

BOSTON UNIVERSITY
SCHOOL OF MEDICINE

Dissertation

**GLYCAN SEQUENCING AND ISOASPARTATE CHARACTERIZATION BY
ELECTRON ACTIVATED DISSOCIATION TANDEM MASS SPECTROMETRY**

by

XIANG YU

B.S., Sichuan University, 2007

Submitted in partial fulfillment of the

requirements for the degree of

Doctor of Biochemistry

2013

Approved by

First Reader

Catherine E. Costello, Ph.D.
Professor of Biochemistry

Second Reader

Cheng Lin, Ph.D.
Assistant Professor of Biochemistry

© Copyright by
XIANG YU
2013

ACKNOWLEDGEMENTS

First of all, I would like to express my deepest gratitude to my advisor, Professor Catherine E. Costello. I would like to thank you for your guidance and support throughout my Ph.D. study. You have always been inspiring and thoughtful in science, patient and progressive as a mentor. You are one of the best advisors I met, very knowledgeable, resourceful, approachable, and extremely nice to your students. You have been truly a role-model for me, in both scientific research and personality.

I am also grateful to Professor Cheng Lin for working closely with me for the last five years. You have lots of great ideas and together we translated them into many different successful projects. You have been always available to answer my questions inside and outside science. Your enthusiasm in scientific excellence gives me confidence in pursuing a career as a scientist.

I want to thank Professor Peter B. O'Connor, who introduced me into the world of mass spectrometry at my second year in graduate school. Although I had worked with you for only one year, you have greatly enlightened my interest in mass spectrometry.

I would like to thank Professor Joseph Zaia, Professor David Harris, and Professor Karen Allen for spending your valuable time serving on my committee and giving me numerous constructive advices.

Many current and past members in the Center for Biomedical Mass Spectrometry (CBMS) contributed to this thesis and it is a great pleasure to work with all of you. Special gratitude goes to Professor Mark McComb and Christian Heckendorf, who provided me a strong IT support; Dr. Yiqun Huang, who helped me a lot on physical chemistry; Dr. Weidong Cui, who taught me how to maintain and trouble-shoot a mass spectrometer; Dr. Chunxiang Yao, with whom I did my first mass spectrometry experiment; Dr. Xiaojuan Li, who worked together with me on the top-down project; Yu Huang, who collaborated with me on the GAG EDD project; Prof. Sandrine Voillard-Bourgoin, who assisted me on FT-ICR mass spectrometry; Dr. Xiaofeng Shi, from whom I learnt a lot on glycan chemistry. I would like to thank the people who helped me at different stages of my doctorate study. They are Ying Zhou, Yang Mao, John Haserick, Han Hu, Liang Han, YanYan Lu, Kshitij Khatri, Mengdi Fan, Chun Shao, Yuhuan Ji, Yi Pu, Dr. Stephen Whelan, Dr. Deborah Francoleon, Dr. Hye Jung Park, Dr. Amanuel Kehasse, Dr. Yan Jiang, Dr. Greg Staples, Dr. Roger Theberge, Dr. Edwin Motari, Dr. Jason Cournoyer, Dr. Zhenning Hong and Dr. David Perlman. I would also thank Denise Neves and Patricia Bullock for all your administrative efforts to let me focus on my research.

It is also a great pleasure to work as an intern for Dr. Wendy Zhong in the Merck research laboratory. I learnt a lot from you on things that I never have a chance to learn in school.

Most importantly, my best friends, Dr. Yi Yang, Yu Huang, Dr. Zhenxiang Xi, Xiaobin Xu, and Dr. Songmao Zheng. I'm so blessed to have all of you in my life.

Finally, I want to thank my parents, for their utmost love.

**GLYCAN SEQUENCING AND ISOASPARTATE CHARACTERIZATION BY
ELECTRON ACTIVATED DISSOCIATION TANDEM MASS SPECTROMETRY**

(Order No.)

XIANG YU

Boston University, School of Medicine, 2013

Major Professor: Catherine E. Costello, Ph.D., Professor of Biochemistry

ABSTRACT

In this study, we carefully examined several types of electron activated dissociation (ExD) processes and developed new ExD techniques that should facilitate biological research, placing particular emphasis on glycan and protein characterization. The first part of this study focuses on determination of ExD fragmentation mechanisms and application of ExD to glycan *de novo* sequencing. Through variation of the electron energy and metal charge carriers, the behaviors of model glycans were systematically studied and a new ExD fragmentation process, designated as electronic excitation dissociation (EED), was found to be the most informative. By identifying and controlling the key parameters, we improved the EED efficiency, to a level that now allows EED to be performed on a time scale that is compatible with high performance liquid chromatography scale. Theoretical modeling was employed to gain insights into the charge remote fragmentation behavior

inherent in the EED process. The experimental results demonstrated that EED has the potential to provide the experimental basis for high-throughput, *de novo* glycan sequencing. The second part of this study focuses on the determination of deamidation of asparagine residues and isomerization of aspartate residues within proteins. In order to avoid the generation of artifacts during trypsin digestion, a comprehensive top-down ExD method was developed to identify both asparagine deamidation and isoaspartate formation at the level of the intact protein. With the consideration that the top-down strategy will eventually fail for high molecular weight proteins, a middle-down ExD method was next developed, for the analysis of peptides generated by proteolysis with Staphylococcal serine protease Protease V8 (Glu-C), carried out at slightly acidic conditions. In addition, the potential for use of in-source decay in isoaspartate analyses was evaluated and its fragmentation mechanisms were investigated.

This research establishes new tools for structural determinations of glycans and significant improvements in methods for the isomer- and site-specific analysis of proteins that contain Asp or Asn residues that can undergo conversion to isoAsp, and provides insight toward understanding and controlling the fundamental processes that lead to the types of fragment ions observed in electron activated dissociation mass spectra.

TABLE OF CONTENTS

Chapter 1	Introduction.....	1
1.1	Introduction to mass spectrometry.....	1
1.1.1	Ion sources.....	1
1.1.2	Mass analyzers.....	4
1.1.3	Ion activation methods for tandem mass spectrometry (MS/MS).....	13
1.2	Glycan sequencing by electron activation dissociation.....	19
1.2.1	Glycan chemistry and its biological roles.....	19
1.2.2	Tandem mass spectrometry of glycans.....	23
1.2.3	Nomenclature of glycan fragments.....	24
1.2.4	Electron activated dissociation of glycans.....	27
1.3	Overview of glycan sequencing by electron activated dissociation.....	32
1.4	Isoaspartate characterization by electron activated dissociation.....	33
1.4.1	Asparagine deamidation and aspartate isomerization.....	33
1.4.2	Mass spectrometry identification of deamidation and isoaspartate formation.....	34
1.5	Overview of isoAsp identification by electron activated dissociation.....	36
1.6	Summary.....	37
Chapter 2	Energy-Dependent Electron Activated Dissociation of Metal-Adducted Permethylated Oligosaccharides.....	38

2.1	Introduction.....	38
2.2	Experimental.....	42
2.2.1	Materials.....	42
2.2.2	Reducing End Reduction.....	42
2.2.3	Reducing End ¹⁸ O-Isotope Labeling.....	43
2.2.4	Permethylation.....	43
2.2.5	Electrospray Conditions.....	44
2.2.6	Tandem Mass Spectrometry.....	44
2.2.7	Data Analysis.....	45
2.3	Results and Discussion.....	46
2.3.1	ExD of the Sodium-Adducted Permethylated Maltoheptaose.....	46
2.3.2	ExD of Lithium-Adducted Permethylated Maltoheptaose.....	57
2.3.3	ExD of Alkaline Earth Metal-Adducted Permethylated Maltoheptaose.....	63
2.3.4	Theoretical Modeling of Glycan ECD.....	67
2.3.5	Theoretical Modeling of Glycan EED.....	71
2.4	Conclusions.....	76
Chapter 3	Detailed Glycan Structural Characterization by Electron Activated Dissociation.....	77
3.1	Introduction.....	78
3.2	Experimental.....	82

3.2.1	Materials.....	82
3.2.2	Reducing End 2-AB Labeling.....	83
3.2.3	<i>N</i> -linked Glycan Release from Ribonuclease B.....	83
3.2.4	Electrospray Conditions.....	84
3.2.5	Tandem Mass Spectrometry.....	84
3.3	Results and Discussion.....	85
3.3.1	Linkage Determination of the High Mannose <i>N</i> -linked Glycan by ExD...85	
3.3.2	Optimization of the EED Experimental Parameters.....	92
3.3.3	Application of EED to Glycan Linkage Isomer Differentiation.....	96
3.4	Conclusions.....	105
Chapter 4	Top-down study of β 2-microglobulin deamidation.....	116
4.1	Introduction.....	116
4.2	Experimental.....	119
4.2.1	Materials.....	119
4.2.2	Reductive Alkylation and <i>In Vitro</i> Aging.....	119
4.2.3	Mass Spectrometry Analysis.....	120
4.3	Results and Discussion.....	122
4.3.1	ESI-MS Analysis of the β ₂ M Protein.....	122
4.3.2	Top-Down ECD Analysis of the Aged β ₂ M Protein.....	124
4.3.3	Identification of isoAsp17 by NSD-ECD MS ³ Analysis and Potential Interference from Sequence Scrambling.....	128

4.3.4	Identification of isoAsp83 by NSD-ECD MS ³ Analysis and Potential Interference from Co-isolation.....	132
4.3.5	Identification of isoAsp42 by NSD-AI-ECD MS ³ Analysis.....	135
4.4	Conclusions.....	139
Chapter 5	Middle-down Isoaspartic Acid Analysis by Glu-C Proteolysis and Electron Activated Dissociation.....	140
5.1	Introduction.....	140
5.2	Experimental.....	144
5.2.1	Materials.....	144
5.2.2	Sample Preparation.....	144
5.2.3	Reversed Phase High Performance Liquid Chromatography	145
5.2.4	Instrumentation.....	145
5.2.5	Data Analysis.....	146
5.3	Results and Discussion.....	147
5.3.1	Challenges in Analyzing the N-terminal Isoaspartate of Tryptic Peptides.....	147
5.3.2	Influencing Factors of the Asn Deamidation Rate during the Glu-C Digestion.....	149
5.3.3	Detection of isoAsp Formation through Electron Activated Dissociation and Charge State Pumping.....	152

5.3.4	pH Dependence of the IsoAsp Formation Rate during the Glu-C Digestion.....	158
5.3.5	Identification of IsoAsp42 in Aged β -2-microglobulin.....	161
5.4	Conclusions.....	163
Chapter 6	In-Source Decay for Isoaspartate Characterization.....	164
6.1	Introduction.....	164
6.2	Experimental.....	168
6.2.1	Peptides and Reagents.....	168
6.2.2	Sample Deposition onto the MALDI-MS Plate.....	168
6.2.3	Mass Spectrometry.....	169
6.3	Results and Discussion.....	170
6.3.1	C_{α} - C_{β} Bond Cleavage within Isoaspartate.....	170
6.3.2	Mechanism of Diagnostic Ion Formation during ISD.....	173
6.3.3	Comparison of ISD Performance between FTICR MS and TOF MS.....	174
6.4	Conclusions.....	176
Chapter 7	Conclusions and Future Perspective.....	177
7.1	Conclusions.....	177
7.2	Future Perspective.....	182

Bibliography.....184

Curriculum Vitae.....201

LIST OF TABLES

Table 2.1	Summary of the glycosidic and cross-ring fragments observed in ExD of permethylated maltoheptaose adducted with Li ⁺ , Na ⁺ , Cs ⁺ , or Mg ²⁺ at three different electron energy levels.....	66
-----------	--	----

LIST OF SCHEMES

Scheme 2.1	Proposed mechanisms for the formation of (a) B [•] and Y ions, and (b) C and Z [•] ions observed in hot-ECD of reduced and permethylated maltoheptaose [M + 2Na] ²⁺ <i>m/z</i> 768.3750.....	50
Scheme 2.2	Proposed mechanisms for neutral losses observed in hot-ECD of reduced and permethylated maltoheptaose [M + 2Na] ²⁺ <i>m/z</i> 768.3750.....	52
Scheme 2.3	Proposed mechanisms for neutral losses from Z-ions observed in hot-ECD of reduced and permethylated maltoheptaose . [M + 2Na] ²⁺ <i>m/z</i> 768.3750.....	54
Scheme 2.4	Proposed EID mechanism for the formation of a doubly charged B ion from the doubly sodiated permethylated maltoheptaose. [M + 2Na] ²⁺ <i>m/z</i> 768.3750.....	55
Scheme 2.5	Proposed mechanisms for the formation of doubly charged fragment ions resulting from (a) glycosidic, and (b) cross-ring cleavages in EED of reduced and permethylated maltoheptaose. [M + 2Na] ²⁺ <i>m/z</i> 768.3750.....	57
Scheme 2.6	Proposed mechanisms for the formation of (a) [C - H + 2Li] ²⁺ by low-energy ECD, and (b) [C - 2H + Li] ²⁺ by hot-ECD.....	62

Scheme 6.1 Formation of the *c/z*-type ISD fragments via hydrogen attachment using 1,5-DAN as the matrix.....166

Scheme 6.2 Formation of the *c+57/z[•]-57* isoAsp diagnostic fragments via hydrogen transfer using 1,5-DAN as the matrix.....174

LIST OF FIGURES

Figure 1.1	Superimposed stability diagrams of three ions with different m/z in the U , V space.....	8
Figure 1.2	A cubic ICR cell (left) and an open-ended cylindrical ICR cell (right). The bold arrow at the top of the drawing indicates the direction of the magnetic field (z-axis)	10
Figure 1.3	Types of peptide backbone cleavages. N -terminal fragments are annotated as a, b, and c fragments, and C-terminal fragments are annotated as x, y, and z fragments	14
Figure 1.4	Glucose, mannose, and galactose are epimers that each differ from one another by one diastereomeric center.....	20
Figure 1.5	Monosaccharides that are derived from glucose through enzymatic modifications.....	21
Figure 1.6	Types of MS/MS fragmentation on a hypothetical N -glycan. The numbering of ring bonds is highlighted in green, glycosidic cleavages are highlighted in blue, and cross-ring cleavages are highlighted in red.....	26

Figure 1.7	The deamidation process of asparagine.....	34
Figure 1.8	The isoAsp diagnostic ions c+57 and z-57 can be produced by ECD or ETD.....	36
Figure 2.1	ExD spectra and cleavage maps of permethylated maltoheptaose $[M + 2Na]^{2+}$ m/z 768.3750 at different electron energy levels: (a) 1.5 eV, (b) 9 eV, and (c) 14 eV.....	48
Figure 2.2	1.5-eV ECD spectrum of sodium adducted native maltoheptaose $[M + 2Na]^{2+}$ m/z 600.1815 with ^{18}O -labeled reducing end.....	50
Figure 2.3	1.5-eV ECD spectra of permethylated maltoheptaose adducted with (a) K^+ , $[M + 2K]^{2+}$ m/z 784.3489, (b) Rb^+ , $[M + 2Rb]^{2+}$ m/z 830.2970, and (c) Cs^+ , $[M + 2Cs]^{2+}$ m/z 878.2907.....	58
Figure 2.4	9-eV hot-ECD spectra of permethylated maltoheptaose adducted with (a) K^+ , $[M + 2K]^{2+}$ m/z 784.3489, (b) Rb^+ , $[M + 2Rb]^{2+}$ m/z 830.2970, and (c) Cs^+ , $[M + 2Cs]^{2+}$ m/z 878.2907.....	59

Figure 2.5	ExD spectra and cleavage maps of permethylated maltoheptaose [M + 2Li] ²⁺ <i>m/z</i> 752.4012 at different electron energy levels: (a) 1.5 eV, (b) 9 eV, and (c) 14 eV.....	60
Figure 2.6	ExD spectra of Mg ²⁺ -adducted permethylated maltoheptaose [M + Mg] ²⁺ <i>m/z</i> 757.3778 at different electron energy levels: (a) 1.5 eV, (b) 9 eV, and (c) 14 eV.....	64
Figure 2.7	ExD spectra of the hybridly adducted permethylated maltoheptaose [M + Li + Na] ²⁺ <i>m/z</i> 760.3881 acquired at (a) 1.5 eV and (b) 9 eV electron energy.....	68
Figure 2.8	The unscaled potential energy surfaces of the methyl and metal loss channels of (a) [Glc-OMe + Li] ⁺ and (b) [Glc-OMe + Na] ⁺ complexes upon electron capture, as calculated at the B3LYP/6-31G(d) level of theory. Numbers in brackets are in units of kcal/mol.....	70
Figure 2.9	The EED spectrum of the Na ⁺ -adducted and ¹⁸ O-labeled cellobiose acquired at an electron energy of 14 eV.....	73
Figure 2.10	The triplet potential energy surface for the EED of cellobiose-Na ⁺ complex to form ^{3,5} A ₂ ion, as calculated at the B3LYP/6-31G(d) level of theory. The numbers in brackets are zero Kelvin enthalpy ⁰ H relative to structure 1a and with unit of kcal/mol. (Data courtesy of Dr. Yiqun Huang)	74

Figure 2.11 The triplet potential energy surface for the EED of cellobiose- Na^+ complex to form $^{1,5}\text{X}_1$ ion, as calculated at the B3LYP/6-31G(d) level of theory. The numbers in brackets are zero Kelvin enthalpy ^0H relative to structure 1a and with unit of kcal/mol. (Data courtesy of Dr. Yiqun Huang)75

Figure 3.1 The ExD fragmentation pattern of metal-adducted glycans is affected by both the electron energy and the charge carrier. Reduced and permethylated maltoheptaose was selected as the model glycan. Precursor ions adducted with either two Li^+ (red circle, m/z 752.4013), two K^+ (green triangle, m/z 784.3490), or two Cs^+ (blue square, m/z 878.2907) were isolated and irradiated with electrons at different energies, ramping from 1 eV to 16 eV at a 1 eV interval. The x axis represents the voltage applied to the cathode dispenser. The y axis represents the percentage ratio of the intensity of a specific type of fragment ion and the total product ion intensity. Fragment ions plotted are (a) doubly charged ions, (b) $[\text{Y-H}+2\text{Metal}]^+$ ions, (c) $[\text{C-2H}+\text{Metal}]^+$ ions, (d) $[\text{C-H}+2\text{Metal}]^+$ ions, (e) $^{1,5}\text{X}+\text{Metal}]^+$ ions, (f) $^{0,2}\text{X}+\text{Metal}]^+$ ions, (g) $^{2,4}\text{A}+\text{Metal}]^+$ ions, and (h) $^{3,5}\text{A}+\text{Metal}]^+$ ions, respectively. The relative abundance of linkage definitive cross-ring cleavage increased significantly as the electron energy approaches the EED region.....78

Figure 3.2 ECD (1.5-eV electrons) cleavage map (top) and spectrum (bottom) of permethylated $\text{Man}_5\text{GlcNAc}_2$ $[\text{M} + 2\text{Li}]^{2+}$ m/z 785.4121.....88

Figure 3.3	Hot-ECD (9.0-eV electrons) cleavage map (top) and spectrum (bottom) of permethylated Man ₅ GlcNAc ₂ [M + 2Li] ²⁺ <i>m/z</i> 785.4121.....	89
Figure 3.4	EED (14.0-eV electrons) cleavage map (top) and spectrum (bottom) of permethylated Man ₅ GlcNAc ₂ [M + 2Li] ²⁺ <i>m/z</i> 785.4121.....	90
Figure 3.5	CID (CE 28 eV) cleavage map (top) and spectrum (bottom) of permethylated Man ₅ GlcNAc ₂ [M + 2Li] ²⁺ <i>m/z</i> 785.4121.....	91
Figure 3.6	a) Schematics of the ExD experimental setup. b) Plot of the relative abundance of the charge reduced species as a function of the cathode heating current, with the cathode bias set at -14 V and the extraction potential at 15 V. c) Plot of the electron current measured at the hexapole as a function of the extraction potential, with the cathode bias set at -14 V, and the cathode heating current set at either 1.3 A (×) or 1.5A (○).....	94
Figure 3.7	Influence of the cathode heating current and extraction lens voltage on the fragmentation pattern of the doubly sodiated permethylated maltoheptaose (<i>m/z</i> 760.3594). With a positive extraction potential of 15 V, allowing all electrons to enter the ICR cell, a) EED dominated at low cathode heating current (1.3 A), and b) ECD dominated at high cathode heating current (1.5 A). c) With the extraction potential set to -	

13.7 V, preventing low-energy electrons from entering the cell, EED fragmentation was recovered at high cathode heating current (1.5 A)95

Figure 3.8 The CID cleavage map and the CID spectrum of the doubly lithiated, permethylated and ^{18}O labeled SLe^{X} precursor ion at m/z 523.2830.....97

Figure 3.9 The ECD cleavage map and the ECD spectrum of the doubly lithiated, permethylated and ^{18}O labeled SLe^{X} precursor ion at m/z 523.2830.....98

Figure 3.10 The EED cleavage map and spectrum of the doubly lithiated, permethylated and ^{18}O -labeled SLe^{X} precursor ion at m/z 523.2830.....99

Figure 3.11 The ECD cleavage map and the ECD spectrum of the doubly lithiated, permethylated and ^{18}O labeled SLe^{A} precursor ion at m/z 523.2830.....100

Figure 3.12 The EED cleavage map and the EED spectrum of the doubly lithiated, permethylated and ^{18}O labeled SLe^{A} precursor ion at m/z 523.2830.....101

Figure 3.13 a) The ECD and b) EED cleavage maps of the doubly lithiated, permethylated, ^{18}O -labeled LNT at m/z 459.7513; c) the EED cleavage map of the singly lithiated, permethylated, ^{18}O -labeled LNT at m/z 912.4872; d) the EED cleavage map of the singly cesiated, permethylated, ^{18}O -labeled LNT at m/z 1038.3767.....102

Figure 3.14	a) The ECD and b) EED cleavage maps of the doubly lithiated, permethylated, ¹⁸ O- labeled LNnT at <i>m/z</i> 459.7513; c) EED cleavage map of singly lithiated, permethylated, ¹⁸ O-labeled LNnT at <i>m/z</i> 912.4872; d) EED cleavage map of singly cesiated, permethylated, ¹⁸ O-labeled LNnT at <i>m/z</i> 1038.3767.....	103
Figure 3.15	The EED cleavage map and spectrum of the singly lithiated, permethylated and ¹⁸ O labeled SLe ^X precursor ion at <i>m/z</i> 1039.5505.....	104
Figure 3.16	The EED cleavage map and spectrum of the singly lithiated, permethylated and ¹⁸ O-labeled SLe ^A precursor ion at <i>m/z</i> 1039.5505.....	106
Figure 3.17	The EED cleavage map and spectrum of the singly lithiated and permethylated (Man) ₅ (GlcNAc) ₂ at <i>m/z</i> 1563.8808.....	107
Figure 3.18	The EED cleavage map and spectrum of the doubly lithiated and permethylated (Man) ₅ (GlcNAc) ₂ at <i>m/z</i> 785.4121.....	109
Figure 3.19	The EED cleavage map and spectrum of the singly cesiated, permethylated, ¹⁸ O-labeled SLe ^X at <i>m/z</i> 1165.4400.....	110

Figure 3.20	The EED cleavage map and spectrum of the singly cesiated, permethylated, ¹⁸ O-labeled SLe ^A at <i>m/z</i> 1165.4400.....	111
Figure 3.21	a) The EED cleavage map of the SLe ^X [M + Cs] ⁺ <i>m/z</i> 1165.4400. b) Fragment ions from SLe ^X [M + 2Cs] ²⁺ <i>m/z</i> 649.1724 can be clustered into different trend lines in the mass defect vs. mass plot based on their Cs+ content.....	112
Figure 3.22	The EED cleavage map and single scan spectrum of the singly cesiated, permethylated, and ¹⁸ O-labeled (Man) ₅ (GlcNAc) ₂	113
Figure 3.23	a) ECD of the [M + 2Li] ²⁺ <i>m/z</i> 519.2938 and b) EED of the [M + Li] ⁺ <i>m/z</i> 1031.5721 of 2-AB labeled, permethylated maltotetraose.....	114
Figure 4.1	ESI mass spectra of the (a) native, (b) reduced/alkylated, and (c) reduced/alkylated and aged β ₂ M. For each spectrum, a selected charge state is enlarged to illustrate the presence of two isotopic clusters (with or without Met oxidation) as well as the mass shifts caused by reductive alkylation and Asn deamidations (insets). All <i>m/z</i> values listed are those of the monoisotopic peak as determined by the SNAP algorithm	123

Figure 4.2 Top-down ECD spectrum of the reduced/alkylated and aged β_2 M in 14+ charge state, shown in four segments for clarity. The cleavage map is shown on top of the spectrum. The inset shows the *N*-terminal diagnostic ion for isoAsp17.....126

Figure 4.3 Enlarged regions of the ECD spectra of the unaged and the aged β_2 M for (a) c_{16}^{3+} and c_{17}^{3+} ions, (b) c_{41}^{6+} and c_{43}^{6+} ions, and (c) z_{16}^{2+} and z_{19}^{2+} ions.....127

Figure 4.4 30 eV NSD spectrum of the aged β_2 M. Insets show the three isoAsp-containing fragments selected for further ECD analysis.....128

Figure 4.5 NSD-ECD spectrum of the b_{22}^{4+} ion generated from the aged β_2 M, with the cleavage map shown on top of the spectrum. The inset shows the *N*-terminal diagnostic ion for isoAsp17.....129

Figure 4.6 NSD-ECD spectrum of the y_{28}^{5+} ion generated from the aged β_2 M, with the cleavage map shown on top of the spectrum. Inset (a) shows the enlarged region at the precursor ion *m/z*, insets (b-d) show the *N*- and *C*-terminal diagnostic ions for isoAsp83. * denotes peaks resulting from ECD of the co-isolated $(a_{24}\text{-NH}_3)^{4+}$ ion.....133

Figure 4.7 NSD-AI-ECD spectrum of the b_{63}^{9+} ion generated from the aged β_2 M, shown in two segments for clarity. The cleavage map is shown on top of the spectrum. Insets (a) and (b) show the comparison between the NSD-AI-ECD and NSD-ECD spectra

at the *N*-terminal isoAsp42 diagnostic ion region; insets (c) and (d) show the comparison at the *C*-terminal isoAsp42 diagnostic ion region.....137

Figure 5.1 MALDI-TOF MS spectra of the synthetic peptides BUXY1 (a) and BUXY2 (b) after 18-h overnight trypsin digestion in pH 7.8 buffer solution at 37 °C...148

Figure 5.2 Isotope patterns of the quadruply charged, unaged RNaseA peptides derived from (⁵⁰SLADVQAVC*SQKNVAC*KNGQTNC*YQSYSTMSITDC*RE⁸⁷) and extracted at different times during the Glu-C digestion in a solution buffered at pH 7.8 (left column) and pH 4.0 (right column) at 25 °C. The theoretical distribution of the unaged form of the same peptide is shown at the top of each column.....151

Figure 5.3 The isotope pattern of the quadruply charged unaged RNaseA peptide (⁵⁰SLADVQAVC*SQKNVAC*KNGQTNC*YQSYSTMSITDC*RE⁸⁷) extracted after 18-h Glu-C digestion in buffer solutions at pH 4.0 at 37 °C. The theoretical distribution of the unaged form of the same peptide is shown at the top for comparison..... 152

Figure 5.4 ExD spectra and c, z cleavage maps of the quadruply charged aged RNaseA peptide (⁵⁰SLADVQAVC*SQKNVAC*K(D/isoD)GQT(N/D/isoD)C*YQSYSTMSITDC*RE⁸⁷): (a) ECD, (b) hot-ECD, and (c) AI-ECD spectra. Insets show the absence or the presence of the diagnostic ions of isoAsp 67 and isoAsp 71.....154

Figure 5.5 The isotope pattern shifts of the quadruply charged aged RNaseA peptides (⁵⁰SLADVQAVC*SQKNVAC*KDGQTDC*YQSYSTMSITDC*RE⁸⁷) extracted after 18-h Glu-C digestions in buffer solutions at pH 7.8 (left column) and pH 4.0 (right column) at 25 °C. For comparison, the theoretical distributions of the same peptides with 1 and 2 deamidation sites are shown at the top and bottom of each column.....155

Figure 5.6 The ECD spectrum and the c, z cleavage map of the [M+5H]⁵⁺ ion of the aged RNaseA peptide (⁵⁰SLADVQAVC*SQKNVAC*KDGQTDC*YQSYSTMSITDC*RE⁸⁷) produced from the Glu-C digestion at pH 4.0 at 25 °C. Insets show the diagnostic ions of isoAsp67 and isoAsp71.....157

Figure 5.7 Formation of isoAsp 67 during the Glu-C digestion of unaged RNaseA as monitored by its diagnostic ions using AI-ECD. The RNaseA peptides (50-87) were extracted at different times during the Glu-C digestions in buffer solutions at pH 7.8 (left column) and pH 4.0 (right column) at 25 °C. IsoAsp diagnostic ions of the aged RNaseA peptides are also shown at the bottom as controls.....159

Figure 5.8 Formation of isoAsp67 during the Glu-C digestion of unaged RNaseA as monitored by its diagnostic ions using AI-ECD. Target RNaseA peptides

(⁵⁰SLADVQAVC*SQKNVAC*KD/(iso)DGQTNC*YQSYSTMSITDC*RE⁸⁷) were extracted after 9-h and 18-h Glu-C digestions in the pH 4.0 buffer solution at 37 °C. Insets indicate the absence of the isoAsp diagnostic ion. IsoAsp diagnostic ions of the aged RNaseA peptides are also shown at the bottom as the positive control.....160

Figure 5.9 ECD spectra of the triply charged aged β2M peptide from Glu-C overnight digestion at pH 4.0 at 25 °C. Insets show the diagnostic ions of the isoAsp42. Insets in the dotted box illustrate the absence of the isoAsp42 diagnostic ions during the analysis of unaged β2M peptide obtained at the same conditions.....161

Figure 6.1 The ISD spectrum of the aged and Glu-C digested β2M peptide (1-36) using 1,5-DAN/2-PA as the matrix, acquired on a solariX 12-T FTICR mass spectrometer. Inset shows the diagnostic fragment for the isoAsp17 residue.....171

Figure 6.2 The ISD spectrum of the aged and Glu-C digested β2M peptide (78-99) using 1,5-DAN/2-PA as the matrix, acquired on a solariX 12-T FTICR mass spectrometer.....172

Figure 6.3 The single scan ISD-CASI spectrum of the aged β2M using 1,5-DAN/2-PA as the matrix, acquired on a solariX 12-T FTICR mass spectrometer.....173

ABBREVIATIONS

AI-ECD	activated ion electron capture dissociation
AP	atmospheric pressure
BIRD	blackbody infrared radiative dissociation
CAD	collisionally activated dissociation
CHCA	α -cyano-4-hydroxycinnamic acid
CHOS	chitooligosaccharides
CI	chemical ionization
<i>d.c.</i>	direct current
DHB	2,5-dihydroxybenzoic acid
DS	dermatan sulfate
ECD	electron capture dissociation
EED	electronic excitation dissociation
EI	electron ionization
EID	electron ionization dissociation
EIEIO	electron-impact excitation of ion from organics
EInD	electron induced dissociation
ER	endoplasmic reticulum
ESI	electrospray ionization
ETD	electron transfer dissociation
eV	electron volt

ExD	electron activated dissociation
FAB	fast atom bombardment
FT-ICR	Fourier transform ion cyclotron
GAG	glycosaminoglycan
Gal	galactose
GlcNAc	<i>N</i> -acetylglucosamine
Glu	glucose
GlcA	glucuronic acid
hECD	hot electron capture dissociation
IdoA	iduronic acid
IRMPD	infrared multiphoton dissociation
LC	liquid chromatography
<i>m/z</i>	mass-to-charge ratio
MALDI	matrix-assisted laser desorption/ionization
MS ⁿ	multistage tandem mass spectrometry
MS/MS	tandem mass spectrometry
nETD	negative electron transfer dissociation
niECD	negative ion electron capture dissociation
PTM	post-translational modification
<i>r.f.</i>	radio frequency
S/N	signal-to-noise ratio
SLe ^A	sialyl-Lewis A

SLe ^x	sialyl-Lewis X
TOF	time of flight
UV	ultraviolet
VUVPD	vacuum ultraviolet photodissociation

Chapter 1 Introduction

1.1 Introduction to mass spectrometry

Biomolecules are produced by every living organism and are the structural basis for all biological functions. In order to better understand biological processes, it is necessary to elucidate the structures of these molecules. Among the current technologies to probe the structures of biomolecules, mass spectrometry (MS) plays an increasingly important role as it is sensitive, accurate and fast.

MS measures the mass-to-charge ratio (m/z) of charged atoms or molecules (ions). A mass spectrometer usually consists of three components: an ion source, which converts neutral molecules to ions, a mass analyzer, which separates ions based on their m/z , and an ion detector, which detects and outputs the signals of the separated ions. In the early years of the technique, the use of MS was limited to small and/or volatile molecules. Recently, the rapidly increasing demand of biopolymer analysis has accelerated the development of new types of ion sources, mass analyzers, and ion detectors.

1.1.1 Ion sources

Many important biomolecules are labile and high in molecular weight. Classic ion sources, such as electron ionization (EI) and chemical ionization (CI), are not useful for the analysis of large molecules, since they require that the sample be in the gas phase and the heating required to volatilize the samples often produces severe decomposition and

since EI transfers so much energy to the analyte (*ca.* 70 eV) that extensive fragmentation results. The development of soft ion sources facilitated the ionization of large, nonvolatile biomolecules. Three soft ion sources have been widely used for biomolecule analysis, fast atom bombardment (FAB)¹ or liquid secondary ionization MS (LSIMS), matrix-assisted laser desorption/ionization (MALDI)², and electrospray ionization (ESI).³

To perform FAB or LSIMS, the analyte is protected by a liquid matrix, such as glycerol or thioglycerol, and is impacted by a high energy (a few keV) atom (FAB) or ion (LSIMS) beam. The kinetic energy is absorbed by the matrix and the non-volatile analyte is ionized by energy transferred from the matrix. However, the practical use of FAB/LSIMS to biomolecules is limited by its high background signal, low tolerance to samples with salts, limited mass range and sensitivity, sample insolubility, and sample decomposition.

Compared to FAB/LSIMS, MALDI and ESI are more gentle ionization techniques. MALDI was first reported by M. Karas and F. Hillenkamp in 1985.² Two years later, K. Tanaka, *et al.* used a technique that employed an ultrafine metal powder and glycerol and successfully ionized proteins and polymers, producing signals from multimers that were detected up to 100,000 Da. The latter work was awarded Nobel Prize in Chemistry in 2002. The details of the MALDI mechanism remain controversial. A possible mechanism for the ion formation in MALDI can be described as follows:⁴ a MALDI matrix, such as 2,5-dihydroxybenzoic acid (DHB) or α -cyano-4-hydroxycinnamic acid (CHCA), is first co-crystallized with the analyte on a metal plate. By irradiating the matrix with a pulsed

high intensity UV laser (*e.g.* 355 nm, at the tripled frequency of a Nd:YAG laser), a hot MALDI plume containing a mixture of ionized matrix and analyte molecules is generated. Gas phase proton transfer can then take place in this mixture, resulting in protonated species. The advantages of MALDI include straightforward sample preparation, minimal analyte decomposition, and high tolerance for the presence of salts and buffers. Additionally, MALDI produces mostly singly charged ions, which simplifies the data interpretation procedures.

ESI was developed by J. B. Fenn,³ who was later recognized as a Nobel laureate in Chemistry. In a typical ESI experiment, the analyte is first dissolved in a solution that is volatile and has low surface tension (*e.g.* 50 % methanol or acetonitrile). To increase the ionization efficiency, a small amount (0.5 % - 2 %) of acid or base is usually mixed into the solution; formic acid is often used for the positive ionization mode and ammonium hydroxide for the negative ionization mode. At atmospheric pressure (AP), ESI solution containing the analyte is passed through a capillary with a small orifice at its end. When a voltage of a few kilovolts is applied at the other end of the capillary, the resulting electric field drives the solution out of the small orifice and generates a spray with a characteristic shape known as Taylor cone. Hydraulic pressure generated by a solvent pump promotes stable spray formation. The spray is composed of small charged droplets, which quickly disperse due to the effects of heating, drying gas collision, and the Coulombic repulsion. This “Coulombic fission” process releases smaller offspring charged droplets until a single, usually highly charged molecule is produced.⁵ Before entering into the mass

analyzer, neutral molecules are swept away by nitrogen (N₂) curtain gas, and only the ionized molecules are transferred into the mass analyzer. ESI allows ionization of macro-biomolecules with minimal decomposition and is most widely used in conjunction with liquid chromatography (LC).

To increase the sensitivity of ESI, M.S. Wilm and M. Mann, introduced nanoESI in 1994.⁶⁻⁷ A nanoESI experiment is performed using a capillary with a ~1-2 μm orifice. With such a small orifice, no external hydraulic pressure is needed to drive out the droplets, making the flow rate of nanoESI very low (a few hundred nL/min). The small orifice also increases the charge density of the initial droplets, resulting in a more efficient “Coulombic fission” process. Due to its better sensitivity and ionization efficiency, nanoESI fits better for the analysis of biomolecules that are available only in small quantities.

1.1.2 Mass analyzers

The ionized biomolecules are guided to a mass analyzer that sorts ions according to their m/z by applying electrical and/or magnetic fields to control ion motion. Each mass analyzer has its unique characteristics. Rational selection of an appropriate mass analyzer is necessary and the choice depends on the specific applications. The performance of a mass analyzer is evaluated by the parameters of mass accuracy, dynamic range, resolving power, detection limit, scan rate, *etc.*

Mass accuracy refers to the correctness of mass measurement, which is calculated through the Eqn. 1.1:

$$\text{mass accuracy (in ppm)} = \frac{(\text{measured mass} - \text{theoretical mass})}{\text{theoretical mass}} \times 10^6 \quad \text{Eqn. 1.1}$$

Dynamic range defines the minimum to maximum signal intensities that may be accurately determined.

Resolving power is the capability for separating two ions that differ in their m/z values. Ions are usually considered to be resolved from one another when they are separated between them at 50% peak height. The resolution of a selected peak can be calculated through Eqn. 1.2:

$$\text{Resolution} = \frac{(m/z)_c}{(m/z)_{\text{FWHM}}} \quad \text{Eqn. 1.2}$$

where $(m/z)_c$ is the m/z value of the peak centroid and $(m/z)_{\text{FWHM}}$ is the peak width measured at half of its maximum intensity (FWHM). A mass analyzer with higher resolving power has higher capability for separation and accurate determination of ions with close m/z values.

The detection limit reflects the smallest quantity of sample needed to give a signal that is distinguishable from background noise. Scan rate refers to the frequency of mass spectra acquisition and requires consideration of the scan time required to record a spectrum over the set m/z range, with high fidelity in terms of peak definition.

Quadrupole and Fourier transform ion cyclotron resonance (FT-ICR) mass analyzers are mainly used for the work presented here and will be discussed in the following sections.

Quadrupole mass analyzer

A quadrupole mass analyzer operates using four parallel hyperbolic or circular rods, which are usually plated with gold to minimize surface roughness and oxidation. Each rod is supplied with a radio frequency (*rf*) oscillating electric field and a superimposed direct current (*dc*) voltage. Ions with a stable trajectory under the combination of fields will pass through the quadrupole and be detected by an electron multiplier. The fields can be scanned to record a complete spectrum or set at a constant to transmit a selected ion packet. Equations 1.3 and 1.4 are used to describe the ion stabilities in a quadrupole:⁸

$$a_m = \frac{8eU}{(m/z)r_0^2\omega^2} \quad \text{Eqn. 1.3}$$

$$q_m = \frac{4eV}{(m/z)r_0^2\omega^2} \quad \text{Eqn. 1.4}$$

where e is the charge of an electron, U is the *dc* amplitude, V is the *rf* amplitude, ω is the *rf* angular frequency, and r_0 is half the distance between two opposing rods. Mathieu parameters, a_m and q_m , are directly related to U and V . The solution of the Mathieu equations for ions with a specific m/z gives a stability diagram. As shown in Figure 1.1, to obtain an optimum resolution, the U , V amplitudes are increased with a fixed ratio that forms a scan line close to the peaks of continuous m/z values. As the U , V amplitudes get close to the stability area of a specific m/z , the corresponding ions will be axially transmitted and detected.

Although a quadrupole mass analyzer is sensitive and fast, it has limited resolving power and is therefore often used in combination with a high-resolution mass analyzer such as an FT-ICR or a time-of-flight (TOF) analyzer in a hybrid mass spectrometer.

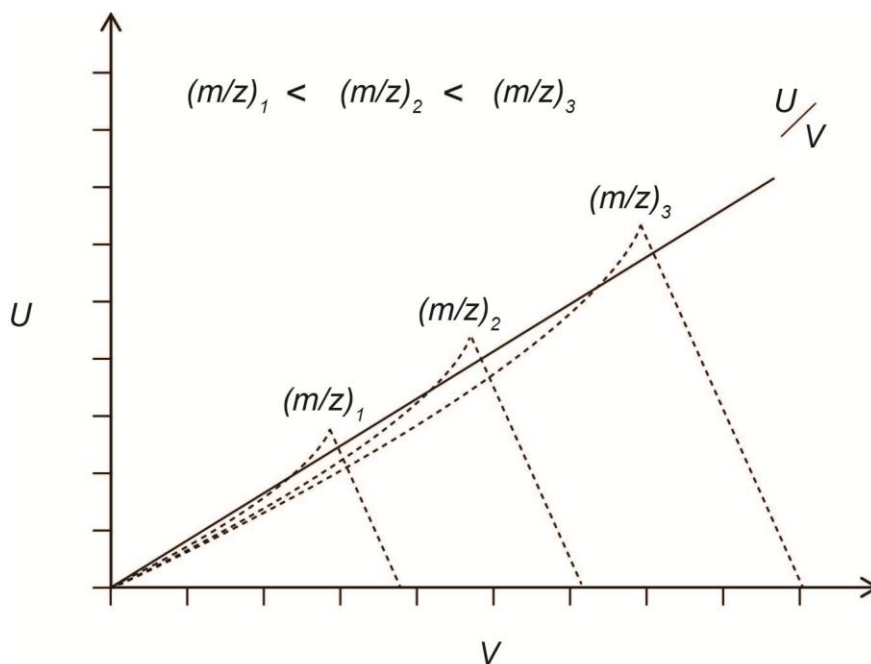


Figure 1.1 Superimposed stability diagrams of three ions with different m/z in the U, V space.

Fourier transform ion cyclotron resonance (FT-ICR) mass analyzer

The Fourier transform ion cyclotron resonance (FT-ICR) MS, developed by M.B. Comisarow and A.G. Marshall in 1974,⁹⁻¹⁰ incorporates a non-destructive mass analyzer that has both high mass accuracy and high resolving power. Although the ICR MS had been under investigation in a number of laboratories since the 1960s,¹¹⁻¹² the initial limitations for data acquisition and processing had restricted its use to theoretical studies and applications to small molecules and metal clusters. Introduction of a system that allowed accumulation of many spectra and rapid Fourier transform of the complex spectra opened the field to widespread use and the application of FT-ICR MS to a much broader range of applications. A typical FT-ICR mass analyzer has two major

components. One is a permanent or superconducting magnet. Higher performance can be obtained with higher-field magnets. At the present time, magnets ranging from 3 T to 15 T are commercially available. Laboratories in both the Pacific Northwest National Laboratory (PNNL) and the National High Magnetic Field Laboratory are constructing 21-T FT-ICR MS instruments. The other is an ICR cell, the place where ions are analyzed and detected. A typical ICR cell has the following constituents: two excitation plates and two detection plates, which are parallel to the direction of the magnetic field, and two trapping plates, which are perpendicular to the magnetic field. The first ICR cell had a cubic design¹³ and a more commonly used design is a cylindrical shaped cell (Figure 1.2).¹⁴ The cylindrical cell is more favored as it makes more efficient use of the chamber of the super conducting magnet,¹⁵ and it also allows ions, electrons and laser beam to enter into the ICR cell without a mechanical barrier.¹⁶

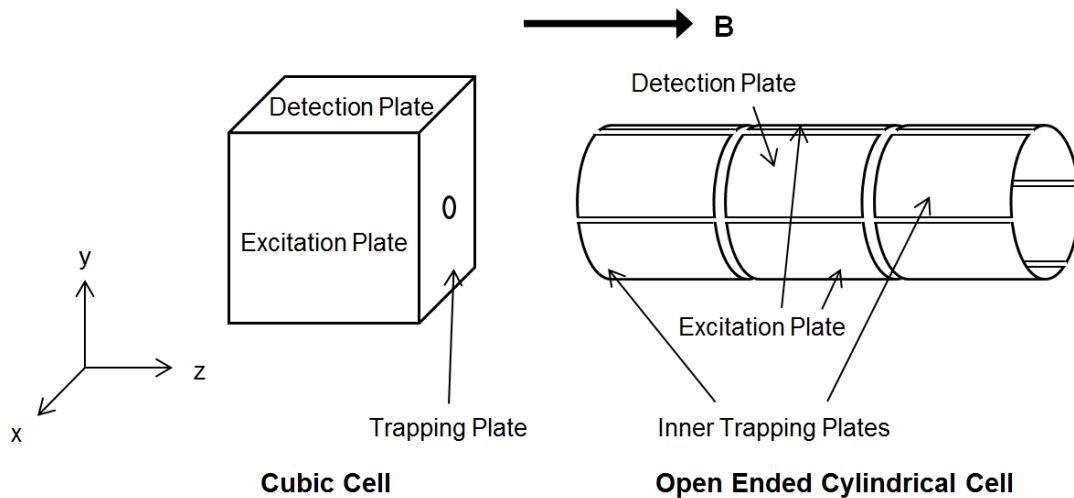


Figure 1.2 A cubic ICR cell (left) and an open-ended cylindrical ICR cell (right). The bold arrow at the top of the drawing indicates the direction of the magnetic field (z-axis).

For a hybrid FT-ICR MS, ions are generated externally typically by either MALDI or ESI. After being transferred into the ICR cell, the ions are axially trapped by the electrical field generated by the two opposing trapping plates, and are radially trapped by the magnetic field. The combination of magnetic and electric fields generates three types of ion motions in the ICR cell: cyclotron motion, axial trapping motion and magnetron motion. In a given magnetic field (\mathbf{B}), the Lorentz force (\mathbf{F}) experienced by an ion having a mass of m and a charge of q can be described as:

$$\mathbf{F} = m\mathbf{a} = m \frac{v^2}{r} = q (\mathbf{v} \otimes \mathbf{B}) \quad \text{Eqn. 1.5}$$

where v is the tangential velocity of the ion and r is the radius of its cyclotron motion.

The frequency of the cyclotron motion (f_c) is defined as:

$$f_c = \frac{v}{2\pi r} \quad \text{Eqn. 1.6}$$

The solution to Eqn. 1.5 and Eqn. 1.6 gives

$$m/q = \frac{\mathbf{B}}{2\pi f_c} \quad \text{Eqn. 1.7}$$

Therefore, the m/z of an ion is inversely proportional to its cyclotron frequency (f_c).

While the magnetic field traps ions in the x - y plane, the ions are also trapped with harmonic oscillation along the z -axis by the electric field generated by the trapping plates (Figure 1.2). For a cubic ICR cell, when a voltage of V_t is applied to the trapping plate, the potential at the cell center is $V_t/3$. This positive potential creates an repulsive electric field on the x - y plane, which pushes the ions towards the excitation and detection plates. The interplay between the magnetic field and the radial electric field generates an additional ion motion around the magnetic field, known as the magnetron motion. For a given cell design, where d is the distance between trapping plates and α is the cell geometry factor, the frequency of the magnetron motion is a function of the trapping voltage (V_t) and the magnetic field strength (\mathbf{B}) (Eqn 1.8).

$$f_m = \frac{\alpha V_t}{\pi d^2 \mathbf{B}} \quad \text{Eqn. 1.8}$$

The magnetron motion leads to a reduction of the observed cyclotron frequency (known as the reduced cyclotron frequency), and affects the accuracy of the mass measurement. It is clear from Eqn. 1.8 that the effect of the magnetron motion can be minimized by reducing the trapping voltage during detection.

The cyclotron motion of an ion packet induces an alternating image current between the opposing detection plates. However, the initial thermal cyclotron motions of ions are not coherent and the net image current is zero. In order to produce a coherent cyclotron motion, it is necessary to excite the ions with the same m/z to a large radius by a spatially uniform electrical field. To detect the ions covering a broad range of m/z , a broadband excitation is usually carried out by applying a chirp waveform, which rapidly sweeps across a wide continuous range of frequencies corresponding to the m/z range of interest. Ions with different m/z will be excited to the same radius and will each induce an image current with a frequency that corresponds to their specific cyclotron frequency, generating a set of superimposed time-domain transient signals. The complete transient signal is further amplified, digitized, and stored in a computer. The cyclotron frequency of each ion can be obtained by performing Fourier transform on the time-domain transient signal.

The resolution (R) of FT-ICR MS for a given ion is linearly proportional to the magnetic field strength (B) and the length of transient signal (T) as described in Eqn. 1.9.

$$R = \frac{B T}{4\pi(m/q)} \quad \text{Eqn. 1.9}$$

Because collisions between ions and neutral gases reduce the mean free path of ions and therefore the time span of the transient signal, in order to achieve high resolution, the ICR cell is usually operated under ultra-high vacuum (e.g. $10^{-9} - 10^{-10}$ Torr), to minimize gas collisions and transient decay.

1.1.3 Ion activation methods for tandem mass spectrometry (MS/MS)

The ion activation methods for MS/MS fall into two categories: vibrational and electronic. The vibrational ion activation can be triggered either by colliding the ions with neutral gases, as employed in collisionally activated dissociation (CAD), or by irradiating them with an infrared laser, as in infrared multiphoton dissociation (IRMPD). CAD and IRMPD of peptides break amide bonds and produce b and y fragments¹⁷ as shown in Figure 1.3. Other than leucine (Leu) and isoleucine (Ile), each of the twenty common amino acids has its unique mass, therefore the full sequence of the precursor peptide can be deduced by measuring the masses of fragments, provided that a complete series of fragment ions are produced. For example, if the mass difference between b_5 and b_4 ions is 97.05 u, then the fifth residue can be deduced as a proline (Pro).

The collision energy also affects fragmentation patterns. The collision energy used for low-energy CAD experiments is usually below 100 eV. When a collision energy in the range from a few hundred to 10 keV is applied, high energy CAD (HE CAD) spectra can be obtained; these include many more fragments than regular CAD spectra. Despite the advantages of HE CAD, it can only be performed on sector MS and MALDI-TOF/TOF MS instruments, and this limits the wide application of this technique to biomolecule analysis.

As an ergodic process, vibrational ion activation breaks the weakest bonds in a molecule. This characteristic makes CAD one of the most routinely used fragmentation techniques for the sequencing of unmodified peptides and glycans. Vibrational ion activation has been discussed in previous reviews.¹⁸⁻¹⁹

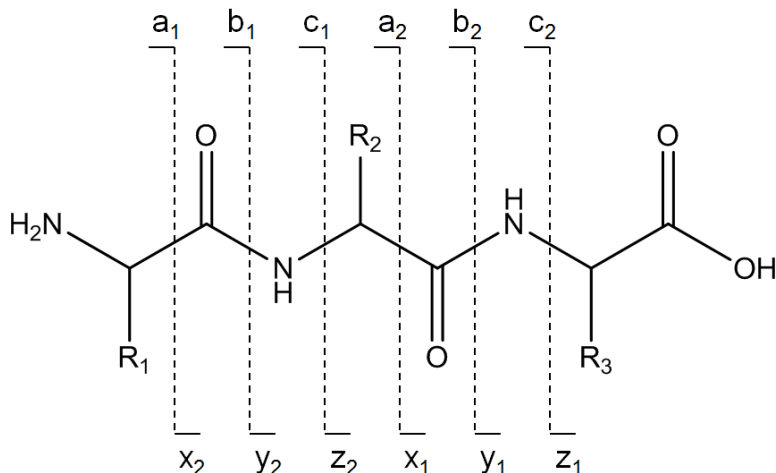
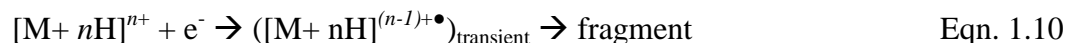


Figure 1.3 Types of peptide backbone cleavages. *N*-terminal fragments are annotated as a, b, and c fragments, and C-terminal fragments are annotated as x, y, and z fragments.²⁰

Electron activation dissociation

The application of electron activated dissociation (ExD) in proteomics has been very successful since the discovery of electron capture dissociation (ECD) in 1998.²¹ Most of the knowledge on ExD has been obtained through gas-phase dissociation studies on peptides.²² Based on the electron energy applied, peptide fragmentation modes, and the chemistry of peptides, ExD can be classified into the following types: electron capture dissociation (ECD), electron transfer dissociation (ETD), negative electron transfer dissociation (NETD), hot-ECD (hECD), electronic excitation dissociation (EED), electron ionization dissociation (EID), and electron detachment dissociation (EDD).²²

Within the range of low electron energy interactions (< 1 eV), a positively charged precursor ion can capture electrons and undergoes recombinative dissociation known as ECD (Eqn. 1.10). Because ECD is a non-ergodic process, instead of cleaving the weakest bonds, ECD cleaves N-C $_{\alpha}$ bonds, generating c- and z-type fragments. Compared to the b and y ions produced by CAD, c and z ions do not provide substantially different information on the peptide sequence. However, the non-ergodic nature of ECD preserves the labile modifications on a peptide, making it an informative tool for the identification of protein post-translational modifications (PTMs).



When the precursor ion has a negative net charge, electrons can still be captured if the precursor ions have local positive charges, *i.e.*, are zwitterions, a process known as the negative ion ECD (niECD). niECD was shown to be informative in identifying the sulfate modifications in peptides.²³ niECD requires the use of electrons with higher kinetic energy (~ 4.5 eV) to obtain a sufficient cross-section for their interaction with the precursor ions. However, not all biomolecules are capable of generating zwitter ions, and this factor limits the practical use of niECD to sulfated and phosphorylated peptides.

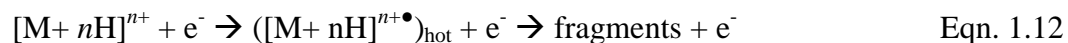
An analog to ECD is ETD, invented by D.F. Hunt *et al.*²⁴ The major advantage of ETD is that it does not require a large and expensive FT-ICR MS instrument. During ETD, instead of free electrons, anionic reagents such as fluoranthene are used to create radicals on the precursor cations (Eqn 1.11).



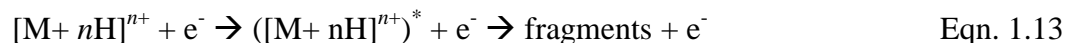
In order for ETD to occur, an electron is detached from the ETD reagent in an external negative ion chemical ionization source and the reagent anion radicals are transferred to the reaction chamber (either a collision cell or an ion trap) containing the precursor cations. ETD is a milder process than ECD, since part of the recombination energy is offset by the energy required for the electron detachment from the ETD reagent and since ETD is usually performed in a high-pressure region where collisional cooling further reduces the energy deposition. Hydrogen transfer between the complementary fragment ions may frequently occur during ETD, which complicates the interpretation of the

resulting spectra. When a precursor ion has a high molecular weight, an electron can be transferred without inducing further fragmentation, a process known as the ETnoD. Therefore, in order to minimize the above problems, ETD is usually carried out together with ion activation by gas collision or infrared laser irradiation, the latter of which is known as AI-ETD. Electrons can also be transferred from an anionic precursor ion to a cationic ETD reagent, generating an electron-deficient anion that is capable of undergoing rearrangement and fragmentation. This process is called negative electron-transfer dissociation (NETD).

The electron capture cross-section of precursor ions is greatly reduced when the electron energy increases above a few eV. When such higher energy electrons are used, vibrational energy can be introduced into the precursor ions, producing b and y fragments in addition to the regular c- and z-type ions observed in ECD (Eqn. 1.12). This process is called hot-ECD (hECD). Excess vibrational energy can also induce secondary cleavages on the peptide side chain, which is useful for the differentiation of Leu and Ile.²⁵



In addition to vibrational activation, electronic excitation can occur as the electron energy is further increased above 5-7 eV. The fragmentation process induced by electronic excitation is known as EED (Eqn. 1.13).

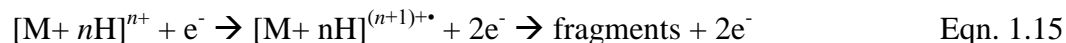


When the electron energy is increased above the ionization threshold of peptide cations, electronic excitation can be achieved by a two-step process: tandem ionization and electron re-capture (Eqn. 1.14).²⁶⁻²⁷



Because EED does not result in charge reduction, it is compatible with both singly and multiply charged precursor ions.²⁸ This property provides an advantage over ECD, which can only be performed on multiply charged ions. In addition to c, z, b, and y ions, EED can produce more ion types, such as a, x and w ions. Although EED provides wide charge state compatibility and rich sequence information, it is not an efficient process, and an increase in EED efficiency is required before it becomes practical for general use.

When the electron energy is above the ionization threshold (9-10 eV), an electron can be ejected from the precursor ions resulting in the formation of (n+1)⁺ species through tandem ionization, as shown in Eqn. 1.15. As the ionization *per se* does not produce any fragmentation, additional energy deposition into the (n+1)⁺ species is needed to induce further fragmentation in a process known as electron ionization dissociation (EID). EID is usually performed using electrons with kinetic energy higher than 30 eV.²⁹



During the past 14 years, since the invention of ECD, the ExD techniques have been used to address numerous analytical challenges in proteomics, including top-down sequencing,²¹ PTM identification,³⁰ and differentiation of isomeric residues.²⁵ It has become clear that ExD methods have great potentials and should contribute substantially to the structural analysis of a wide variety of biomolecules.

1.2 Glycan characterization by electron activation dissociation

1.2.1 Glycan chemistry and its biological roles

Carbohydrates or glycans constitute one of the four major classes of biomolecules. They are the most abundant organic materials on earth. For most living organisms, not only are glycans used as the major energy source and the basis of structural support, but they also participate in a wide variety of cellular processes.³¹

The building blocks of glycans are monosaccharides. A monosaccharide can be an aldose (*e.g.* glucose, Glc) or a ketose (*e.g.* fructose, Fru), which is essentially an aldehyde or a ketone, with multiple hydroxyl groups, attached to carbon atoms. In solution, monosaccharides exist in a mixture of two equilibrated forms: the open-chain form or the closed-ring form that is generated when the carbonyl group of the aldehyde or ketone reacts with a distal hydroxyl group to yield a hemiacetal or hemiketal, respectively.³² In

solution, the five- or six- membered ring is the primary structure for glycans. Each carbon on the monosaccharide ring can be a potential diastereomeric center that can give rise to epimers (Figure 1.4).

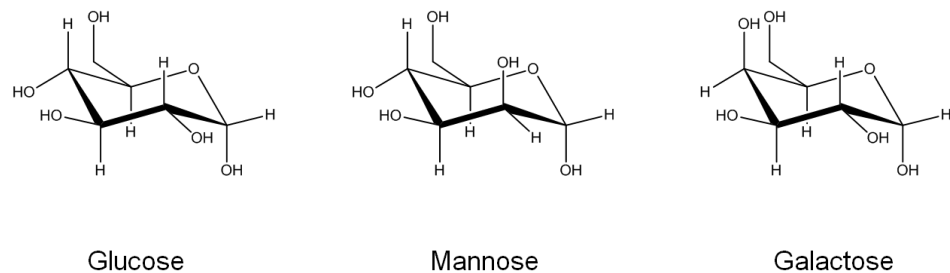


Figure 1.4 Glucose, mannose, and galactose are epimers that each differ from one another by one diastereomeric center.

For aldose, formation of a hemiacetal bond creates an additional diastereomeric center in C-1, which is also known as the anomeric carbon. The C-1 epimers can be either an α -anomer, or a β -anomer, depending on the relative stereo configuration of the anomeric carbon and the anomeric reference carbon (*e.g.* C-5 for aldohexoses). The two anomers can interconvert and eventually reach equilibrium in solution. The hydroxyl groups on the carbohydrate ring can be converted to or substituted by different functional groups through enzymatic modifications, which lead to different chemical properties (Figure 1.5). The combination of epimers and enzymatic modifications theoretically can give rise to a wide variety of monosaccharides.

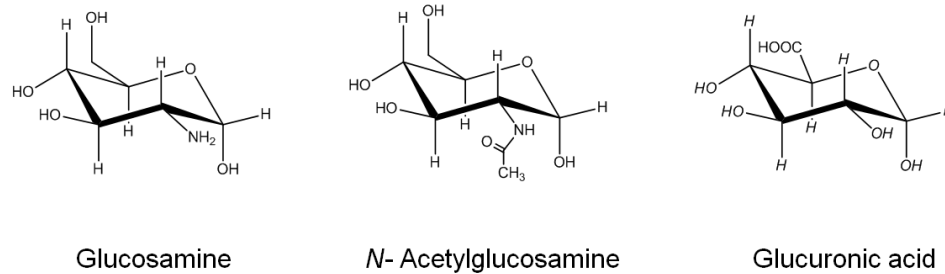


Figure 1.5 Monosaccharides that are derived from glucose through enzymatic modifications.

Glycosidic bonds can be formed between the hemiacetal group of one monosaccharide residue and a hydroxyl group on another. Depending on the anomeric configuration of C-1, either α -glycosidic bond or β -glycosidic bond can be produced. Disaccharides, oligosaccharides (DP 3-9) and polysaccharides (DP >10) are formed by monosaccharide residues that are linked by glycosidic bonds with increasing degrees of polymerization (DP). In addition to linear structures, branched structures can be formed when multiple glycosidic bonds are connected to one or more of the monosaccharides.

In eukaryotes, there are mainly three types of protein-linked glycans involved in cellular processes. 1) *N*-linked glycans are attached to the nitrogen atom on the side chain of asparagine (Asn, N) in the sequence –Asn-X-Ser- or -Asn-X-Thr- ($X \neq \text{Pro}$); 2) *O*-linked glycans are attached to the oxygen atom on a serine (Ser, S) or threonine (Thr, T) residue; and 3) Glycosaminoglycans (GAGs) are attached to a Ser residue in the sequence -Ser-Gly-X-Gly- and yield proteoglycans that are abundant on cell surfaces. GAGs are also prevalent in extracellular spaces, in locations such as connective tissues.

The functions of glycans are greatly extended when conjugated with other biomolecules. *N*-glycans are co-translationally added to proteins in the endoplasmic reticulum (ER) and facilitate protein folding; incorrect folding condemns the nascent protein to degradation. In order for the protein with the correct higher-order structures to be synthesized, the occupancy of the glycosylation sites and the structures of the glycans are strictly regulated by the levels of many glycosyltransferases and nucleotide-linked monosaccharides in the ER membrane and the Golgi.³³ Glycosylation is also found to switch the activities of a protein on and off by changing the protein structures.³⁴

Alternation in glycoforms is related to tumor progression. SLe^X and SLe^A are ligands for endogenous selectins, which are a family of proteins responsible for cell adhesion. Tumor cells can overexpress the SLe^X and SLe^A motifs and lose adhesion, leading to metastasis.³¹ In another example, viral and chemical carcinogenesis will up-regulate the transcription and expression of UDP-GlcNAc:*N*-glycan GlcNAc transferase V (GlcNAcT-V) enzyme by activating the promoter of *MGAT5* gene. As a result, the β 1-6 linkage in *N*-glycans can be greatly up-regulated. Inhibition of such *N*-glycans can reverse the tumor phenotypes.³¹ In the example of human fertilization, glycoproteins with a sialyl-Lewis X (SLe^X) motif at the non-reducing terminus has been found to play a key role in human sperm binding to the extracellular matrix coating of the oocyte.³⁵

O-glycosylation is another set of common modifications found in glycoproteins. The simplest *O*-glycosylation is a single *N*-acetylgalactosamine (GalNAc) residue attached to the Ser or Thr residue on a protein. The longer and more complex *O*-glycans are generated from the core *O*-glycan structures. *O*-glycans are also known to participate in many biological processes. For example, mucins are a class of heavily *O*-glycosylated glycoproteins. Mucins on the cell surface such as MUC1 are found to play a key role in cell adhesion. MUC1 with less degree of glycosylation is usually associated with increased rate of cancer.³¹

The in-depth understanding of glycan biological functions depends on thorough understanding of the glycan structures. Despite the importance of glycans in these crucial cellular processes, the lack of analytical tools has hampered studies of structure-function relationships of glycans. Therefore, it is necessary to develop fast, sensitive, and accurate analytical methods to decipher glycan structures.

1.2.2 Tandem mass spectrometry of glycans

Unlike proteins and nucleic acids, which have linear primary structures, glycans have multiple levels of structural complexity. The ultimate goal of glycan structural analysis is to obtain information on not only composition, but also topology, linkage patterns, and stereochemical configurations. Isomeric heterogeneities and the lack of glycan amplification methods make the glycan structural determination even more challenging.

Various chemical, enzymatic, and physical chemical methods have been developed to determine the glycan structure at different levels. The choice of the methodology depends on the quantity and purity of the glycan sample. Although nuclear magnetic resonance (NMR) spectrometry can offer complete glycan structural information, it requires a large amount of sample (> 1 mg) that is not always available for biological and clinical samples.

Recent developments of advanced MS and MS/MS techniques have added new dimensions to the structural analysis of glycans. The composition of a glycan can be easily deduced by measuring the accurate mass of a glycan. Other structural information, including topology, linkage patterns, and stereochemical configurations, can be obtained through MS/MS, but it often provides only partial definition of the structures. In order to achieve complete structural elucidation of glycans, it is necessary to understand the mechanisms of glycan fragmentation processes and to develop robust MS/MS methods to meet the challenges in the modern glycobiology research.

1.2.3 Nomenclature of glycan fragments

In 1988, in order to facilitate clear description of rich glycan fragmentation in high energy FAB MS/MS spectra, B. Domon and C. E. Costello introduced the now widely-used glycan fragmentation nomenclature.³⁶ As shown in Figure 1.6, when the charge is retained on the non-reducing end of a glycan, the corresponding fragment ions are assigned as A_i , B_i , and C_i ions, where i represents the position number counted from the

non-reducing end. If the charge is retained on the reducing end of a glycan, fragment ions are assigned as X_j , Y_j , and Z_j ions, where j represents the position number counted from the reducing end. A_i and X_j ions, highlighted in red, are designated as cleavages within a glycan ring. B_i , C_i , Y_j , and Z_j , highlighted in blue, designate as glycosidic cleavages. For primary branches, subscripts in Greek letters are used to represent the branches, with α , β , γ in the decreasing order of size. Subscript primes are used to indicate the secondary branches. For example, α' and α'' suggest there are two secondary branches coming out of the α branch, where the size of α' is larger than α'' . The bonds on the glycan ring are numbered as 0-5, starting from the O-C₁ bond (highlighted in green). The left superscripts of the cross-ring fragments (*e.g.* $^{m,n}A_i$ and $^{m,n}X_j$) indicate which ring bonds have been cleaved.

Glycosidic and cross-ring fragments carry glycan structural information at different levels.³⁶⁻³⁷ The glycosidic fragments offer information on the sequence and topology of a glycan, whereas cross-ring cleavages offer additional information on the topology and linkage patterns. Taking the *N*-glycan shown in Figure 1.6 as an example, the cross-ring cleavage $^{2,4}A_{2\alpha'}$ (m/z 223.1 for protonated species) indicates that the linkage between the *N*-Acetylglucosamine residue (GlcNAc) and the Galactose residue (Gal) is either a 1-3 or a 1-4 linkage. Another cross-ring cleavage $^{3,5}A_{2\alpha'}$ (m/z 237.1 for protonated species) indicates that the linkage between GlcNAc and Gal is either a 1-4 or a 1-6 linkage. The combination of the two cross-ring cleavages confirms the existence of a 1-4 linkage

between GlcNAc and Gal. Other linkage patterns can be deduced following the same principle.

As the topology and linkage patterns of a glycan are closely related to its biological functions as discussed in the previous sections. It is important to develop an informative, sensitive, accurate, and high-throughput MS/MS technique that is capable of producing extensive cross-ring cleavages at the LC time scale. The development of straightforward MS/MS techniques will eventually facilitate the *de novo* sequencing of unknown glycans.

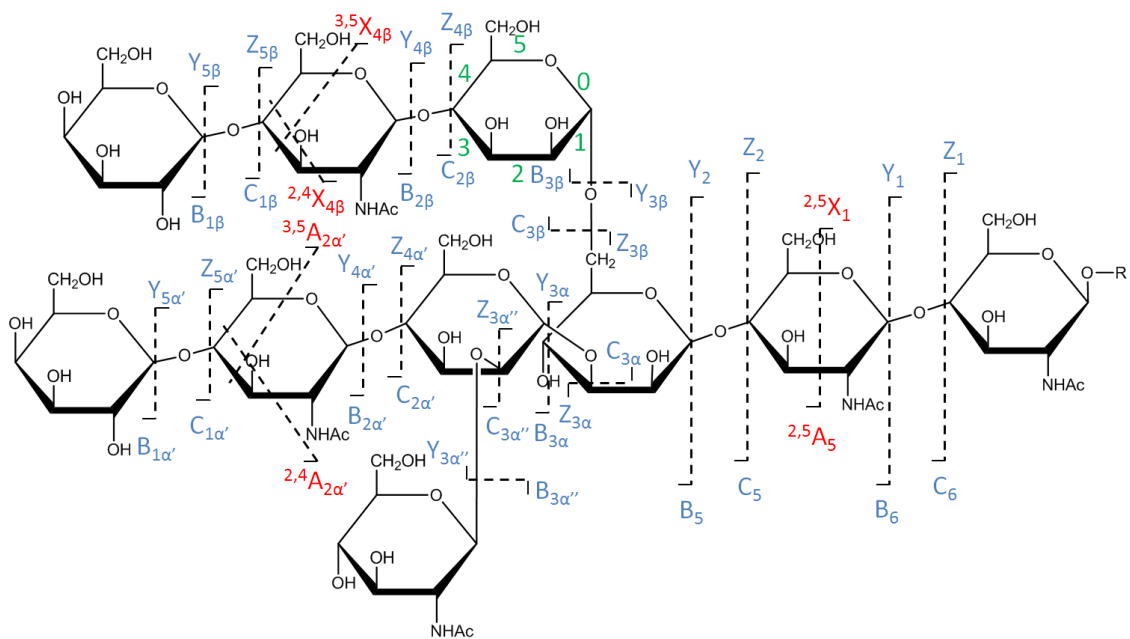


Figure 1.6 Types of MS/MS fragmentation on a hypothetical *N*-glycan. The numbering of ring bonds is highlighted in green, glycosidic cleavages are highlighted in blue, and cross-ring cleavages are highlighted in red.

1.2.4 Electron activated dissociation of glycans

Vibrational ion activation MS/MS, such as CAD and IRMPD, usually breaks the weakest bonds in a molecule. Because glycosidic bonds are weakened by adduction of the charge carrier(s), CAD and IRMPD produce mostly B/Y glycosidic cleavages and very limited linkage information can be recovered. D. J. Ashline *et al.* reported that for a given *N*-glycan, the linkage definitive cross-ring cleavages can be obtained using multiple stages of MS/MS or MSⁿ.³⁸ However, the MSⁿ approach suffers from its low throughput, low sensitivity, and its general incompatibility with on-line glycan separation methods. Considering that the potential of electronic ion activation methods in glycan sequencing remains underexplored, it is necessary to fully characterize the effectiveness of ExD in glycan structural analysis.

The first ExD experiment on glycans was reported by B. A. Budnik *et al.* in 2003.³⁹ In their work, ECD was carried out on a doubly charged chitooligosaccharides (CHOS) and produced mostly B and C ions with a series of neutral losses and hydrogen transfers. Electron-induced dissociation (EID or EInD) was also performed on the singly and doubly charged glycan precursor ions. Because the ExD mechanism for glycans was not yet defined then, glycan dissociation induced by energetic electron (8-13 eV) irradiation was called EID. To avoid confusion, in the following part of this introduction, electron-induced dissociation will be referred to as EInD, whereas electron ionization dissociation will be referred as EIoD. EInD was found to produce types of fragmentation similar to ECD, with differences only in the relative fragmentation efficiency. Some fragments

have similar relative intensities in both EInD and CAD spectra, suggesting the occurrence of vibrational ion activation. Because symmetrical structure of CHOS resulted in isomeric fragments, it was assumed that the charge was retained on the non-reducing end after fragmentation, producing B and C ions. To test whether the charge could have been retained on the reducing end, same set of experiments was carried out on an asymmetric glycoconjugate, lipotetraglucosamine. Reducing end fragments were observed, suggesting that it is possible that Y and Z ions were superimposed onto the B and C ions in the ExD spectra of CHOS. Whereas CAD produced simpler spectra with full sequence coverage for the protonated and sodiated native glycan and glycoconjugates, these ExD experiments produced complicated spectra but appeared to add no significant analytical value.

In 2005, M. A. McFarland *et al.* compared the performance of IRMPD, ECD, and EDD for characterization of the structure of the ganglioside GM1, which could be a mixture of two linkage isomers, GM1a and GM1b.⁴⁰ IRMPD produced fewer fragmentation types, even with longer irradiation time and multiple levels of laser power and evidence for the presence of the unlikely isomer GM1b was weak. IRMPD also has the risk of producing secondary fragments. Although EDD produced complementary fragments, it suffered from low fragmentation efficiency and hydrogen losses complicated the data interpretation. In contrast, with 50 ms electron irradiation, a single ECD experiment offered extensive fragmentation for both the glycan moiety and the *N*-acetyl moiety with little secondary fragmentation, allowing confident determination of the glycan sequence.

The success of ECD in the structural analysis of GM1 suggested it should be a promising technique in glycan analysis.

The successful application of EDD technique to the analysis of Glycosaminoglycans (GAGs) was reported by J. J. Wolff, *et al.* in 2007.⁴¹⁻⁴² GAGs are linear, sulfated polysaccharides that play important roles in many biological processes. The numbers and positions of sulfate groups on GAGs are of particular interest because the structural variations of sulfate groups have been found to be correlated to the biological functions of GAGs.³¹ Efforts toward the structural analysis of GAGs through conventional MS/MS techniques, such as CAD and IRMPD, have been made very difficult by the facile loss of SO₃ groups mediated by free protons.⁴³ EDD is performed by irradiating the precursor ion with 15-20 eV electrons. Results showed that EDD outperformed IRMPD by producing full sets of glycosidic and extensive cross-ring fragments for the purified tetrasaccharides⁴¹ and dermatan sulfate (DS) oligosaccharides up to 10 residues long without significant SO₃ losses.⁴² EDD is also capable of distinguishing heparan sulfate epimers that contain either glucuronic acid (GlcA) or iduronic acid (IdoA).⁴⁴ However, the low EDD efficiency and prevalent hydrogen transfers remained as a significant problem.

In 2007, J. T. Adamson and K. Håkansson carried out the first systematic study on the effect of metal cations on the ECD fragmentation of model glycans.⁴⁵ ECD experiments were performed on native maltoheptaose adducted with alkali, alkaline earth, and

transition metal cations. Compared to IRMPD, the predominant ECD fragmentation channels were found to be cross-ring cleavages at both ends of maltoheptaose, such as $^{0,2}A(^{2,4}X)$ and $^{2,4}A(^{0,2}X)$. For all the metal cations tested reported in this paper, it was difficult to produce small fragments that had fewer than 3 residues. The authors showed that AI-ECD could also be used to overcome the poor ECD fragmentation efficiency for large branched *N*-glycans. Based on the experimental observations that different metal adducts had different ECD fragmentation patterns, a hypothesis was proposed that, because the electron is captured by the metal cation, the coordination pattern between metal cations and oxygen determines the ECD fragmentation pattern. Unlike a proton, a metal cation coordinates with multiple oxygen atoms; this feature could be beneficial for the production of cross-ring cleavages during ECD.

In 2008, C. Zhao *et al.* reported that, when sodiated permethylated maltoheptaose was irradiated by 5-14 eV electrons, a condition called hot-ECD (hECD), full sets of linkage defining cross-ring cleavages could be produced.⁴⁶ This hECD method also produced rich structural information on the branching and linkage patterns of *N*-glycans, which cannot be obtained through CAD. These results suggested that the hECD technique has substantial potential in the structural analysis of a wide variety of glycans. Compared to the ECD spectrum of sodiated native maltoheptaose,⁴⁷ the hECD spectrum of sodiated permethylated maltoheptaose⁴⁶ exhibited different fragmentation behavior. It was not yet clear whether this difference is caused by variation in the electron energy or

permethylation. Also, as the kinetic energies of electrons were not consistently set from one experiment to another (5-14 eV), the reproducibility of hECD remained to be tested. The first NETD experiment on GAGs was reported by J. J. Wolff, *et al.* in 2010.⁴⁸ Their results showed that NETD produced spectra similar to EDD, but some peaks were missing from the NETD spectra, due to the lack of electron excitation. NETD not only minimized the loss of SO₃ groups, but also increased the efficiency of producing cross-ring cleavages. F. E. Leach, III, *et al.* later reran similar experiments on an FT-ICR instrument, and confirmed the assignment of NETD fragments.⁴⁹

ETD of permethylated glycans in the positive mode was investigated by L. Han and C. E. Costello, in 2011.⁵⁰ To preclude the interference of isomeric fragment ions, asymmetrical milk glycans were selected and labeled with ¹⁸O at the reducing end prior to permethylation. Compared to CID, ETD of Mg²⁺-adducted glycans produced mostly C and Z cleavages and extensive cross-ring fragments. In combination with the ETD-CID MS³ technique, the linkage patterns for a series of milk glycans could be unambiguously delineated. “Smart decomposition”, which is a gas collision ion activation technique, was used throughout the experiment to increase the ETD fragmentation efficiency by minimizing the ETnoD process. As a consequence, the observed fragmentation may originate from both ETD and CID processes.

1.3 Overview of glycan sequencing by electron activated dissociation

The ideal ion activation technique for glycan sequencing is expected to have the following characteristics: informative, sensitive and high-throughput. Although previous studies showed that the ExD techniques hold great promise for the glycan sequencing, they are still far from achieving all of the above requirements at the same time. In order to make use of the ExD techniques practical for routine glycan sequencing, it is important to address the following questions:

- (1) What are the mechanisms of ExD?
- (2) What determines the ExD fragmentation patterns?
- (3) What determines the sensitivity and throughput of ExD?

This thesis will focus on the mechanisms of ExD and their applications. The first half (chapters 2 and 3) focuses on the ExD of metal-adducted glycans. Chapter 2 presents a systematic ExD study of model glycans by varying the electron energy and metal charge carriers. Chapter 3 discusses optimization of the EED parameters to improve its efficiency, and gives a few examples of its application in glycan sequencing. This section of the thesis demonstrates that the ExD has the potential to be the experimental basis for high-throughput glycan *de novo* sequencing. The second half (chapters 4-6) addresses another important and difficult-to-characterize post-translational modification, the isomerization of aspartyl to isoaspartyl residues. In this section, the insight gained

from previous ExD studies is employed to make improvements in the characterization of peptides and proteins that contain the iso-Asp residue.

1.4 Isoaspartate characterization by electron activated dissociation

1.4.1 Asparagine deamidation and aspartate isomerization

Asparagine (Asn) deamidation is a non-enzymatic protein PTM that occurs both *in vivo* and *in vitro*.⁵¹ This process is associated with aging and protein misfolding diseases⁵¹, including neurodegenerative disorders⁵²⁻⁵³, apoptosis⁵⁴⁻⁵⁵, and autoimmunity⁵⁶⁻⁵⁷. The importance of deamidation in the proteome remains underestimated due to the lack of efficient and high-throughput analytical techniques.

Previous studies showed that the Asn deamidation rate depends on a number of factors such as protein primary sequences⁵⁸⁻⁵⁹, higher order structures⁶⁰, pH⁶¹, and temperature⁶² *etc.* For example, peptides containing the –NG– sequence have a very fast deamidation rate under high pH and high temperature conditions.⁵⁸ As shown in Figure 1.7, at pH > 4, deamidation occurs through a base-catalyzed pathway in which the nitrogen of the protein backbone attacks the carbonyl group of the Asn side chain, forming a cyclic succinimide intermediate with loss of ammonia. Carbonyl groups on this intermediate are then attacked by OH⁻ in aqueous solution and undergo hydrolysis, resulting in a mixture of aspartate (Asp) and isoaspartate (isoAsp). At pH < 3, deamination takes place *via* direct acid hydrolysis, producing only Asp.

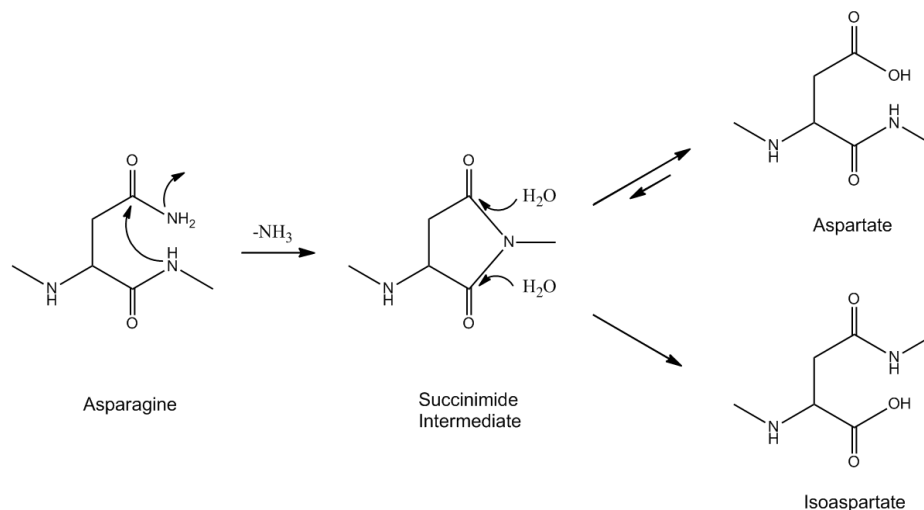


Figure 1.7 The deamidation process of asparagine.

Asp isomerization proceeds via the same succinimide intermediate as in Asn deamidation (Figure 1.7) but it is a much slower process. Although Asp isomerization might appear to be a very minor PTM, such conversion would alter the structure and bioactivity of a protein.⁶³ In order to study protein aging and misfolding diseases, it is important to identify both Asn deamidation and Asp isomerization.

1.4.2 Mass spectrometry identification of deamidation and isoaspartate formation

Deamidation can be identified by observing the mass difference between Asp and Asn, which is 0.984 Da. Because a deamidated peptide is stable in the gas phase, CAD MS/MS is capable of revealing all deamidation sites.⁶⁴

The differentiation between Asp and isoAsp is challenging, as they have identical masses, and usually requires the combination of a variety of analytical techniques. Among the tools for isoAsp determination, ECD⁶⁵ and AI-ETD⁶⁶ are capable of producing isoAsp diagnostic ions, c+57 and z-57, by breaking the C_α-C_β bond of the isoAsp residue, as shown in Figure 1.8.⁶⁵ ExD methods have been successfully implemented to characterize isoAsp formation in Alzheimer disease, amyloid disease and collagen aging.⁶⁷ However, occurrence of artifactual deamidation during tryptic digestion is a common problem when using these methods.

In a previous report, a time course study was carried out to determine the rate of artifactual deamidation during trypsin digestion using ¹⁸O isotopic labeling.⁶⁸ Results showed that the -NG- sequence in ribonuclease A underwent quick deamidation after 4 hours of trypsin digestion. Therefore, in order to identify the isoAsp without false-positives, it was recommended that the trypsin digestion be completed within 4 hours. However, the trypsin digestion is often incomplete within such a short time, and therefore it is necessary to develop an alternative isoAsp identification method that is free of artifacts.

Isoaspartic Acid

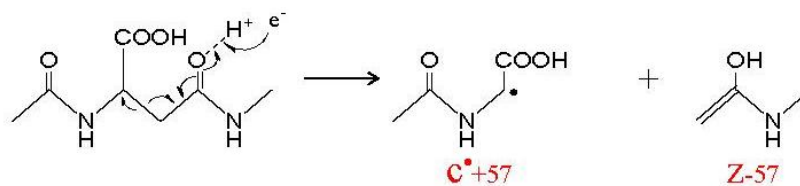


Figure 1.8 The isoAsp diagnostic ions c+57 and z-57 can be produced by ECD or ETD.

1.5 Overview of isoAsp identification by electron activated dissociation

The second half of this thesis focuses on improvement of ExD and related methods for the identification of deamidation and isoAsp formation, to develop a method which is free of false-positive results. Chapter 4 presents a comprehensive top-down MS/MS study that can identify both deamidation and isoAsp formation at the intact protein level (~ 11 kDa). Chapter 5 presents an alternative middle-down approach using Glu-C proteolysis at pH 4.0, which is particularly well suited for analysis of large proteins that are difficult to analyze using the top-down approach. Chapter 6 discusses the development and application of the in-source decay (ISD) method for isoAsp characterization with a MALDI ionization source.

1.6 Summary

Since the invention of ECD in 1998, the ExD MS/MS techniques have addressed numerous analytical challenges. Although ExD's have been widely implemented in most modern mass spectrometers, the full potential of these powerful techniques still remains underexplored. In this thesis, the ExD processes are carefully examined and new ExD techniques are developed for biological research with particular emphasis on protein and glycan characterization.

Chapter 2 Energy-Dependent Electron Activated Dissociation of Metal-Adducted Permethylated Oligosaccharides

2.1 Introduction

Oligosaccharides participate in a variety of cellular processes, such as protein folding, cell signaling, and cell-cell recognition.⁶⁹⁻⁷⁰ Better understanding of their roles in these biological processes often requires detailed structural characterization of the relevant oligosaccharides. Among the methodologies currently employed for structural analysis of oligosaccharides, tandem mass spectrometry (MS/MS or MSⁿ) has been proven to be one of the most powerful, as it offers high speed and high sensitivity, and has minimum sample requirements and capability for determination of the components in complex mixtures.⁷¹⁻⁷²

Dissociation of oligosaccharides can generate both glycosidic and cross-ring fragments.³⁶ For detailed structural analysis, cross-ring fragments are more informative, as they can be used to determine linkage types between adjacent monosaccharide residues.³⁷ For production of sufficient cross-ring fragments to fully define the oligosaccharide structure, a combination of different MS/MS methods is often necessary. Collisionally activated dissociation (CAD), or collision-induced dissociation (CID), can be easily implemented on most types of mass spectrometers and is the most commonly used method.^{37, 73-74} Low-energy CID of oligosaccharides produces mostly glycosidic fragments, which do not furnish any information on linkage types. In addition, internal monosaccharide

residue loss,⁷⁵⁻⁷⁶ fucose migration,⁷⁷ and elimination of residues that are linked through labile bonds, such as sialic acid,⁷⁸⁻⁷⁹ may further complicate the interpretation of CID mass spectra. Other slow-heating fragmentation methods such as infrared multiphoton dissociation (IRMPD)^{47, 80-81} also suffer from similar problems. High-energy CID⁸² and vacuum ultraviolet (157 nm) photodissociation (VUVPD)⁸³ result in more cross-ring cleavages, but these two fragmentation methods are not widely available. Recently, several electron activated dissociation (ExD) techniques, including electron capture dissociation (ECD)⁴⁶⁻⁴⁷ and electron transfer dissociation (ETD)⁵⁰, have been applied to oligosaccharide structural characterization, and have shown great promise. In addition, a number of dissociation methods have been developed for oligosaccharide analysis in the negative ion mode, including negative CID,⁸⁴ electron detachment dissociation (EDD),⁴¹ and negative electron transfer dissociation (nETD).⁴⁸ These methods are well suited for structural analysis of acidic oligosaccharides, such as those containing sialic acid residues or sulfate substituents.

The fragmentation behavior of oligosaccharides depends on the nature of the charge carriers.^{73, 47, 81, 85-89} The relationship between the cationizing agents and the fragmentation pattern has been well characterized for CID. Protonated oligosaccharides produce only glycosidic cleavages; larger alkali metal cations increase the dissociation threshold and are themselves often eliminated during fragmentation. Lithium and sodium were therefore suggested as the two best candidates for MS/MS analysis.^{86, 88-90} In CID, the preferred positions for glycosidic bond cleavages were found to be dependent on the

size of the alkali metal ion, whereas the types of cross-ring cleavages were not.⁸⁶ CID of oligosaccharides coordinated with divalent cations produced more abundant ions than had been observed from adduction of alkali metals.⁷³ A similar trend was also observed in ECD of native oligosaccharides.⁴⁷ While Na⁺- and K⁺-adducted maltoheptaose fragmented poorly under ECD, the alkaline-earth or divalent transition metal-adducted species underwent efficient fragmentations, producing abundant cross-ring fragments.

The amount of energy available also influences the fragmentation behavior of oligosaccharides. ECD is a softer fragmentation technique than CID. It is initiated by the dissociative recombination of electrons with polycationic molecules and generates charge-reduced radical species and product ions.²¹ Although the electron capture efficiency usually reaches its maximum at low electron energies,²² higher-energy electrons may also induce fragmentation, as observed in hot-ECD.²⁵ For peptides, in addition to the c- and z-type ions commonly observed in low-energy ECD, secondary side-chain fragments can be produced in hot-ECD, and this strategy has been utilized for isomeric residue differentiation.²⁵ When compared to CID, hot-ECD of sodium-adducted permethylated oligosaccharides was found to generate more cross-ring fragments, including types which were not present in the low-energy ECD spectra of native oligosaccharides. However, it was unclear whether the fragmentation pattern change was the result of permethylation or could be attributed to the electron energy difference between ECD and hot-ECD.⁴⁶ Although hot-ECD appears to be a valuable tool for the structural analysis of oligosaccharides, its potential has remained underexplored.

In order to better define the ExD behavior of metal-adducted oligosaccharides, a model oligosaccharide maltoheptaose was reduced and permethylated and subjected to ExD analysis under different experimental conditions. Judicious selection of the electron energy and metal charge carriers resulted in different fragmentation patterns and new types of informative fragmentation. Theoretical modeling contributed insight into the metal-dependent behavior of carbohydrates during low-energy ECD and EED.

2.2 Experimental

2.2.1 Materials

Native maltoheptaose, ribonuclease B, H₂¹⁸O (97%) water, 2-aminopyridine, acetic acid, and reagents for permethylation including dimethyl sulfoxide (DMSO), sodium hydroxide, methyl iodide, and chloroform, as well as all salts including sodium borohydride, lithium acetate, sodium acetate, potassium acetate, rubidium chloride, cesium acetate, magnesium acetate, calcium acetate, strontium chloride, and barium acetate were obtained from Sigma-Aldrich (St. Louis, MO). Glycerol-free PNGase F was obtained from Prozyme (Hayward, CA). Porous-graphitized carbon (PGC) solid phase extraction (SPE) columns were obtained from Thermo-Scientific (Springfield, NJ). Sep-Pak™ C18 SPE cartridges were obtained from Waters (Milford, MA).

2.2.2 Reducing End Reduction

Reducing end reduction was performed on maltoheptaose according to the method reported by Costello *et al.*⁹¹ Dried native maltoheptaose (~100 µg) was dissolved in 200 µL of 0.1 M NaOH / 1 M NaBH₄ for 1 h at ambient temperature. Acetic acid (10%) was then added drop by drop until bubbling ceased. PGC SPE cartridges were used for desalting of the reduction product. The PGC cartridges were pre-wetted with 100% acetonitrile followed by sequential rinses with 2 mL of 60%, 30%, and 0% acetonitrile/water, each containing 0.1% trifluoroacetic acid (TFA). The reduction product was loaded to a PGC cartridge, washed extensively with 0.1% TFA and eluted by

3 mL of 30% acetonitrile (ACN) in 0.1% TFA. The desalted and reduced maltoheptaose was then dried in a SpeedVac™ concentrator.

2.2.3 Reducing End ¹⁸O-Isotope Labeling

The reducing end ¹⁸O-isotope labeling was performed based on the method introduced by Viseux *et al.*⁹² The catalyst solution was prepared by dissolving 2.7 mg of 2-aminopyridine in 1.0 mL of anhydrous methanol. Dried native maltoheptaose (50 µg) was dissolved in 25 µL of H₂¹⁸O (97%) with 2.5 µL of catalyst solution and 1 µL of acetic acid. The solution was then incubated at 55 °C overnight. After completion of the reaction, the ¹⁸O-labeled maltoheptaose was dried in a SpeedVac™ concentrator prior to permethylation.

2.2.4 Permethylation

Permethylation was performed using the method introduced by Ciucanu and Kerek⁹³ and modified by Ciucanu and Costello.⁹⁴ The native glycan (100 µg) was suspended in 100 µL of DMSO/NaOH solution and left at room temperature for 1 h, with vortexing every 15 min. Methyl iodide (50 µL) was then added to the reaction mixture and the reaction was allowed to proceed for another 1 h, with vortexing every 15 min. Additional NaOH/DMSO (100 µL) and of methyl iodide (50 µL) were then added together, and the reaction was allowed to proceed for at least 1 h longer, with vortexing every 15 min. After the completion of the reaction, 300 µL of chloroform was added to stop the permethylation reaction and to extract the permethylated glycans. Water (400 µL) was

added to wash out the salts in the sample. The sample tubes were vortexed and centrifuged. The upper aqueous layer was removed and the organic phase was retained. The washing cycle was repeated 5-7 times.

2.2.5 Electrospray Conditions

Permethylated oligosaccharides were dissolved in 50% methanol, 20-40 μM salt solutions to a concentration of 1-5 μM for electrospray ionization (ESI) tandem MS analysis. Samples were loaded into a glass capillary tip pulled with a micropipette puller (model P-97; Sutter Instruments Co., Novato, CA) to $\sim 1\text{-}\mu\text{m}$ orifice diameter. A stainless steel wire was inserted into the sample solution on the distal end of the tip to form the electrical connection. Samples were then directly infused into the mass spectrometer ion sources.

2.2.6 Tandem Mass Spectrometry

The maltoheptaose study was carried out on a custom-built 7-T qQq-FTICR mass spectrometer equipped with an on-axis indirectly heated dispenser cathode (Heatwave, Watsonville, CA).⁹⁵⁻⁹⁶ The study of high mannose *N*-linked glycans was performed on a 12-T solariXTM hybrid Qq-FTICR mass spectrometer equipped with an indirectly heated hollow dispenser cathode (Bruker Daltonics, Billerica, MA). Experimental results were reproducible on both platforms. Target ions were isolated by a front-end quadrupole and accumulated in the collision cell for 100 to 500 ms before being transferred to the ICR cell. For low-energy ECD analysis, the precursor ions were irradiated with $\sim 1.5\text{-eV}$

electrons for 100 ms; for higher energy ExD experiments, the precursor ions were irradiated with 9- or 14-eV electrons, for up to 1 s. The cathode heating current was 1.3 A for hot-ECD and EED, and 1.5 A for ECD experiments. A 0.5 s transient was typically acquired for each scan, and each ExD spectrum shown represents the results of 100 to 200 transients summed to improve the signal-to-noise ratio.

2.2.7 Data Analysis

All spectra were zero-filled twice and Fourier transformed without apodization. The ExD spectra were calibrated internally using the precursor ion and a few fragment ions assigned with high confidence, giving a typical mass measurement accuracy better than 5 ppm (2 ppm for solariXTM spectra). Deconvoluted mass lists were generated semi-automatically by MasSPIKE⁹⁷ for spectra obtained on the custom-built FTICR instrument, or by the SNAPTM (Sophisticated Numerical Annotation Procedure) algorithm⁹⁸ using the DataAnalysisTM software (Bruker Daltonics) for solariXTM spectra. Software used to assist in data analysis included Boston University Data Analysis (BUDA, version 1.4), GlycoWorkBench,⁹⁹⁻¹⁰⁰ and a home-made Visual Basic program for auto-assignment. The nomenclature employed for designating carbohydrate fragments was that introduced by Domon and Costello.³⁶

2.3 Results and Discussion

Figures 2.1, 2.5 and 2.6 show the ExD spectra of permethylated maltoheptaose coordinated with Na^+ , Li^+ , and Mg^{2+} , respectively, acquired at three different electron energies. For each experimental condition, the bottom panel shows the spectrum in its full range, with the number above each bracket indicating, roughly, the number of monosaccharide units contained in that set of fragment ions observed within the bracketed range. The expansion of a selected m/z range is shown above each full spectrum to demonstrate the various types of fragment ions observed. Peaks resulting from glycosidic bond cleavages are labeled in blue, whereas peaks resulting from cross-ring cleavages are labeled in red. A schematic representation of all glycosidic and cross-ring fragment ions observed is shown to the left of each ECD spectrum.

2.3.1 ExD of the Sodium-Adducted Permethylated Maltoheptaose

In the 1.5 eV ECD spectrum of doubly sodiated permethylated maltoheptaose, sodium loss was the dominant fragmentation channel (Figure 2.1 a). However, at 9 eV, *i.e.*, under the hot-ECD condition, the same precursor ion underwent extensive fragmentation, generating both glycosidic and cross-ring product ions (Figure 2.1 b). Due to its symmetric structure, native or permethylated maltoheptaose can produce multiple pairs of isobaric product ions, such as B_n and Z_n , C_n and Y_n , and $^{0,2}X_n$ and $^{2,4}A_{n+1}$. In order to facilitate unambiguous peak assignment, maltoheptaose was reduced before permethylation, since this step introduces a 16-Da mass shift for all reducing end-containing fragment ions. Peak assignments were also independently verified by ^{18}O -

labeling at the reducing end of native maltoheptaose. The superior mass resolving power and mass measurement accuracy afforded by the FTICR instrument are essential for correct peak assignments, as illustrated by the peaks at m/z 1073.5 (inset), which correspond to a doublet consisting of both C_5 ($[C_5 - 2H + Na]^+$) and Z_5 ($[Z_5 + Na]^+$) ions. This pair of ions are separated from one another by 36 mDa, a common splitting seen in oligosaccharide fragment ions due to the mass difference between a CH_4 group and an O atom, requiring a mass resolving power of $\sim 60,000$ for baseline separation at this m/z value.

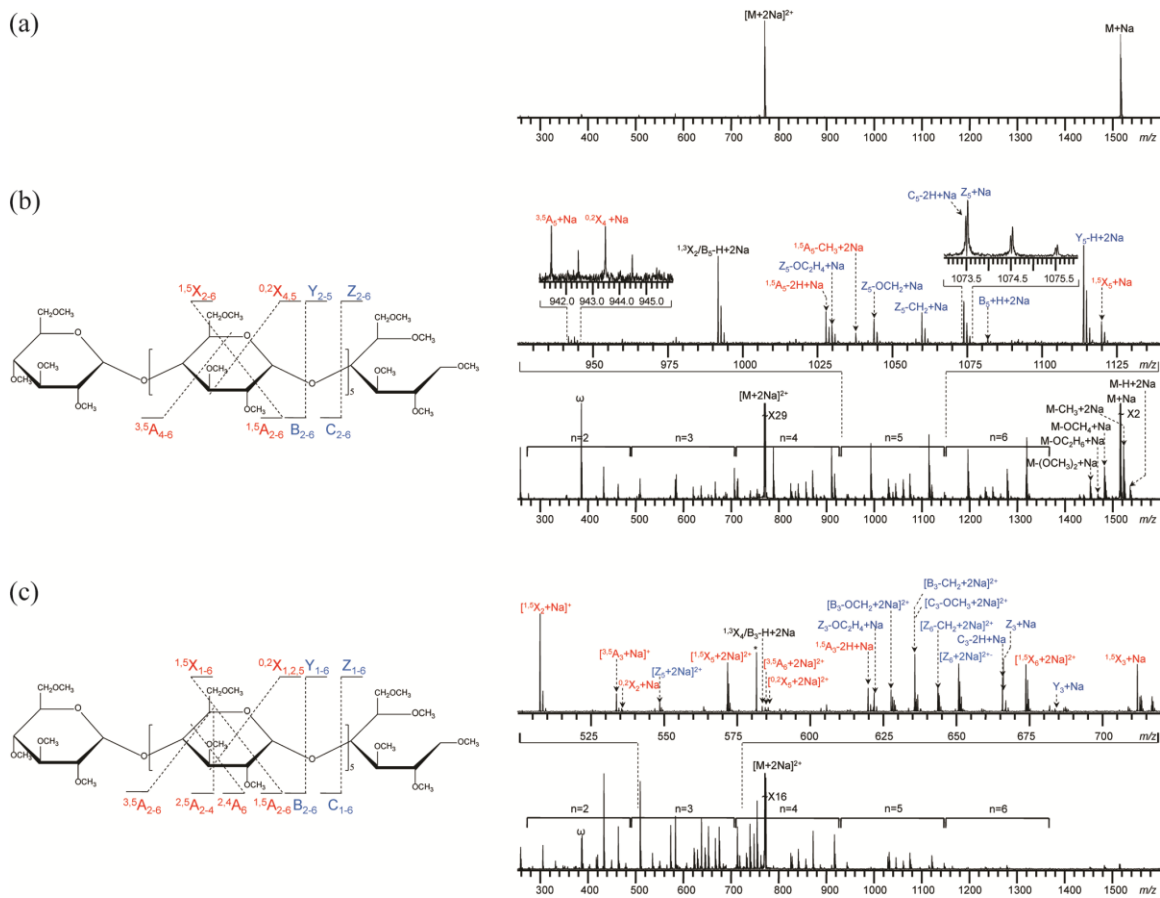


Figure 2.1 ExD spectra and cleavage maps of permethylated maltoheptaose $[M + 2Na]^{2+}$ m/z 768.3750 at different electron energy levels: (a) 1.5 eV, (b) 9 eV, and (c) 14 eV.

The majority of the fragment ions were glycosidic fragments, including C-, Y- and Z-ions, whereas $^{1,5}A$ - and $^{1,5}X$ -type product ions were the most abundant cross-ring fragments. These fragment ions are useful for sequence determination, but they do not provide linkage information. A few informative cross-ring fragment ions were also present in the hot-ECD spectrum, including $^{3,5}A$ - and $^{0,2}X$ -type ions. In comparison, Håkansson and coworkers reported that ECD of the doubly sodiated native maltoheptaose primarily

resulted in the formation of 0,2- and/or 2,4-designated A- and X-type cross ring fragments,⁴⁷ although the assignments had ambiguity due to the symmetry of the non-reduced maltoheptaose used in their study. To remove this uncertainty in peak assignment, we have now performed ECD on ¹⁸O-labeled native maltoheptaose, and have determined that the most abundant fragments are ^{2,4}A-type ions (Figure 2.2). It is interesting to note that definition of the 1→4 linkage in maltoheptaose requires both ^{3,5}A- (from hot-ECD of permethylated maltoheptaose) and ^{2,4}A-type ions (from ECD of native maltoheptaose). In the hot-ECD spectrum of permethylated maltoheptaose, a series of high-abundance fragment ions was also observed at masses ~106 Da lighter than corresponding C_n ions, and we have tentatively assigned this series as the ^{1,3}X_m/B_{7-m}-H ions (*e.g.* the ^{1,3}X₂/B₅-H ion at *m/z* ~991.4). It appears that generation of these product ions is specific to the 1,4-linkage, as they were also observed in the hot-ECD spectra (data not shown) of permethylated cellobiose (β-1,4-linkage) and mannohexaose (β-1,4-linkage), but not in those of permethylated isomaltose (α-1,6-linkage) and laminarihexaose (β-1,3-linkage).

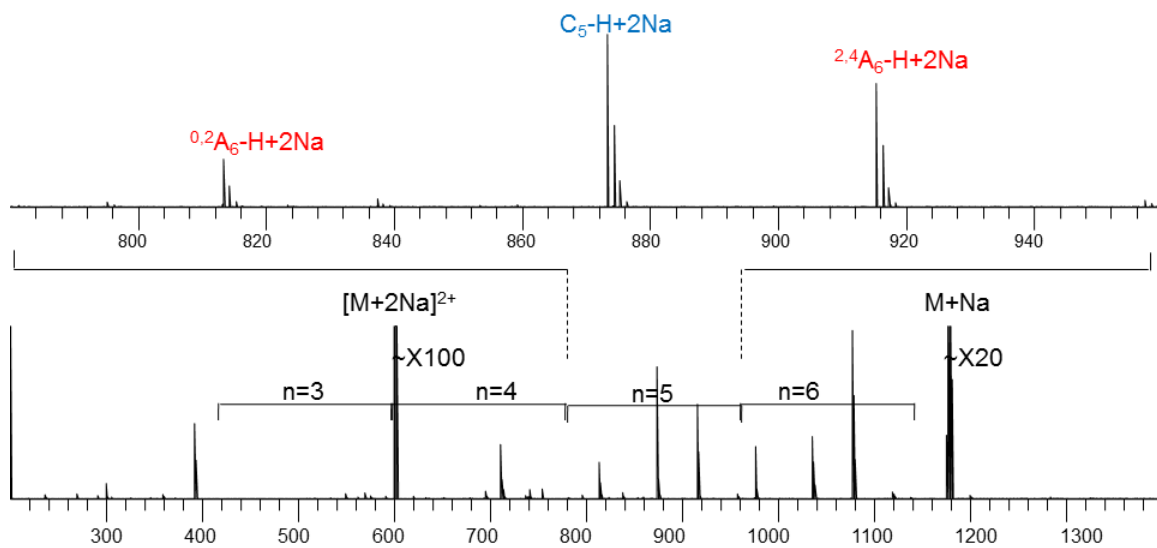
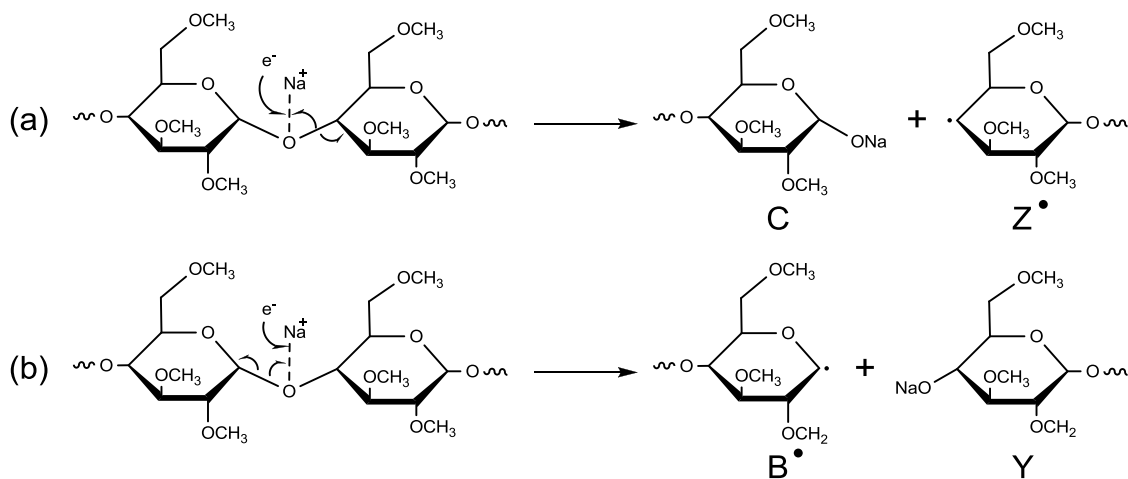
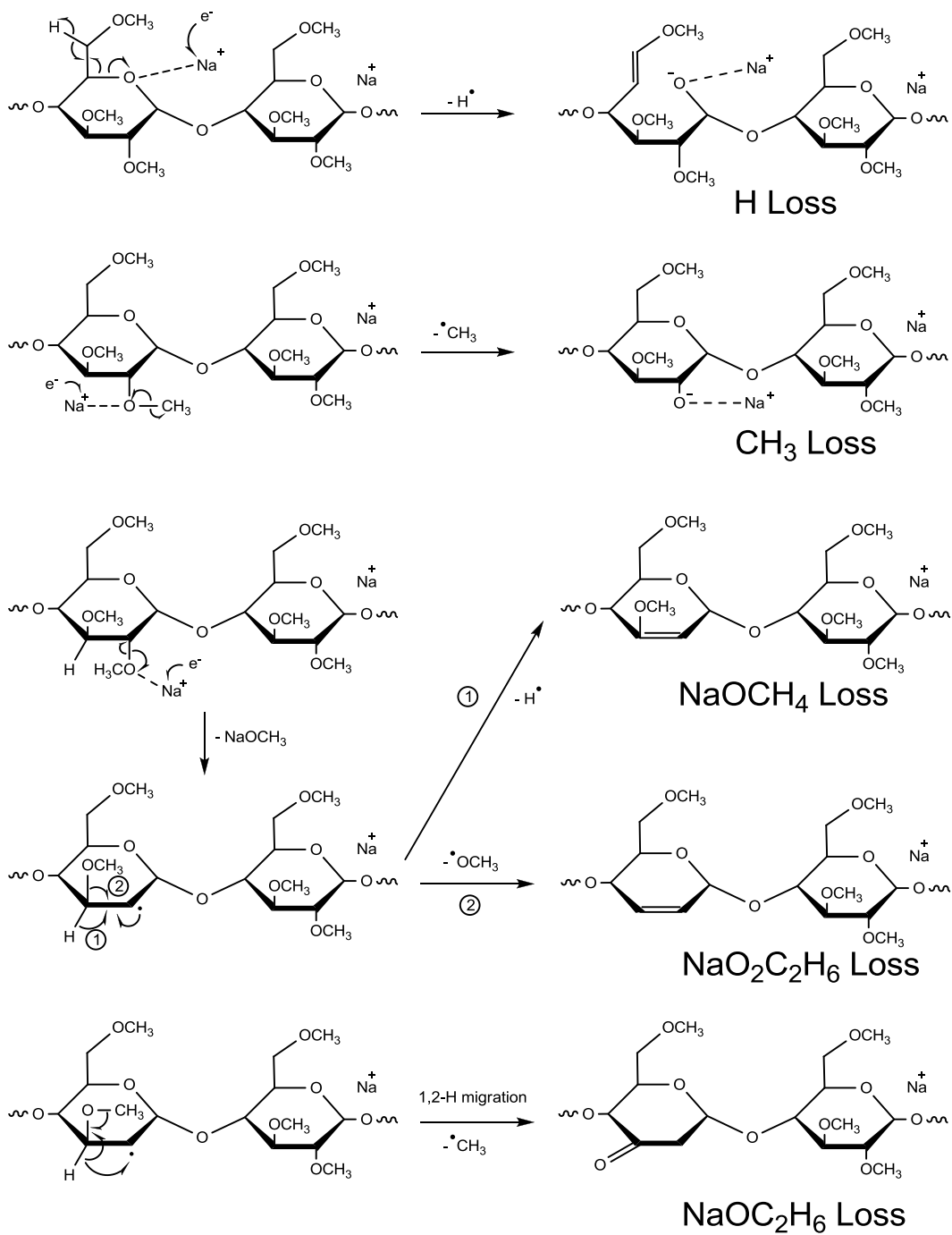


Figure 2.2 1.5-eV ECD spectrum of sodium adducted native maltoheptaose $[M + 2Na]^{2+}$ m/z 600.1815 with ^{18}O -labeled reducing end



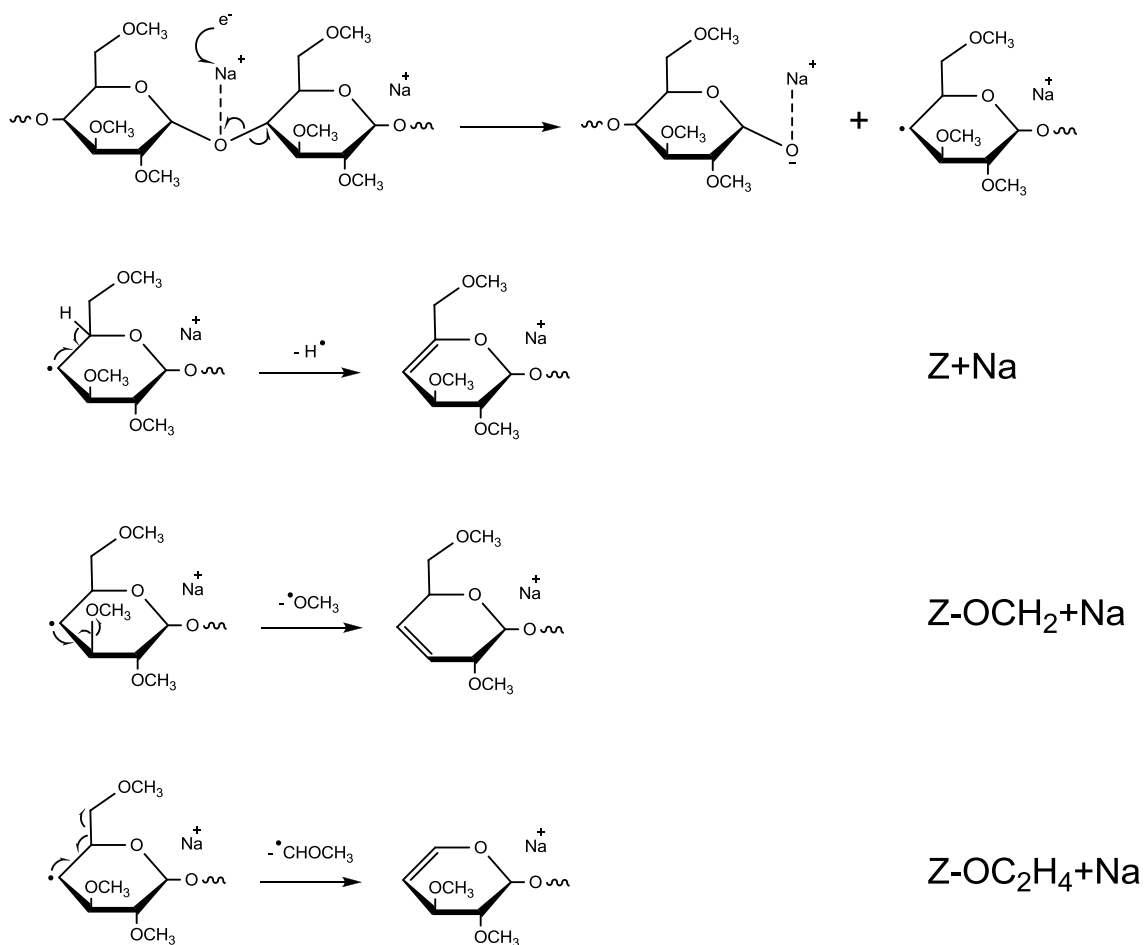
Scheme 2.1 Proposed mechanisms for the formation of (a) B^\bullet and Y ions, and (b) C and Z^\bullet ions observed in hot-ECD of reduced and permethylated maltoheptaose $[M + 2Na]^{2+}$ m/z 768.3750.

Many of the fragment ions observed in the hot-ECD spectrum of permethylated maltoheptaose, including many of the glycosidic and cross-ring fragments, were also present in its CID spectrum.⁴⁶ However, hot-ECD also produced abundant neutral losses from the charge-reduced species and from B- and Z-type ions, which were absent in the CID spectrum. No neutral losses from C- or Y-type ions were observed in the hot-ECD spectrum. This is expected, as the homolytic cleavage of the glycosidic bond after electron capture at a glycosidic oxygen-binding Na^+ will produce an odd-electron B- (or Z-) ion, and even-electron C- (or Y-) ion, depending on which glycosidic bond is cleaved and which fragment retains the charge (Scheme 2.1). Only the odd-electron B- and Z-ions can undergo further radical-induced dissociations. Possible mechanisms for several neutral losses from the charge-reduced molecular ion and from Z-ions in hot-ECD are illustrated in Schemes 2.2 and 2.3, respectively. Thus, hot-ECD is likely a radical-driven process rather than a slow-heating method, capable of producing new types of fragment ions (*e.g.*, the $^{1,3}\text{X}_m/\text{B}_{7-m}\text{-H}$ ions mentioned above) that can be used for linkage determination.



Scheme 2.2 Proposed mechanisms for neutral losses observed in hot-ECD of reduced and permethylated maltoheptaose $[M + 2Na]^{2+}$ m/z 768.3750

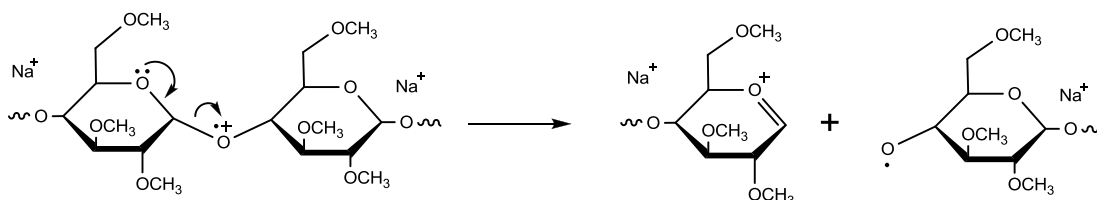
At 14 eV, the distribution of fragment ions shifted to the lower m/z region (Figure 2.1c). This shift in fragmentation pattern was partly due to the ultimate formation of smaller fragments upon irradiation at the higher energy, as reflected in the pattern of relative abundances of product ions, and partly due to the presence of doubly-charged fragments, which could not have resulted from ECD of the doubly-charged precursor ion. At the high mass end of the 14-eV spectrum, charge-reduced species and neutral losses are barely observable, further suggesting that electron capture may not play an important role here.



Scheme 2.3 Proposed mechanisms for neutral losses from Z-ions observed in hot-ECD of reduced and permethylated maltoheptaose . $[M + 2Na]^{2+}$ m/z 768.3750

One possibility is that the impact of high-energy electrons resulted in vibrational excitation (VE) of the precursor ion, as in the electron impact excitation of ions from organics (EIEIO).¹⁰¹ Since no charge reduction takes place in EIEIO, subsequent fragmentation of the vibrationally excited precursor ion can generate doubly-charged product ions. However, as a VE method, EIEIO usually produces CID-type fragments,

and cannot explain the observation of several ECD-like, doubly-charged fragments, such as those arising *via* neutral losses from B- and Z-ions.



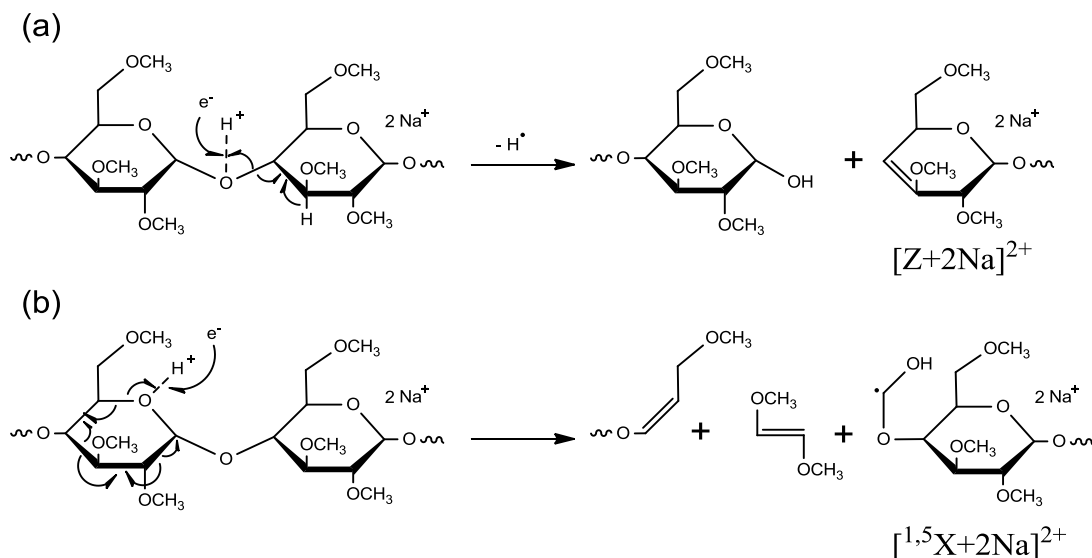
Scheme 2.4 Proposed EID mechanism for the formation of a doubly charged B ion from the doubly sodiated permethylated maltoheptaose. $[M + 2Na]^{2+}$ m/z 768.3750

A second possibility is that the precursor ion could undergo a second ionization step upon encounter with high-energy electrons, generating a radical species in a 3+ charge state that can produce 2+ fragment ions, *via* a process known as electron ionization dissociation (EID).²⁹ The most likely electron detachment site here would be an ether or acetal oxygen, which has an ionization potential of ~10 eV, well below the electron energy used. The resulting radical cation could undergo further fragmentation, similar to what occurs in electron impact ionization (EI) mass spectrometry. Scheme 2.4 illustrates a possible pathway for B- and Y-ion production *via* this EID mechanism. However, ionization alone does not necessarily lead to dissociation, and additional energy is often needed to produce fragmentation; this could be imparted through collisions with high-energy electrons. An alternative EID mechanism has been proposed by Zubarev and coworkers to explain the ECD-like fragmentation behavior of peptide and protein ions when irradiated with >20 eV electrons.²⁹ These investigators proposed that EID involves

double ionization of the precursor ion which subsequently captures one of the ejected electrons and fragments. This hypothesis was supported by their observation that abundant backbone fragments were observed only at electron energies exceeding ~40 eV, the level at which doubly-ionized species started to appear. Neither EID mechanism is likely to play a major role here, as the ~14 eV electrons had much lower energy, which was neither energetic enough to induce extensive fragmentations after single ionization nor sufficient for double ionization. Further, no triply-charged molecular or fragment ions were observed in support of either EID mechanism.

A third possibility is electronic excitation dissociation (EED), which has been invoked to explain the formation of ECD-like fragment ions upon irradiation of singly-charged peptide ions with >10 eV electrons.²⁶ In this case, the Zubarev group proposed that, following ionization, the charge (hole) could migrate to a remote site, such as the N terminus. Subsequent H-atom transfer from a carboxylic acid group would generate a peptide dication that could capture a low-energy electron and undergo fragmentation. In oligosaccharides, electron detachment from the lone pair of an oxygen atom produces an oxygen radical cation, which can abstract a hydrogen atom from a spatially adjacent carbon to form protonated oxygen. Because of its larger recombination energy, the newly protonated oxygen becomes favored, over sodiated sites, as the location for electron capture. Subsequent electron capture at the protonated oxygen can produce doubly-charged glycosidic and cross-ring fragments (Scheme 2.5). Since this charge neutralization occurs at a protonated site, all doubly-charged product ions are expected to

contain both sodium cations, consistent with the experimental observation. The EID mechanism (Scheme 2.4) would predict that doubly-charged fragment ions can carry either one or two sodium atoms, but no singly-sodiated product ions were observed experimentally.



Scheme 2.5 Proposed mechanisms for the formation of doubly charged fragment ions resulting from (a) glycosidic, and (b) cross-ring cleavages in EED of reduced and permethylated maltoheptaose. $[M + 2Na]^{2+}$ m/z 768.3750

2.3.2 ExD of Lithium-Adducted Permethylated Maltoheptaose

ExD of permethylated maltoheptaose adducted with larger alkali metal cations (K^+ , Rb^+ or Cs^+) exhibited fragmentation behavior similar to that of the sodium adducts, producing only metal loss at low electron energy, while undergoing extensive fragmentations at higher electron energies (Figures 2.3 and 2.4).

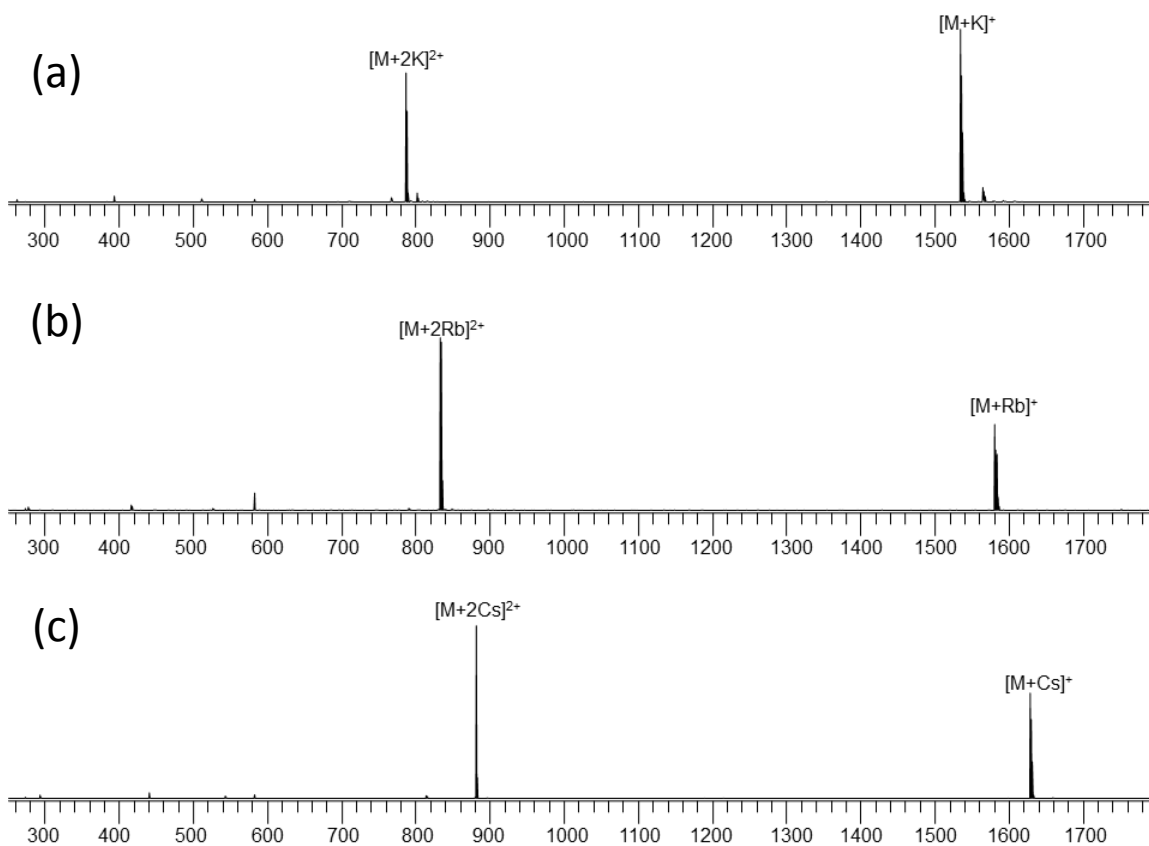


Figure 2.3 1.5-eV ECD spectra of permethylated maltoheptaose adducted with (a) K^+ , $[M + 2K]^{2+}$ m/z 784.3489, (b) Rb^+ , $[M + 2Rb]^{2+}$ m/z 830.2970, and (c) Cs^+ , $[M + 2Cs]^{2+}$ m/z 878.2907.

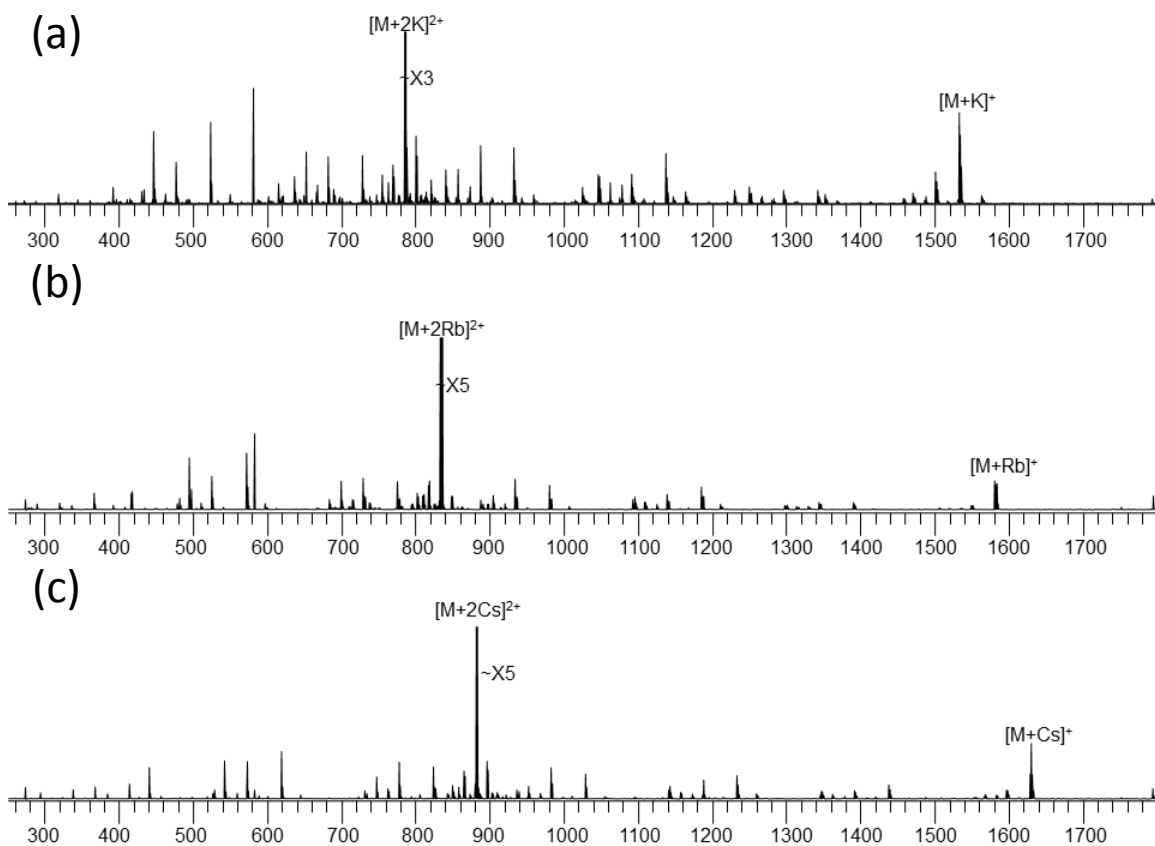
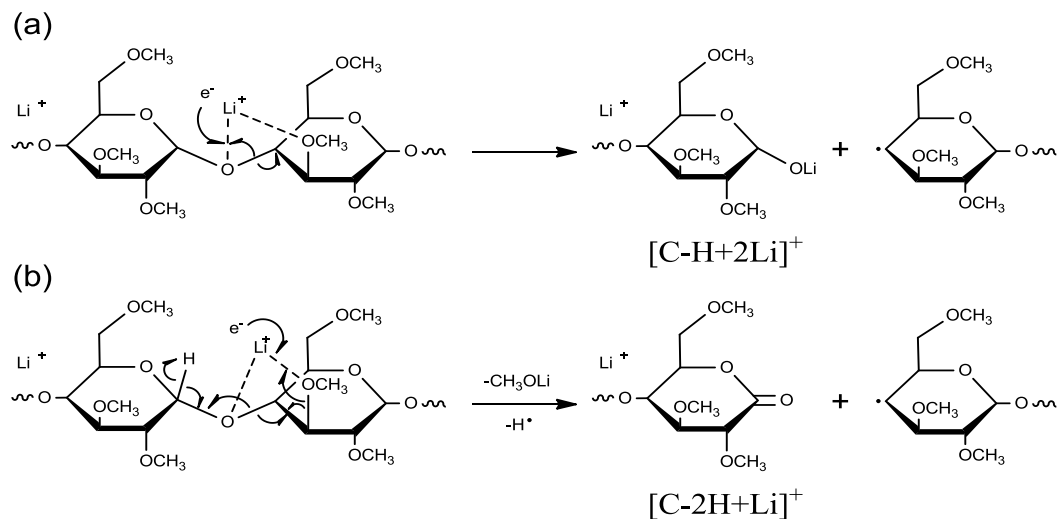


Figure 2.4 9-eV hot-ECD spectra of permethylated maltoheptaose adducted with (a) K^+ , $[\text{M} + 2\text{K}]^{2+}$ m/z 784.3489, (b) Rb^+ , $[\text{M} + 2\text{Rb}]^{2+}$ m/z 830.2970, and (c) Cs^+ , $[\text{M} + 2\text{Cs}]^{2+}$ m/z 878.2907

However, the Li^+ adduct readily fragmented at 1.5 eV (Figure 2.5a), indicating that the ECD fragmentation threshold has a dependence on the charge carrier. At higher energies, the hot-ECD (Figures 2.5b) and EED (Figures 2.5c) spectra of lithiated and sodiated (Figure 2.1b, c) permethylated maltoheptaose had many parallel features. The types of fragments present were very similar, except for a few low-abundance cross-ring fragments and neutral losses. Thus, although the identity of the metal charge carrier still

As in the case of the Na^+ adduct, the electron energy was observed to have a very strong effect on the fragmentation behavior of the Li^+ -adducted permethylated maltoheptaose. At 1.5 eV, the vast majority of product ions contained two lithium atoms, with C-type ions ($[\text{C}_n - \text{H} + 2\text{Li}]^+$) being the most abundant. At 9 eV, product ions containing both one and two lithium atoms were observed, and Y-type ions ($[\text{Y}_n - \text{H} + 2\text{Li}]^+$) became the most abundant glycosidic fragments. At 14 eV, doubly-charged fragment ions were produced, the abundance of Y-type ions diminished, and the C-type ions ($[\text{C}_n - 2\text{H} + \text{Li}]^+$) became one of the most abundant sets of glycosidic fragments. It is important to note that many seemingly similar types of fragment ions observed at different energies were actually different species, likely produced by different processes. For example, at 1.5 eV, the only C-type ions produced were $[\text{C}_n - \text{H} + 2\text{Li}]^+$ ions, with a possible mechanism for their formation illustrated in Scheme 6a. At 14 eV, only $[\text{C}_n - 2\text{H} + \text{Li}]^+$ ions were observed; these could be produced *via* the mechanism shown in Scheme 6b.



Scheme 2.6 Proposed mechanisms for the formation of (a) $[C-H+2Li]^{2+}$ by low-energy ECD, and (b) $[C-2H+Li]^{2+}$ by hot-ECD.

As was observed for the sodiated species, an increase in the electron energy shifted the distribution of the Li^+ adducts to favor formation of smaller ions. For example, the range of C- and Y-type ions produced changed from C_{3-6} and Y_{3-6} at 1.5 eV to C_{2-6} , and Y_{2-6} at 9 eV, and to C_{1-5} and Y_{1-5} at 14 eV. One possible explanation is that the production of small fragments requires the charge neutralization site to be near an end (reducing or non-reducing) to initiate cleavage, and its successful detection requires the remaining charge-carrying Li^+ to be coordinated at the same end. The proximity of the two charge carriers would cause significant Coulombic repulsion, and such a conformer would only be accessible at higher energies. EED may also contribute to this shift by allowing smaller fragment ions to be generated and detected from thermodynamically more favored conformers where the two charge carriers are farther apart, because the EED cleavage is initiated by charge neutralization at a protonated site without the involvement of either

metal charge carrier. Finally, it is also possible that, under the EED conditions, the more energetic initial products could undergo further fragmentation to generate abundant low m/z fragments, as is observed in EI mass spectra.

2.3.3 ExD of Alkaline Earth Metal-Adducted Permethylated Maltoheptaose

Previous reports suggested that divalent cation-adducted oligosaccharides can produce more abundant and informative fragment ions than are produced by alkali metal-coordinated species under low-energy ECD and ETD conditions.^{47, 50} Thus, the electron-energy dependence of the fragmentation behavior of alkaline earth metal coordinated oligosaccharides was further investigated here. The ExD spectra of Mg^{2+} -adducted permethylated maltoheptaose are shown in Figure 2.6. For the most part, the ExD behavior of the Mg^{2+} adduct resembled that of the Li^+ adduct, which underwent extensive fragmentation at 1.5 eV, and produced abundant EED fragments (as exemplified by the presence of doubly-charged fragment ions) at 14 eV. However, ECD of the Mg^{2+} adduct produced a slightly broader range of fragments, possibly because it does not need to overcome Coulombic repulsion to adopt conformations producing small fragments. Further, unlike those of the alkali metal adducts, the ExD spectra of the Mg^{2+} adduct underwent minimal change when the electron energy was raised from 9 to 14 eV: the range of observed fragments did not shift towards smaller fragments, and no new members of the $^{3,5}A_n$ ion series were produced. One explanation is that EED of the alkali metal adducts was initiated by electron capture at the protonated site, and this could produce cleavages distant from the original metal binding sites, whereas Mg^{2+} remained

as the preferred electron capture site owing to its much higher recombination energy. Maltoheptaose adducted with other alkaline metals (Ca^{2+} , Sr^{2+} and Ba^{2+}) showed similar energy-dependent ExD fragmentation behavior and will not be discussed further.

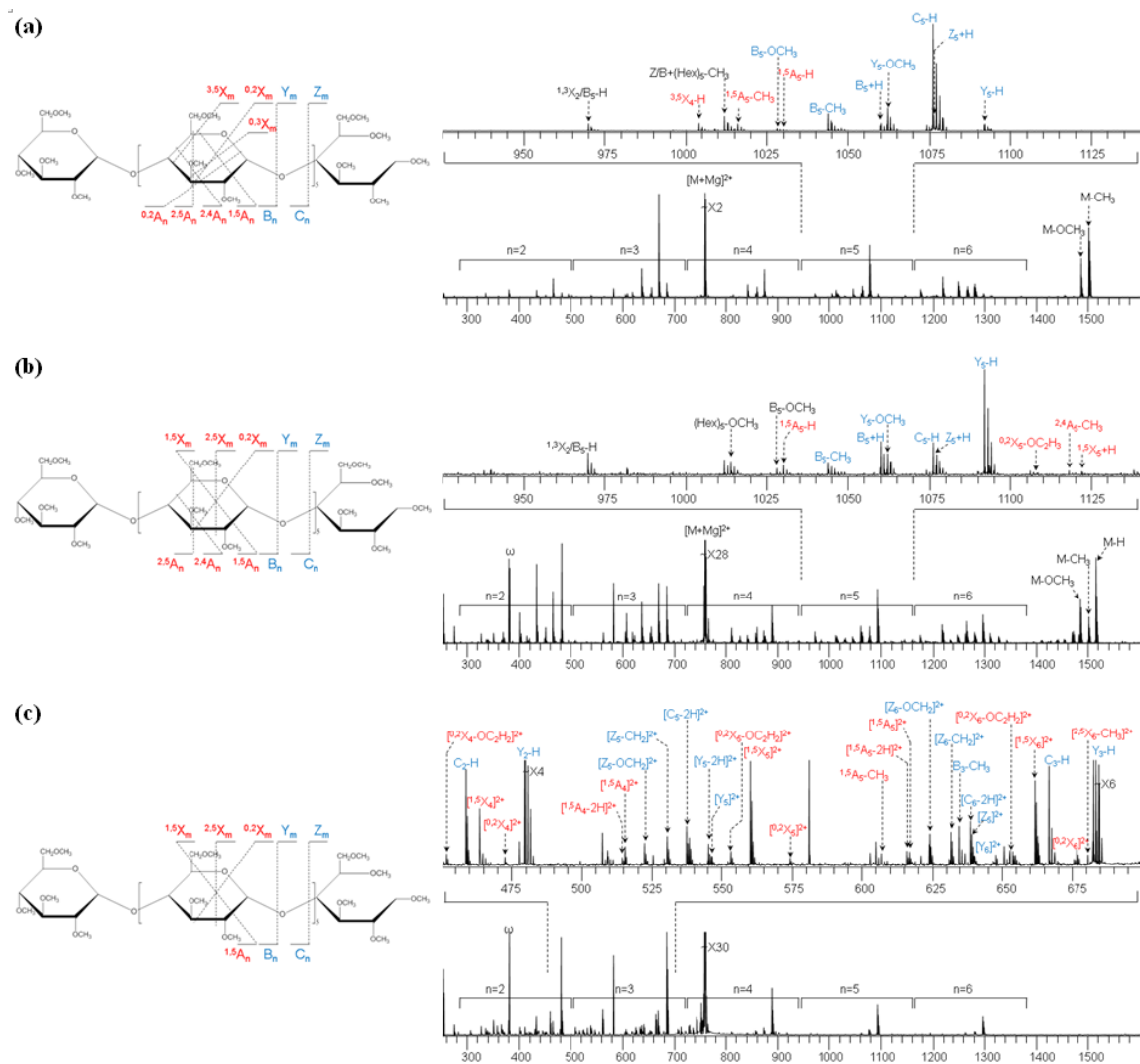


Figure 2.6 ExD spectra of Mg^{2+} -adducted permethylated maltoheptaose $[M + \text{Mg}]^{2+}$ m/z 757.3778 at different electron energy levels: (a) 1.5 eV, (b) 9 eV, and (c) 14 eV

Table 2.1 summarizes the ExD fragments observed, at three different electron energies, from permethylated maltoheptaose with Li^+ , Na^+ , Cs^+ and Mg^{2+} adductions. Although the Mg^{2+} adduct provided the most information under low-energy ECD conditions, its favorable performance was surpassed the results from analyses that used the alkali metal adducts at higher energies. The largest alkali metal (Cs^+) adduct in this set generated a wider range of fragment ions than the Li^+ and Na^+ adducts, possibly because Cs^+ can simultaneously coordinate with oxygen atoms that may be located in several monosaccharide units than can the smaller metals Li^+ or Na^+ , and this property allows it to initiate fragmentation at more positions. Considering that 0,2-, 2,4- and 3,5- types of cross-ring cleavages are the most informative, EED of the Cs^+ -adduct seemed to offer an advantage for linkage analysis.

n=	1.5 eV				9.0 eV				14.0 eV			
	2Li ⁺	2Na ⁺	2Cs ⁺	Mg ²⁺	2Li ⁺	2Na ⁺	2Cs ⁺	Mg ²⁺	2Li ⁺	2Na ⁺	2Cs ⁺	Mg ²⁺
B _n	3-6	/	/	2-6	2-6	2-6	2-6	2-6	2-6	2-6	1-6	2-6
Y _n	3-6	/	/	2-6	2-6	2-5	1-6	2-6	1-5	1-6	1-6	1-6
C _n	3-6	/	/	2-6	2-6	2-6	1-6	2-6	1-5	1-6	1-6	2-6
Z _n	3-6	/	/	2-6	2-6	2-6	1-6	2-6	1-6	1-6	1-6	2-6
^{0,2} A _n	4-5	/	/	6	5,6	/	/	/	4	/	/	/
^{1,5} A _n	3-6	/	/	3-6	3-6	2-6	2-6	2-6	2-6	2-6	1-6	3-6
^{2,4} A _n	/	/	/	3	/	/	4-6	5,6	/	6	4-6	/
^{2,5} A _n	2,4,5	/	/	3,4	/	/	/	6	/	2-4	2-4	/
^{3,5} A _n	/	/	/	/	4-6	4-6	4-6	/	2-6	2-6	2-6	/
^{0,2} X _n	3-5	/	/	2,3,6	3-6	4,5	4-6	3,5,6	1-2	1,2,5	2-6	3-6
^{1,5} X _n	/	/	/	/	2-5	2-6	1-6	2-6	1-6	1-6	1-6	3-6
^{2,5} X _n	/	/	/	/	/	/	/	1	/	/	/	1,6
^{3,5} X _n	3-5	/	/	2-5	/	/	/	/	/	/	/	/

Table 2.1 Summary of the glycosidic and cross-ring fragments observed in ExD of permethylated maltoheptaose adducted with Li⁺, Na⁺, Cs⁺, or Mg²⁺ at three different electron energy levels.

2.3.4 Theoretical Modeling of Glycan ECD

While all metal-adducted maltoheptaoses underwent extensive fragmentation when irradiated with high-energy electrons, their fragmentation behaviors differed drastically at lower energies. For the Na^+ , K^+ , Rb^+ and Cs^+ adducts, metal loss was the dominant channel (Figures 2.1a and 2.3), whereas for the Li^+ and alkaline earth metal adducts (Figures 2.2a and 2.6), the most abundant fragment ions were the C-type ions and the products resulting from methyl loss, the latter of which would correspond to the C_7 ion, if the methyl radical is eliminated from the reducing end. The Mg^{2+} adduct fragmented more extensively under low-energy ECD conditions, probably because it has a much higher recombination energy (second IP of Mg is ~ 15 eV) than alkali metals (*e.g.*, the first IP of Cs is ~ 3.89 eV). However, the drastic difference between the low-energy ECD behaviors of the Li^+ and Na^+ adducts was somewhat surprising, considering that their first ionization potentials are fairly close (Li: 5.39 eV, Na: 5.14 eV). It was also interesting to note that, when the doubly charged precursor ion contained both Li^+ and Na^+ , Na loss was still the predominant fragmentation channel at 1.5 eV (Figure 2.7a). At 9 eV, the $[\text{M} + \text{Li} + \text{Na}]^{2+}$ species fragmented extensively, producing a mixture of product ions that contained either Na^+ or Li^+ or both, which indicated that either Li^+ or Na^+ could serve as the neutralization site initiating fragmentations (Figure 2.7b).

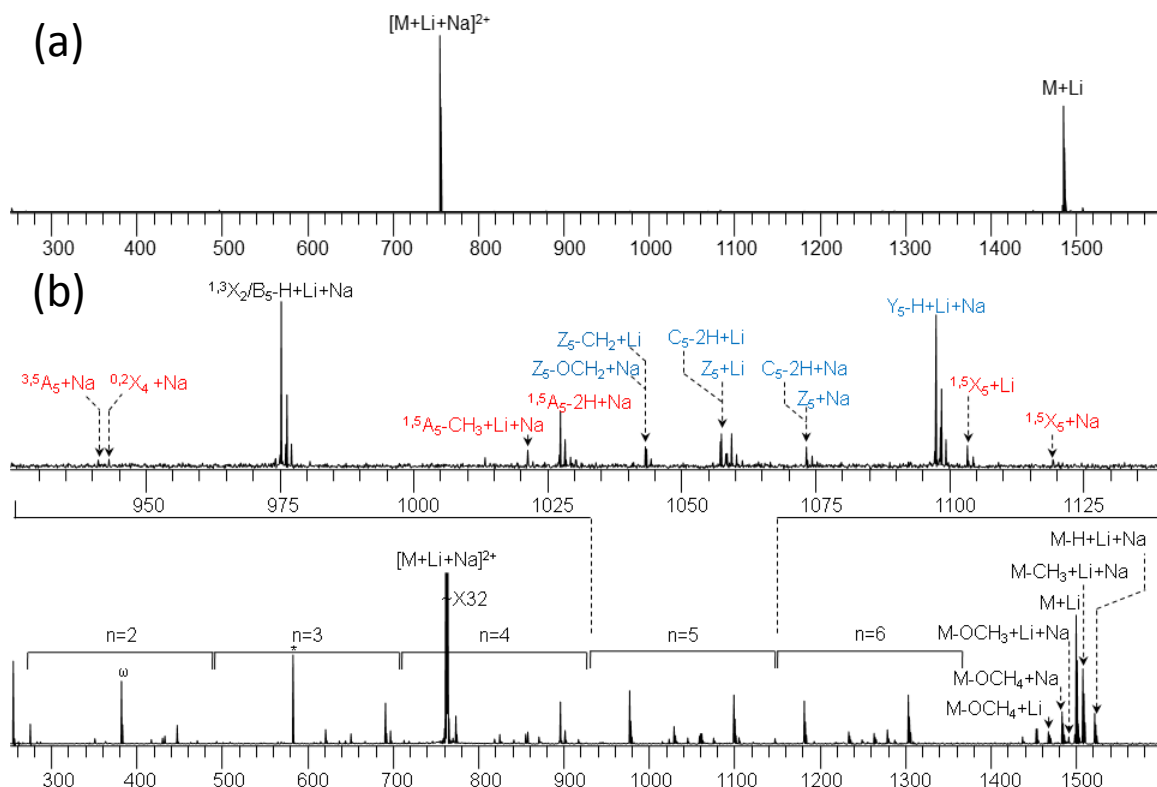


Figure 2.7 ExD spectra of the hybridly adducted permethylated maltoheptaose $[M + Li + Na]^{2+}$ m/z 760.3881 acquired at (a) 1.5 eV and (b) 9 eV electron energy.

These phenomena can be rationalized using theoretical modeling carried out on alkali-metal coordinated β -methyl-glucosides (GlcOMe) as the corresponding model systems. The Na^+ -GlcOMe complex has a larger recombination energy (85 kcal/mol) than the Li^+ -GlcOMe complex (79 kcal/mol). Figure 2.8 illustrates the potential energy surfaces (PESs) for the metal loss and methyl loss channels of the Li^+ - or Na^+ -adducted GlcOMe, as calculated at the B3LYP/6-31g(d) level of theory. For the Li^+ adduct, Li loss is 20 kcal/mol endothermic relative to the charge-reduced species, whereas the methyl loss

channel is 6 kcal/mol exothermic with an energy barrier of 12 kcal/mol (Figure 2.8a). Therefore, methyl loss is both thermodynamically and kinetically favored over Li loss. For the Na⁺ adduct, although methyl loss and Na loss have similar exothermicities, the methyl loss channel is associated with a 24 kcal/mol energy barrier, while Na loss is barrier-less, making Na loss the preferred fragmentation pathway (Figure 2.8b). By analogy, the initial electron capture for the [M + Li + Na]²⁺ of permethylated maltoheptaose is likely to occur at the Na⁺ site, leading to predominant Na loss, consistent with the experimental observation (Figure 2.7).

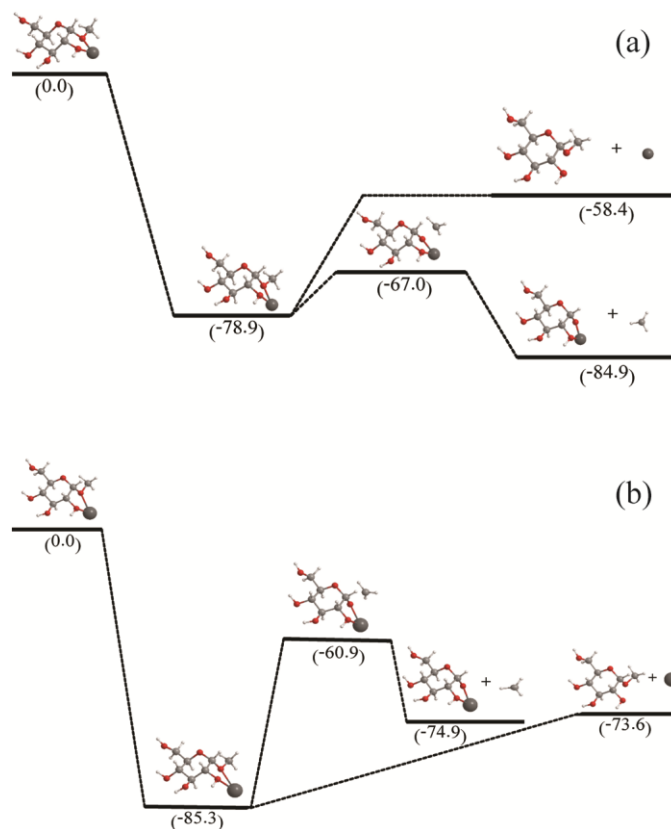


Figure 2.8 The unscaled potential energy surfaces of the methyl and metal loss channels of (a) [Glc-OMe + Li]⁺ and (b) [Glc-OMe + Na]⁺ complexes upon electron capture, as calculated at the B3LYP/6-31G(d) level of theory. Numbers in brackets are in units of kcal/mol.

Therefore, the ECD threshold depends not only on the recombination energy of the charge carrier, but also on the detailed PESs for the metal loss and bond dissociation channels. However, at higher electron energies, the relatively small differences in recombination energies and activation barriers became less important, as was reflected by the similarity in the hot-ECD spectra of the Li⁺ and Na⁺ adducts (Figures 2.5b and 2.1b),

as well as by the presence of both Li^+ - and Na^+ -adducted fragment ions in the hybrid adduct spectrum (Figure 2.7b). The details in fragmentation patterns, including both the types and ranges of fragments generated, were still metal-dependent at higher energies, *e.g.*, in hot-ECD and EED spectra of the alkali metal adducts, as shown in Table 2.1. This was also true at lower energies, where the Li^+ and Mg^{2+} adducts displayed substantial differences in the types and ranges of fragment ions produced. Theoretical calculations by Leary and coworkers showed that Li^+ and Mg^{2+} have different binding patterns with monosaccharides.¹⁰² Thus, a hypothesis may be made that, once the energy requirement is met for fragmentation to occur, it is the coordination pattern between the metal and the oligosaccharide that determines which fragments are actually produced. As we have shown herein, complementary information can be obtained by conducting ExD experiments using different metal charge carriers at different electron energies.

2.3.5 Theoretical Modeling of Glycan EED

To the best of our knowledge, there has been no mechanistic study on EED of metal-adducted oligosaccharides. Considering the superior performance of EED in glycan linkage analysis, a better understanding of the EED behavior of oligosaccharide will not only help with the optimization of the EED parameters but also facilitate accurate spectral interpretation.

The cellobiose- Na^+ complex was chosen as the model system for theoretical EED mechanistic studies. The EED spectrum and the fragmentation map of cellobiose- Na^+ are shown in Figure 2.9. The mass measurement accuracy for all assigned peaks is better than 1 ppm. The most abundant product ion in the EED spectrum of Na^+ -adducted cellobiose is $^{3,5}\text{A}_2$, and this assignment was confirmed by reducing-end ^{18}O -labeling. The second most abundant fragment ion was determined similarly as $^{1,5}\text{X}_1$. Other, less abundant, cross-ring fragments were also detected in the EED spectrum. In addition, fragments resulting from the glycosidic bond cleavage (B_1 , C_1 , Y_1 and Z_1) were present in lower abundances, together with some neutral loss fragment ions.

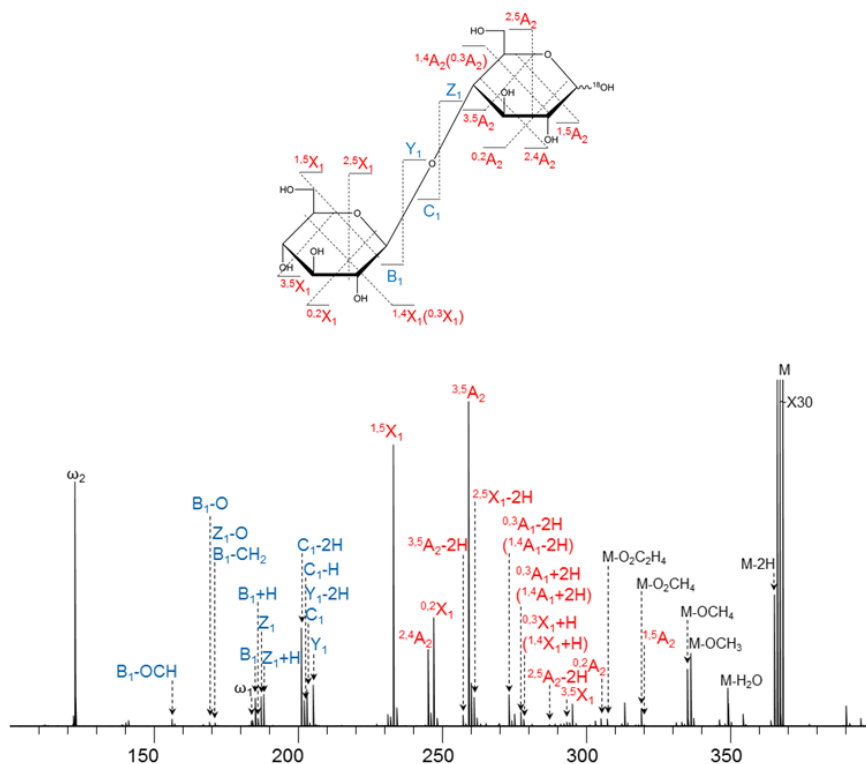


Figure 2.9 The EED spectrum of the Na^+ -adducted and ^{18}O -labeled cellobiose acquired at an electron energy of 14 eV.

Based on the theoretical calculation performed by Dr. Yiqun Huang, we proposed a novel EED mechanism which claims that when subjected to high energy electron irradiation the cellobiose- Na^+ complex is ionized to form a mixture of a doubly charged radical cation and two ring-opening distonic ions. Upon recapture of the low energy electron released during the ionization step, the radical cation may undergo EIEIO type of dissociation, resulting in glycosidic bond cleavage, whereas the two ring-opening distonic ions form di-radicals with trivial singlet-triplet splitting. The triplet states of the di-radicals can undergo radical driven alpha cleavages to form both $^{3,5}\text{A}_2$ (Figure 2.10) and $^{1,5}\text{X}_1$ (Figure

2.11), the two most abundant fragment ions observed in the EED spectrum of Na^+ -cellobiose.

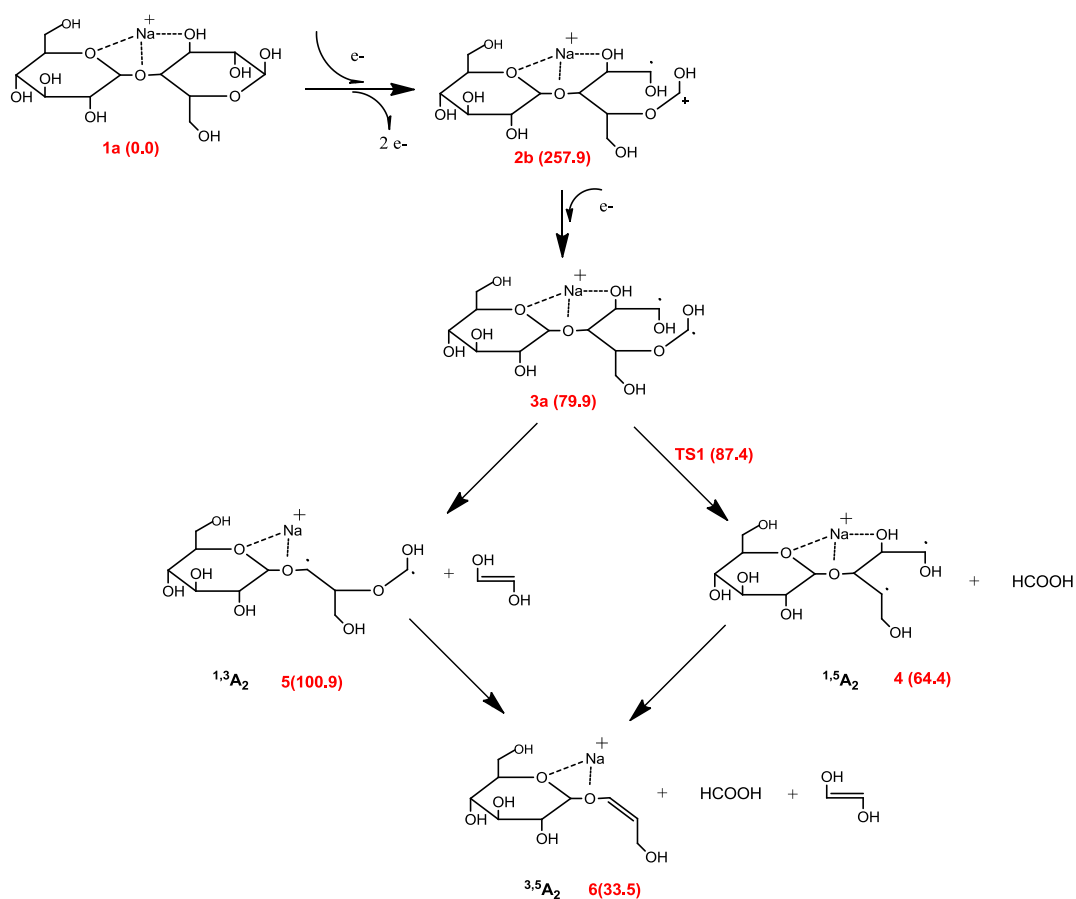


Figure 2.10 The triplet potential energy surface for the EED of cellobiose- Na^+ complex to form $^{3,5}\text{A}_2$ ion, as calculated at the B3LYP/6-31G(d) level of theory. The numbers in brackets are zero Kelvin enthalpy ^0H relative to structure 1a and with unit of kcal/mol.

(Data courtesy of Dr. Yiqun Huang)

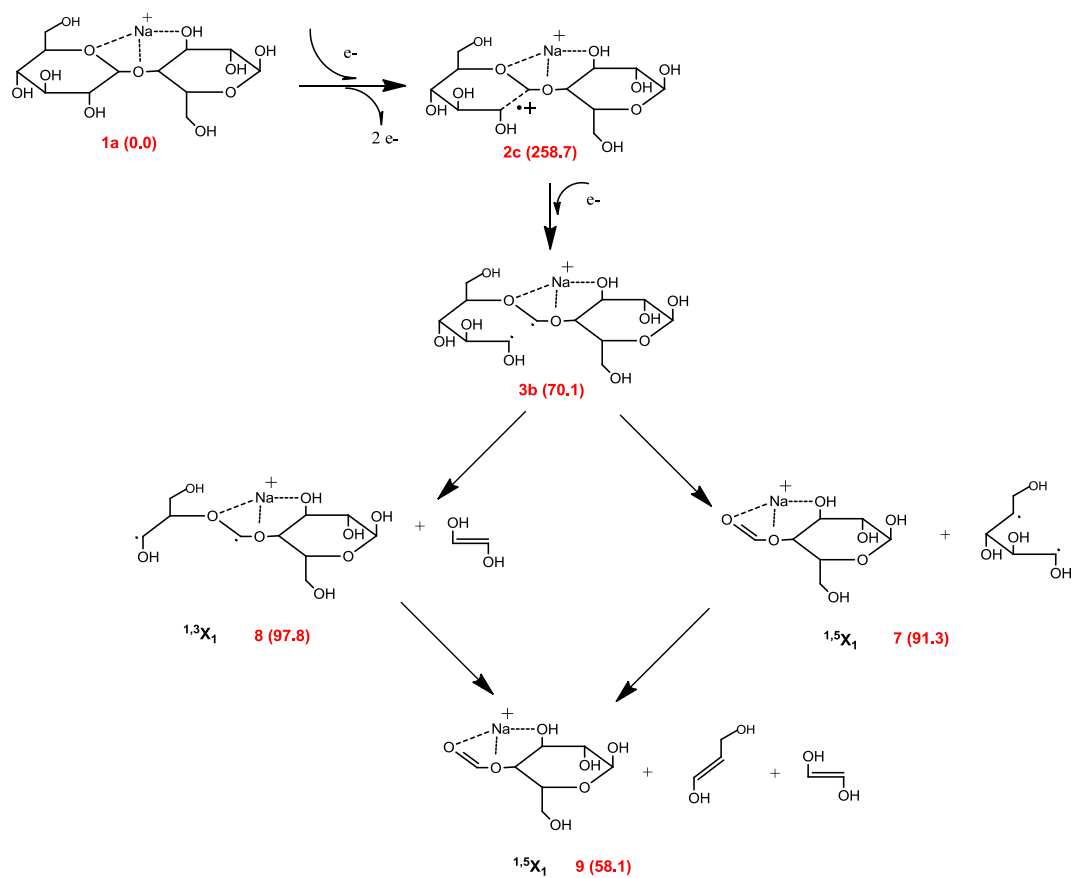


Figure 2.11 The triplet potential energy surface for the EED of cellobiose- Na^+ complex to form $^{1,5}\text{X}_1$ ion, as calculated at the B3LYP/6-31G(d) level of theory. The numbers in brackets are zero Kelvin enthalpy ^0H relative to structure 1a and with unit of kcal/mol. (Data courtesy of Dr. Yiqun Huang)

2.4 Conclusions

Using maltoheptaose as the model system, the ExD fragmentation behaviors of metal-adducted permethylated oligosaccharides were investigated. At low electron energies, adducts formed with divalent alkaline metals or lithium produced abundant glycosidic and cross-ring cleavages, whereas adducts containing larger alkali metals generated predominantly metal losses. This metal-dependent ECD fragmentation behavior was rationalized on the basis of theoretical modeling and could be attributed to the difference in the metal cation recombination energies and the detailed PESs that governed various dissociation channels.

At higher energies, hot-ECD and EED processes took over, generating types of fragments different from those that had been observed in low-energy ECD, and often yielding a broader range of fragments as well. The types and ranges of fragments observed depended on the specific metal-oligosaccharide binding patterns, which were influenced by both the electron energy and the metal charge carriers.

EED on cellobiose cationized with Na^+ was carried out and a novel mechanism for its EED behavior was revealed by theoretical calculation. The proposed ionization-recapture mechanism can successfully explain formation of the most abundant fragment ions observed in the EED spectrum of Na^+ -cellobiose complex, and is consistent with the observed metal charge carrier-independence of the EED process.

Chapter 3 Detailed Glycan Structural Characterization by Electron Activated Dissociation

3.1 Introduction

Glycans play vital roles in many biological processes, including immunological response, inflammation, and cancer metastasis.^{31, 70} The multilateral functions of glycans derive from their structural diversity. Unlike a linear biopolymer, such as an oligonucleotide or a protein, whose primary structure is uniquely defined by its one-dimensional sequence, a glycan is built from multivalent monosaccharide units, giving rise to a large number of potential topological and linkage isomers. Thus, detailed glycan structural characterization requires determination of not only its topology, but also its linkage configuration. This analytical challenge is further exacerbated by the lack of glycan amplification methods, and the presence of many closely-related structures in most naturally-occurring glycan mixtures. Among the current methodologies, tandem mass spectrometry (MS/MS) is one of the most powerful owing to its specificity, low sample requirement, and compatibility with chromatographic separation methods. However, the conventional collision-induced dissociation (CID)-based tandem MS method often fails to produce sufficient numbers of the cross-ring fragments that are crucial for linkage determination.⁷² Although multistage tandem MS analysis (MSⁿ) can potentially provide more exhaustive linkage information, the MSⁿ approach suffers from its low throughput

and sensitivity, as well as its general incompatibility with on-line glycan separation methods.

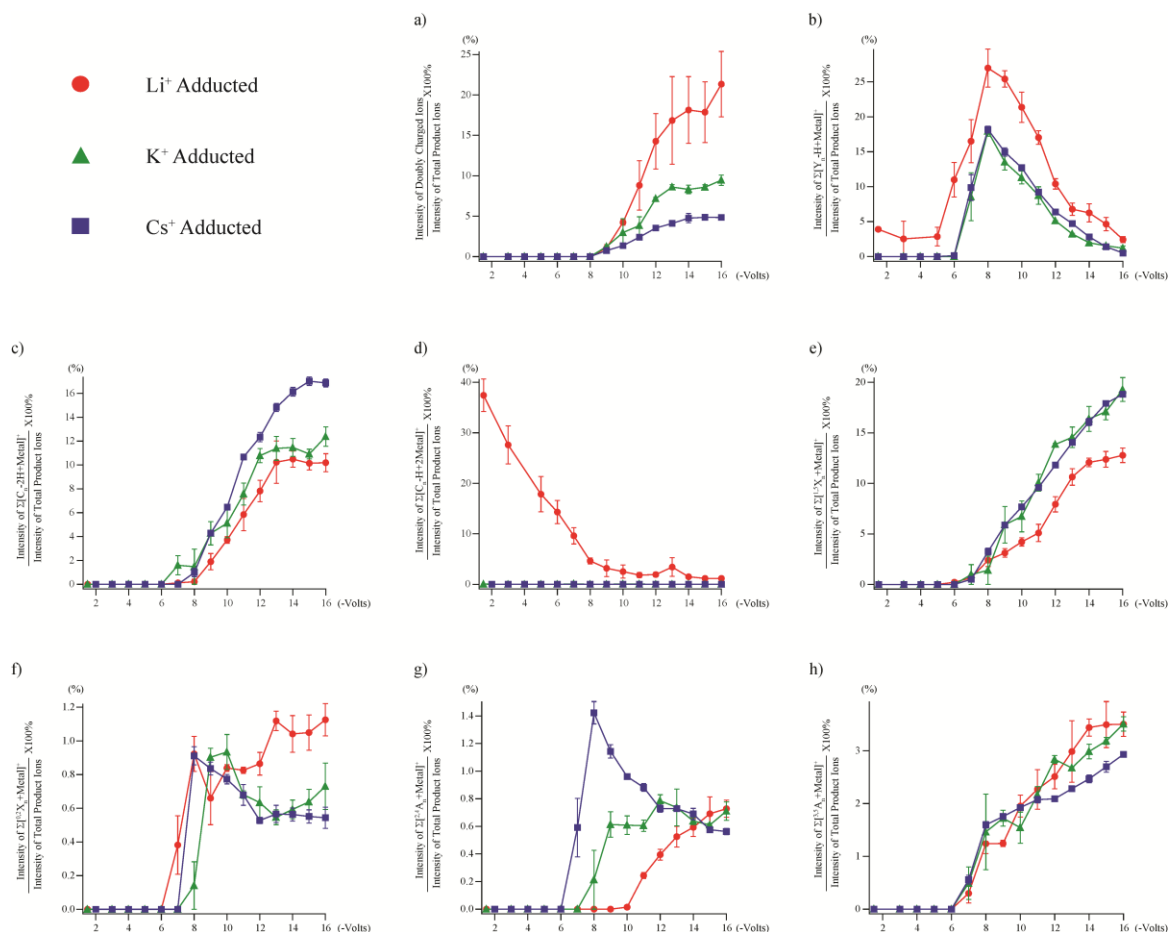


Figure 3.1 The ExD fragmentation pattern of metal-adducted glycans is affected by both the electron energy and the charge carrier. Reduced and permethylated maltoheptaose was selected as the model glycan. Precursor ions adducted with either two Li⁺ (red circle, *m/z* 752.4013), two K⁺ (green triangle, *m/z* 784.3490), or two Cs⁺ (blue square, *m/z* 878.2907) were isolated and irradiated with electrons at different energies, ramping from 1 eV to 16 eV at a 1 eV interval. The x axis represents the voltage applied to the cathode

dispenser. The y axis represents the percentage ratio of the intensity of a specific type of fragment ion and the total product ion intensity. Fragment ions plotted are (a) doubly charged ions, (b) $[Y-H+2Metal]^+$ ions, (c) $[C-2H+Metal]^+$ ions, (d) $[C-H+2Metal]^+$ ions, (e) $[^{1,5}X+Metal]^+$ ions, (f) $[^{0,2}X+Metal]^+$ ions, (g) $[^{2,4}A+Metal]^+$ ions, and (h) $[^{3,5}A+Metal]^+$ ions, respectively. The relative abundance of linkage definitive cross-ring cleavage increased significantly as the electron energy approaches the EED region.

Figure 3.1 The ExD fragmentation pattern of metal-adducted glycans is affected by both the electron energy and the charge carrier. Reduced and permethylated maltoheptaose was selected as the model glycan. Precursor ions adducted with either two Li^+ (red circle, m/z 752.4013), two K^+ (green triangle, m/z 784.3490), or two Cs^+ (blue square, m/z 878.2907) were isolated and irradiated with electrons at different energies, ramping from 1 eV to 16 eV at a 1 eV interval. The x axis represents the voltage applied to the cathode dispenser. The y axis represents the percentage ratio of the intensity of a specific type of fragment ion and the total product ion intensity. Fragment ions plotted are (a) doubly charged ions, (b) $[Y-H+2Metal]^+$ ions, (c) $[C-2H+Metal]^+$ ions, (d) $[C-H+2Metal]^+$ ions, (e) $[^{1,5}X+Metal]^+$ ions, (f) $[^{0,2}X+Metal]^+$ ions, (g) $[^{2,4}A+Metal]^+$ ions, and (h) $[^{3,5}A+Metal]^+$ ions, respectively. The relative abundance of linkage definitive cross-ring cleavage increased significantly as the electron energy approaches the EED region.

Electron-activated dissociation (ExD) methods have recently emerged as promising tools for glycan structural analysis.^{46-47, 50, 103} ExD of metal-adducted glycans can be initiated by either electron transfer from anion radical reagents, as in electron transfer dissociation (ETD) or direct interaction with free electrons. In the latter case, several ExD fragmentation pathways exist; these differ from one another in terms of the electron energy, including: electron capture dissociation (ECD) at low energies, hot-ECD at intermediate energies, and electronic excitation dissociation (EED) at high energies.²⁶ As discussed in Chapter 2, EED takes place at an electron energy of > 9 eV, as evident by the presence of doubly charged fragment ions, which cannot be produced by ECD from doubly charged precursor ions (Figure 3.1). EED is also different from the electron ionization dissociation (EID) process,^{22, 104} because a 9 eV electron is not energetic enough to induce fragmentation after ionization or to induce double ionization. Theoretical investigation presented in Chapter 2 suggested that EED is initiated by electron detachment from an oxygen atom, forming a distonic ion. The subsequent electron re-capture produces a di-radical which can undergo extensive fragmentation. As a charge remote process, EED is capable of producing many more structurally informative fragments than ECD, regardless of the type of metal charge carriers (Figure 3.1).

Whereas a basic understanding of the mechanisms of ExD has been established using model oligosaccharides in Chapter 2, the full potential of this set of powerful techniques remains underexplored. This chapter focuses on the application of different ExD

techniques to the structural characterization of glycans. The potential of EED in high-throughput glycan structural analysis was further investigated.

3.2 Experimental

The experimental procedures for permethylation, reducing end reduction, reducing end ^{18}O -labeling and data analysis are described in Chapter 2.

3.2.1 Materials

Sialyl lewis A (SLe^A), sialyl lewis X (SLe^X), lacto-*N*-tetraose (LNT), and lacto-*N*-neotetraose (LNnT) were purchased from Dextra Laboratories (Reading, UK). Maltoheptaose, dextran ladder, ribonuclease B (RNase B), H₂¹⁸O (97%) water, 2-aminopyridine, acetic acid, and reagents for permethylation including dimethyl sulfoxide (DMSO), sodium hydroxide (NaOH), methyl iodide (CH₃I), and chloroform, as well as all salts including lithium acetate, sodium acetate, sodium borohydride (NaBH₄), potassium acetate, cesium acetate were obtained from Sigma-Aldrich (St. Louis, MO). Glycerol-free PNGase F was obtained from Prozyme (Hayward, CA). Sep-PakTM C18 SPE cartridges were obtained from Waters (Milford, MA). Porous-graphitized carbon (PGC) solid phase extraction (SPE) columns were obtained from Thermo-Scientific (Springfield, NJ). Reverse-phase C18 ZipTip was obtained from Millipore (Billerica, MA). Microspin cellulose cartridges were purchased from Harvard Apparatus (Holliston, MA).

3.2.2 Reducing End 2-AB Labeling

The reducing end 2-AB labeling was performed as described previously.¹⁰⁵ Briefly, the labeling reagent solution was prepared by dissolving 6 mg of dried 2-aminobenzamide (2-AB) and 6 mg of dried sodium cyanoborohydride (NaBH₃CN) in 100 μL of acetic acid:DMSO (3:7, v:v) solution. 10 μg of the oligosaccharide sample was dissolved in 10 μL of the reagent solution and was incubated at 65 °C for 3 hours. The excessive reagents were then removed by microspin cellulose cartridges (Harvard Apparatus, Holliston, MA).

3.2.3 N-linked Glycan Release from Ribonuclease B

The high-mannose *N*-linked glycans were released from RNase B by PNGase F according to the Glyko® *N*-Glycanase protocol by Prozyme. Dried glycoprotein (500 μg) was dissolved in 45 μL of 1X Tris reaction buffer and 2.5 μL of denaturation solution. The glycoprotein was then denatured in boiling water for 5 min. After denaturation, 2.5 μL of detergent solution and 2 μL of PNGase F were added. The glycoprotein and PNGase F mixture was incubated at 37 °C overnight. Sep-Pak™ C18 SPE cartridges were used to separate the released *N*-linked glycans from the protein. The C18 SPE cartridge was sequentially rinsed with 10 mL of 100% ACN, 50% ACN, and water. The high mannose *N*-linked glycan, deglycosylated ribonuclease B and PNGase F mixture was then loaded to the cartridge. The *N*-linked glycans were eluted from the cartridge by 2 mL water for three times. The purified *N*-linked glycans were then dried in a SpeedVac™ concentrator.

3.2.4 Electrospray Conditions

Permethylated oligosaccharides were dissolved in 25% methanol, 20-250 μM salt solutions to a concentration of 5 μM for electrospray ionization (ESI) tandem MS analysis. Samples were loaded into a glass capillary tip pulled with a micropipette puller (model P-97; Sutter Instruments Co., Novato, CA) to ~ 1 μm orifice diameter. A bare nickel chromium wire was inserted into the sample solution on the distal end of the tip to form the electrical connection. Samples were then directly infused into the mass spectrometer ion source.

3.2.5 Tandem Mass Spectrometry

The tandem mass spectrometry (MS/MS) experiments were performed on a 12-T solariXTM hybrid Qq-FTICR mass spectrometer equipped with an indirectly heated hollow dispenser cathode (Bruker Daltonics, Bremen, Germany). Target ions were isolated by a front-end quadrupole and accumulated in the collision cell for 100 to 500 ms before being transferred to the ICR cell. For low-energy ECD, the precursor ions were irradiated with ~ 1.5 eV electrons for 100 ms; for EED, the precursor ions were irradiated with 14 eV or 16 eV electrons, for up to 0.5 s. The cathode heating current was from 1.32 A to 1.52 A. A 0.5 s transient was typically acquired. Each ExD spectrum shown is the result of 100 to 200 transients summed to improve the signal-to-noise ratio, except for the spectrum in Figure 3.22, which is 1 transient.

3.3 Results and discussion

3.3.1 Linkage Determination of the High Mannose *N*-linked Glycan by ExD

The ExD techniques were applied to the structural analysis of an *N*-linked glycan released from Ribonuclease B, Man₅GlcNAc₂ (Man: mannose, GlcNAc: *N*-acetyl glucosamine). Li⁺ was selected as the charge carrier, because the earlier results indicated that it is able to initiate fragmentations at all electron energies, and Li-induced cleavages reached both the reducing and non-reducing ends in the maltoheptaose study. Doubly lithiated Man₅GlcNAc₂ was isolated and fragmented by ExD at three electron energies, 1.5 eV (Figure 3.2), 9.0 eV (Figure 3.3), and 14.0 eV (Figure 3.4). The same precursor ion was also subjected to CID for comparison (Figure 3.5). Note that, this branched *N*-linked glycan produced quite a few fragment ions for which more than one assignment is possible. For example, the Y_{4α}['], Y_{4α}^{''} and Y_{3β} ions all have the same calculated mass, as do the ^{1,5}X_{4α}['], ^{1,5}X_{4α}^{''} and ^{1,5}X_{3β} ions. Figures 3.2 to 3.5 include all possibilities, although some of the labeled cleavages may not have actually occurred. The assignments could be fully clarified with higher stages of MSⁿ but, since these monosaccharide losses do not inform about branching and thus do not contribute significantly to the structural determination, such analyses were not performed in this study.

As expected, CID (28 eV) generated mostly glycosidic bond cleavages, producing complete B- and Y-ion series, as well as abundant cross-ring products in the ^{1,5}A and ^{1,5}X series (Figure 3.5). A few informative cross-ring fragments were also observed, which

identified the two 1→6 linkages based on the presence of the $^{0,4}A_{2\alpha}$ and $^{0,4}A_3$ fragments. The linkage positions for the other four glycosidic bonds could not be determined unambiguously by CID.

The low-energy ECD (1.5 eV) cleavage map and spectrum are shown in Figure 3.2. The four dominant fragments resulted from glycosidic cleavages around the chitobiose core, indicating that the preferred electron capture site was the GlcNAc-bound Li^+ near the reducing end. The presence of B_3 and C_3 ions suggested that the other Li^+ was probably distant, coordinated by mannose residues on the 6-branch to minimize the Coulombic repulsion between the two charge carriers. Several Y- and Z-type ions resulting from cleavages near the non-reducing end were also observed, indicating that the non-reducing end Li^+ could also initiate ECD pathways, albeit with lower probabilities. Although low-energy ECD produced several informative cross-ring cleavages that were not observed in CID, they mostly occurred around the GlcNAc residues, and no evidence indicated that cross-ring products formed *via* cleavages in the antennae regions. Among the six glycosidic linkages, only the 1→6 linkage at the first branch point could be defined. The absence of cross-ring cleavages near the termini of the antennae was likely the consequence of competitive electron capture near the chitobiose core, together with competition from glycosidic cleavages, even when the Li^+ located on an antenna did capture an electron.

As suggested by the maltoheptaose ExD study presented in Chapter 2, increasing the electron energy should help to access the thermodynamically and/or kinetically unfavored fragmentation channels of the released and permethylated high mannose *N*-linked glycan.

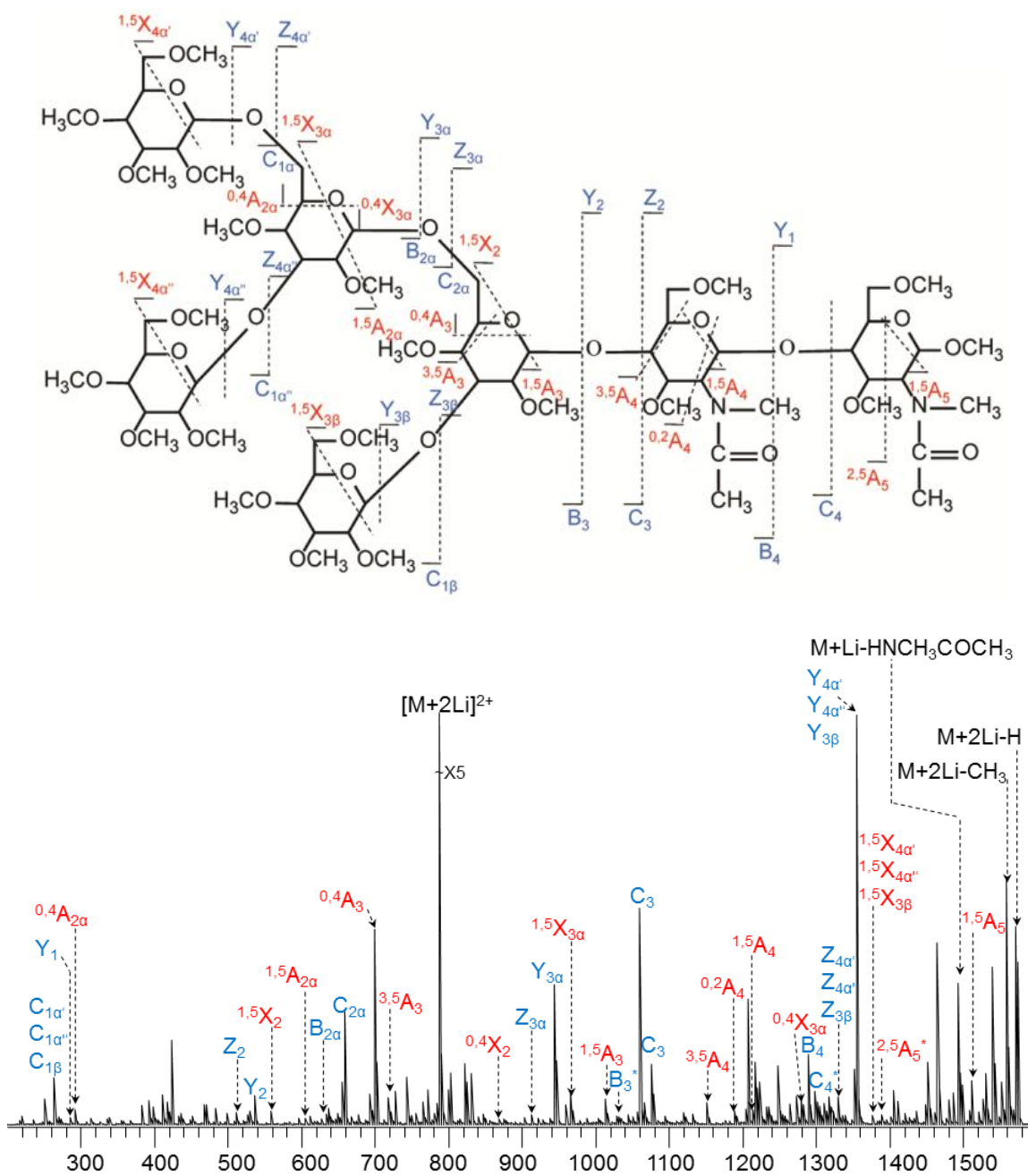


Figure 3.3 Hot-ECD (9.0-eV electrons) cleavage map (top) and spectrum (bottom) of permethylated $\text{Man}_5\text{GlcNAc}_2$ $[\text{M} + 2\text{Li}]^{2+}$ m/z 785.4121.

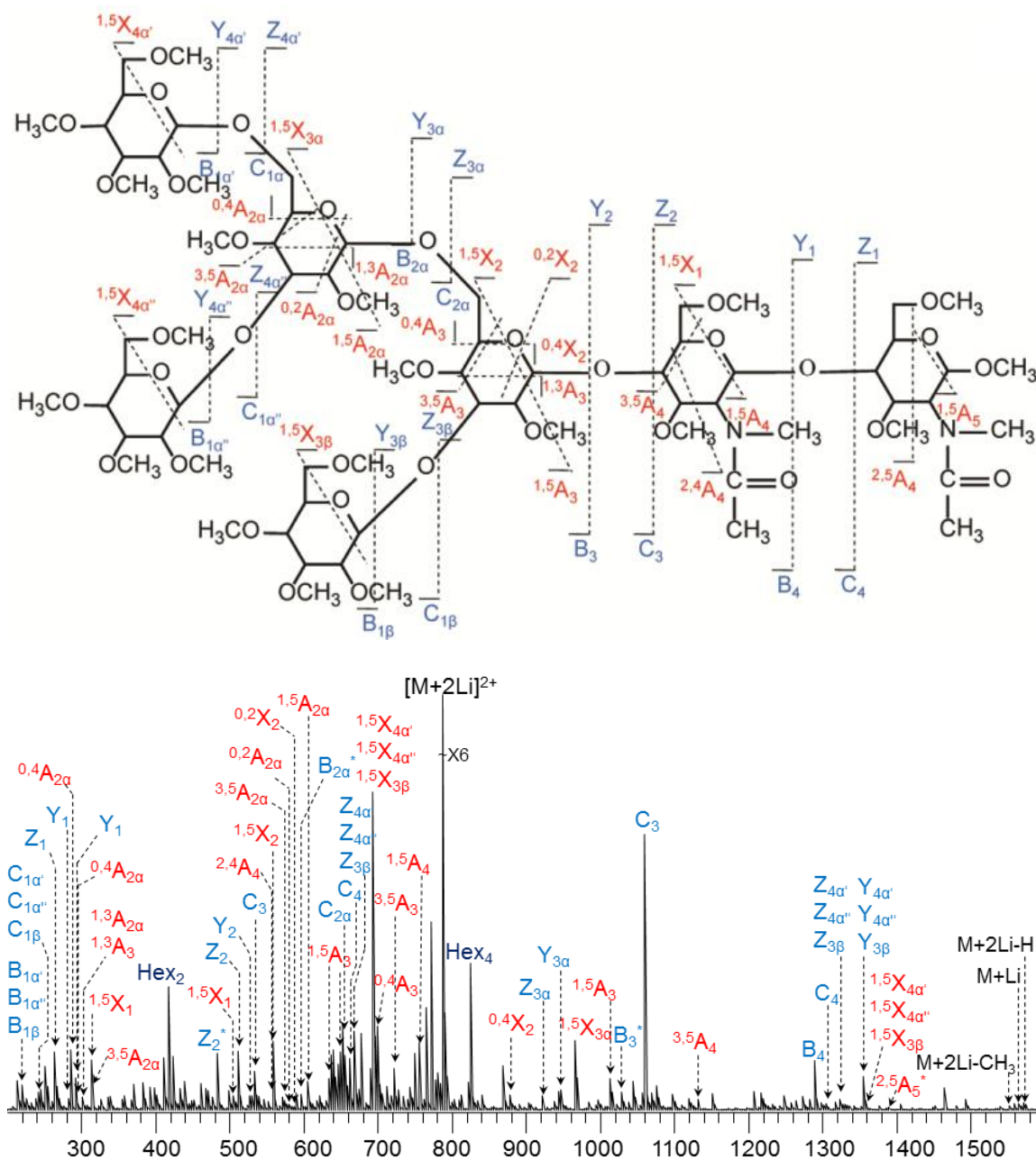


Figure 3.4 EED (14.0-eV electrons) cleavage map (top) and spectrum (bottom) of permethylated Man₅GlcNAc₂ [M + 2Li]²⁺ *m/z* 785.4121.

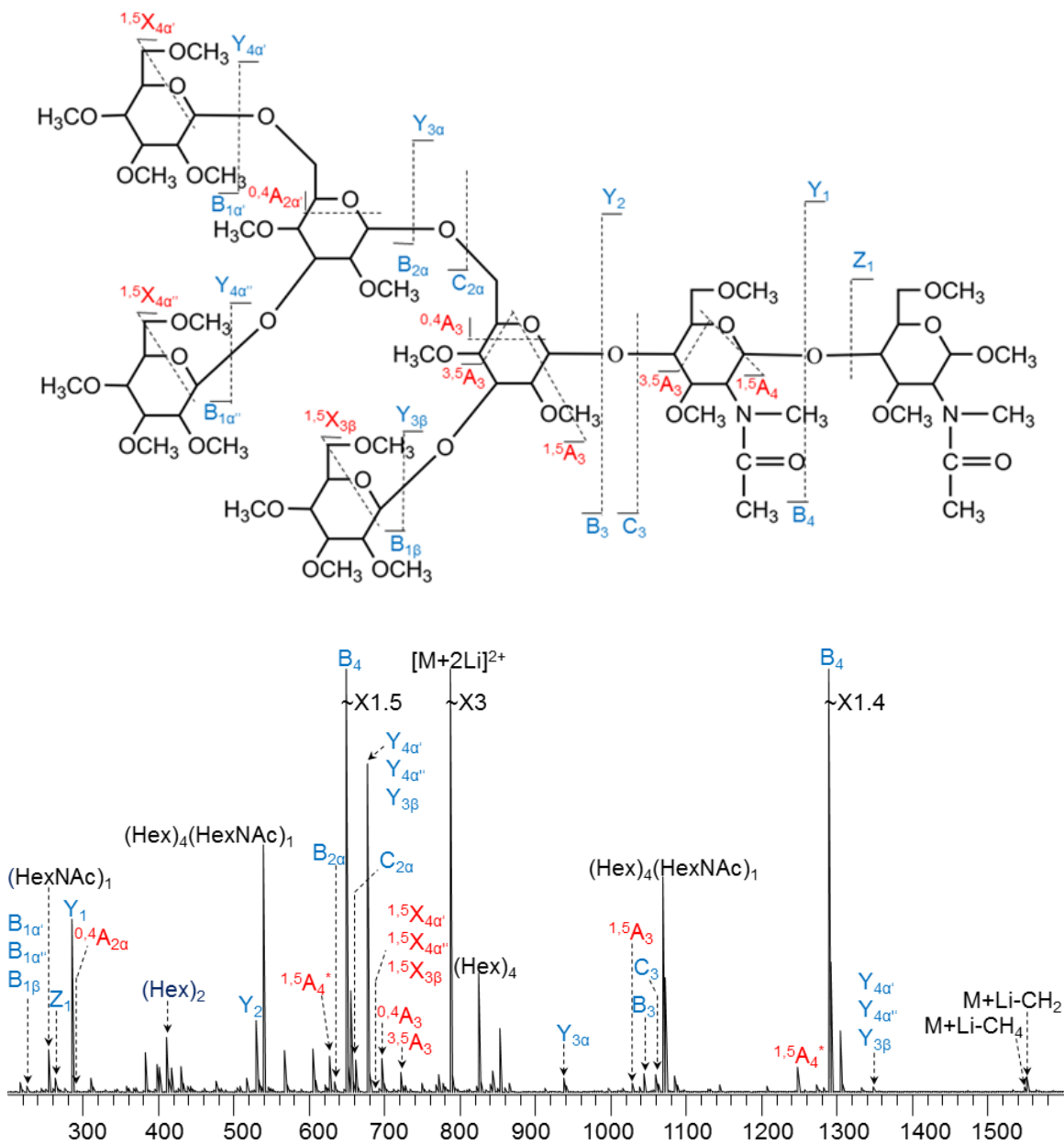


Figure 3.5 CID (CE 28 eV) cleavage map (top) and spectrum (bottom) of permethylated $Man_5GlcNAc_2 [M + 2Li]^{2+} m/z$ 785.4121.

Figures 3.3 and 3.4 show the hot-ECD (9 eV) and EED (14 eV) cleavage maps and spectra of the doubly lithiated $\text{Man}_5\text{GlcNAc}_2$, respectively. Hot-ECD was able to produce cross-ring cleavages reaching the second branching point, identifying the second 1→6 linkage *via* the presence of the $^{0,4}\text{A}_{2\alpha}$ and $^{0,4}\text{X}_{3\alpha}$ ions. At 14 eV, additional, new cross-ring fragments were generated, including the $^{1,3}\text{A}_{2\alpha}$ and $^{0,2}\text{A}_{2\alpha}$, as well as the $^{1,3}\text{A}_3$ and $^{0,2}\text{X}_2$ ions, which were essential for the delineation of the 1→3 linkages at both branch points. Altogether, five out of the six glycosidic linkage positions could be identified by EED, including all linkages in the antennae regions, and thus EED provided much more complete information than either CID or low-energy ECD.

3.3.2 Optimization of the EED Experimental Parameters

The practical use of EED has been limited by its low fragmentation efficiency.²² Figure 3.6a shows a generic setup for ExD experiments. The large negative cathode bias used in EED allows a much higher number of electrons, including those in the low-energy tail of the electron energy distribution, to enter the ion cyclotron resonance (ICR) cell. It is thus important to control the electron population in the cell to minimize competition from the more efficient ECD process. Consequently, previous EED studies were usually carried out with a low cathode heater current (1.3 A).²⁸ As this current was increased, the fragmentation process switched from EED to ECD, generating predominantly the charge reduced species (Figure 3.6b, 3.7a, b). However, use of a lower heater current necessitates prolonged electron irradiation time (> 1 s) for efficient EED. Alternatively,

the influx of low-energy electrons can be limited by setting the extraction potential to a value slightly less negative than the cathode bias, allowing only the high-energy electrons to enter the ICR cell (Figure 3.6c), as was previously implemented in electron detachment dissociation (EDD) studies. Under the optimized conditions, 200 to 500 ms irradiation time was sufficient for efficient EED (Figure 3.7c).

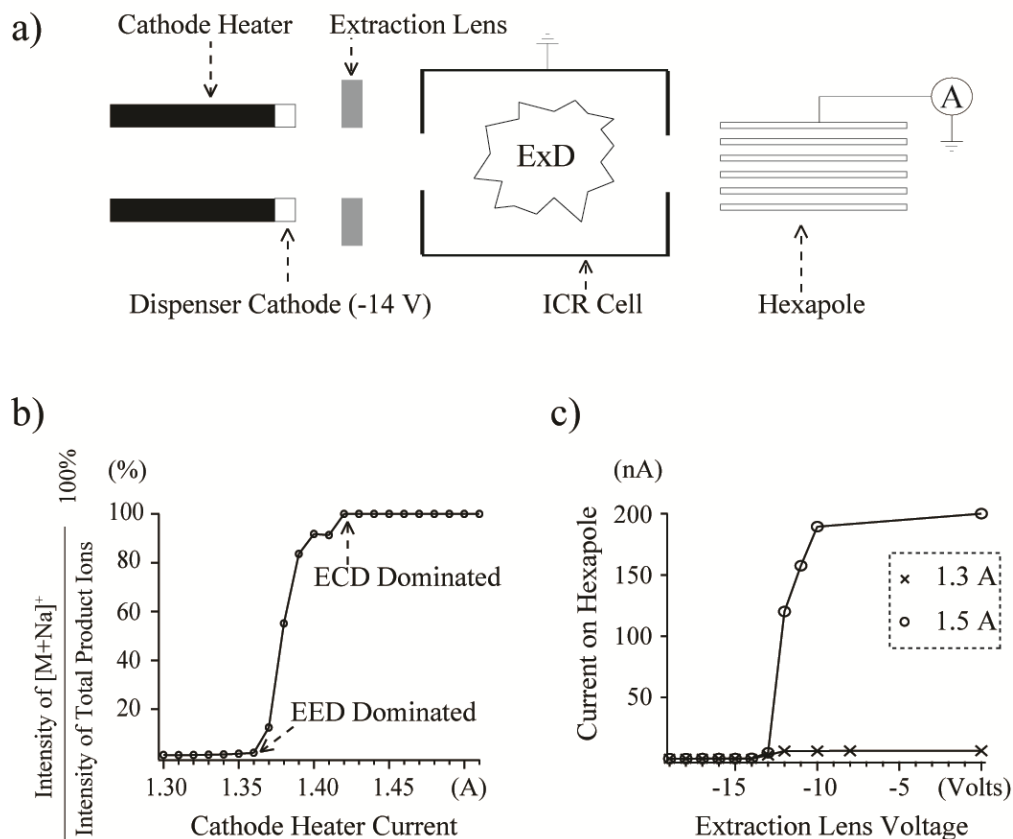


Figure 3.6 a) Schematics of the ExD experimental setup. b) Plot of the relative abundance of the charge reduced species as a function of the cathode heating current, with the cathode bias set at -14 V and the extraction potential at 15 V. c) Plot of the electron current measured at the hexapole as a function of the extraction potential, with the cathode bias set at -14 V, and the cathode heating current set at either 1.3 A (×) or 1.5A (○).

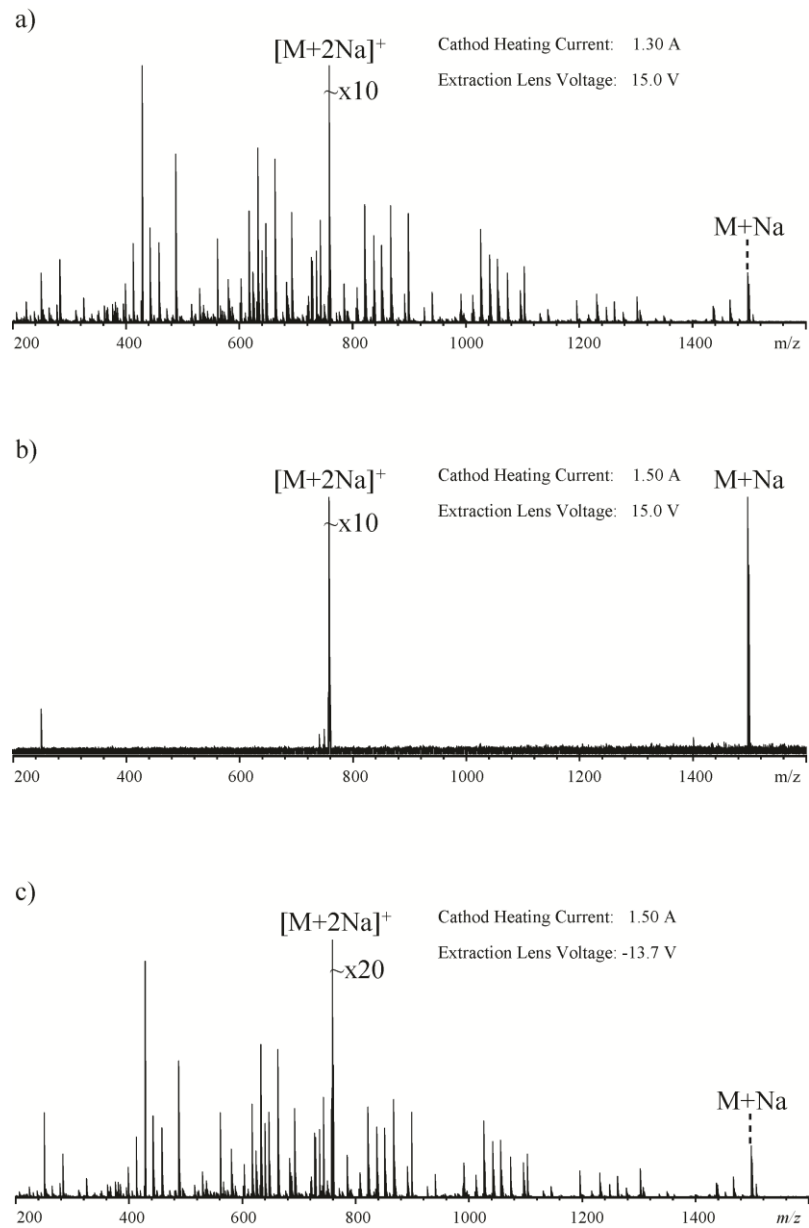


Figure 3.7 Influence of the cathode heating current and extraction lens voltage on the fragmentation pattern of the doubly sodiated permethylated maltoheptaose (m/z 760.3594). With a positive extraction potential of 15 V, allowing all electrons to enter the ICR cell, a) EED dominated at low cathode heating current (1.3 A), and b) ECD dominated at high cathode heating current (1.5 A). c) With the extraction potential set to -

13.7 V, preventing low-energy electrons from entering the cell, EED fragmentation was recovered at high cathode heating current (1.5 A).

3.3.3 Application of EED to Glycan Linkage Isomer Differentiation

The previous examples demonstrated the utility of EED in the structural characterization of simple linear and branched glycan standards. Here, with improved efficiency, the performance of EED was further evaluated on glycans having more complex structures. Two tumor antigens, Sialyl Lewis A (SLe^A) and Sialyl Lewis X (SLe^X), were selected as models, not only because they play important roles in cell-cell recognition, but also because they are linkage isomers containing analytically challenging residues: sialic acid (*N*-acetyl neuraminic acid, Neu5Ac) and fucose (Fuc).⁷² Permethylation was performed to stabilize these labile groups and to block unpredictable fragmentation pathways such as Fuc migration. Permethylation also facilitates *de novo* topology analysis as each glycosidic cleavage leaves a free hydroxyl “scar”, enabling differentiation of terminal and internal fragment ions and assignment of the initial branch point. However, ambiguities arising from the potential for isomeric non-reducing end and reducing end fragments still exist for permethylated glycans. Although isomer-based ambiguity is more common for glycans with symmetrical structures, it can also occur in highly asymmetrical glycans. For example, for permethylated SLe^X, the ^{0,2}A_{2α} and ^{2,5}X_{1α} fragments both have a neutral mass of 523.263 u. Such ambiguity can be removed by labeling the reducing end hemiacetal oxygen with ¹⁸O prior to permethylation.

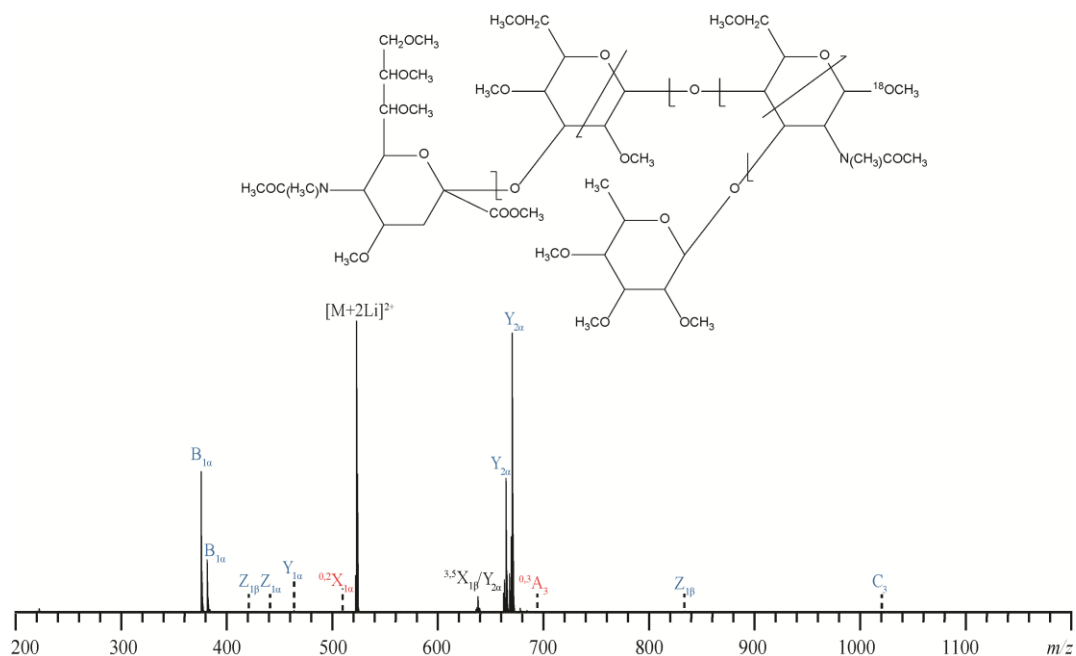


Figure 3.8 The CID cleavage map and the CID spectrum of the doubly lithiated, permethylated and ^{18}O labeled SLe^{X} precursor ion at m/z 523.2830.

Figures 3.8, 3.9, and 3.10 show the CID, ECD, and EED spectra and cleavage maps of the doubly lithiated, ^{18}O -labeled and permethylated SLe^{X} , obtained on a 12-T hybrid Fourier-transform (FT) ICR mass spectrometer. As an ergodic fragmentation method, CID produced mostly glycosidic cleavages with the most abundant product ions resulting from the facile sialic acid loss (Figure 3.8). A few more cross-ring cleavages were observed in ECD (Figure 3.9), but none occurred within the reducing end *N*-acetyl glucosaminyl (GlcNAc) residue, preventing differentiation of SLe^{A} and SLe^{X} . Sialic acid loss was still the predominant pathway, presumably because the ECD process was initiated by electron capture by the metal charge carrier, and the sialic acid residue was the preferred metal binding site. By contrast, EED produced extensive glycosidic and

cross-ring cleavages throughout the molecule (Figure 3.10). Similar ExD fragmentation patterns were observed for SLe^A (Figures 3.11 and 3.12).

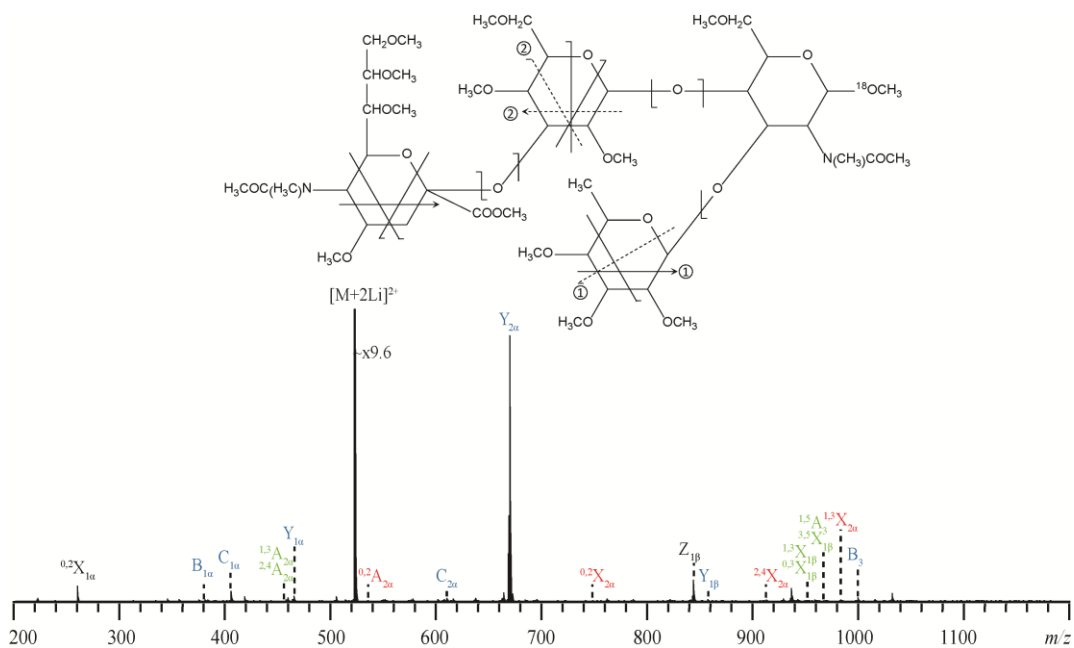


Figure 3.9 The ECD cleavage map and the ECD spectrum of the doubly lithiated, permethylated and ¹⁸O labeled SLe^X precursor ion at *m/z* 523.2830.

Figure 3.10 inset shows a zoomed-in view of the region containing the ^{2,5}A_{2α} and ^{0,2}X_{1α} ions in the EED spectrum of SLe^X, with (bottom) and without (top) the reducing-end ¹⁸O-labeling. Both ^{2,5}A_{2α} and ^{0,2}X_{1α} ions (*m/z* 514.2834 for the unlabeled SLe^X) are keys to determination of the 2→3, sialic acid–galactose (Gal) linkage, but they are isomeric and cannot be assigned definitively in the spectrum of the unlabeled glycan. When this spectrum is compared to the spectrum of the ¹⁸O-labeled glycan, the ^{0,2}X_{1α} ion is offset by

~2 Da whereas the $^{2,5}A_{2\alpha}$ ion is unaffected, and this confirms their assignments, allowing confident linkage determination.

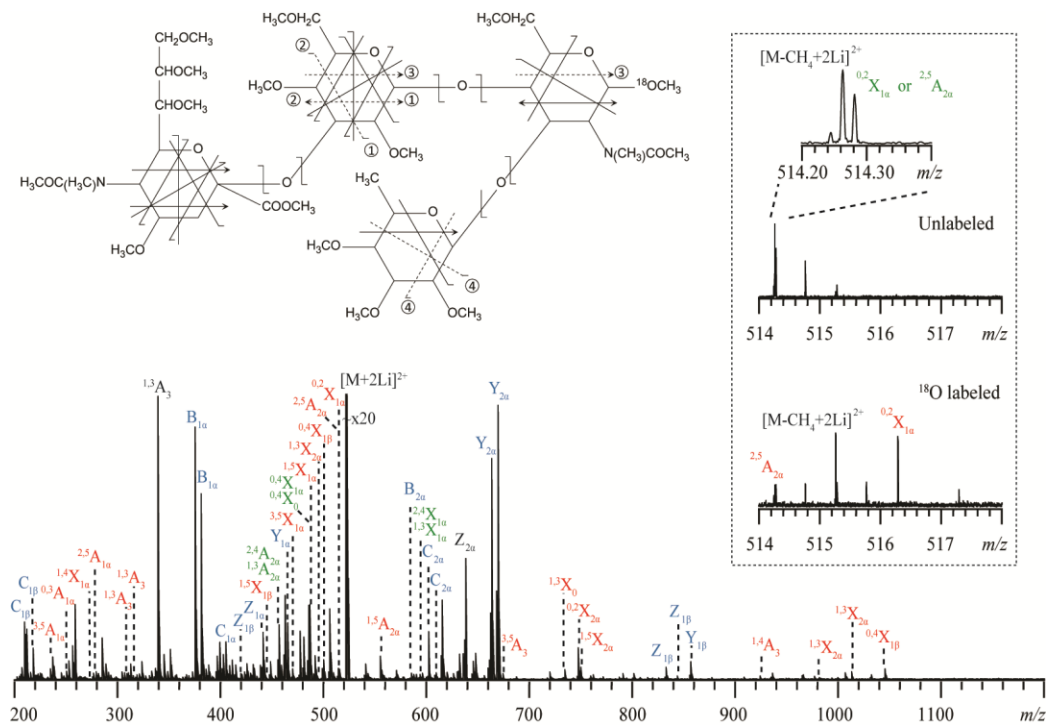


Figure 3.10 The EED cleavage map and spectrum of the doubly lithiated, permethylated and ^{18}O -labeled SLe^X precursor ion at m/z 523.2830.

The number of building blocks with unique masses is smaller for glycans than for peptides, and each monosaccharide residue can potentially be cleaved into 22 different glycosidic and cross-ring fragments. Consequently, the presence of isobaric fragment ions is quite common in complex glycan EED spectra. A 36-mDa peak splitting due to the mass difference between a CH_4 group and an O atom is frequently observed; their

definition requires a mass resolving power of $> 50,000$ at $m/z \sim 1,000$ for baseline separation. Peak splitting with a smaller interval can also occur. For example, in the EED spectrum of permethylated SLe^X , the $^{0,2}X_{1\alpha}$ and $^{2,5}A_{2\alpha}$ ions (both at m/z 514.2834) and the doubly charged $[M-CH_4+2Li]^{2+}$ ion (m/z 514.2658) are separated by only 18 mDa (Figure 3.10 inset). The superior mass resolving power afforded by a high-field FTICR mass analyzer is essential for confident peak assignments, and for delineation of the Neu5Ac2 \rightarrow 3Gal linkage in SLe^X .

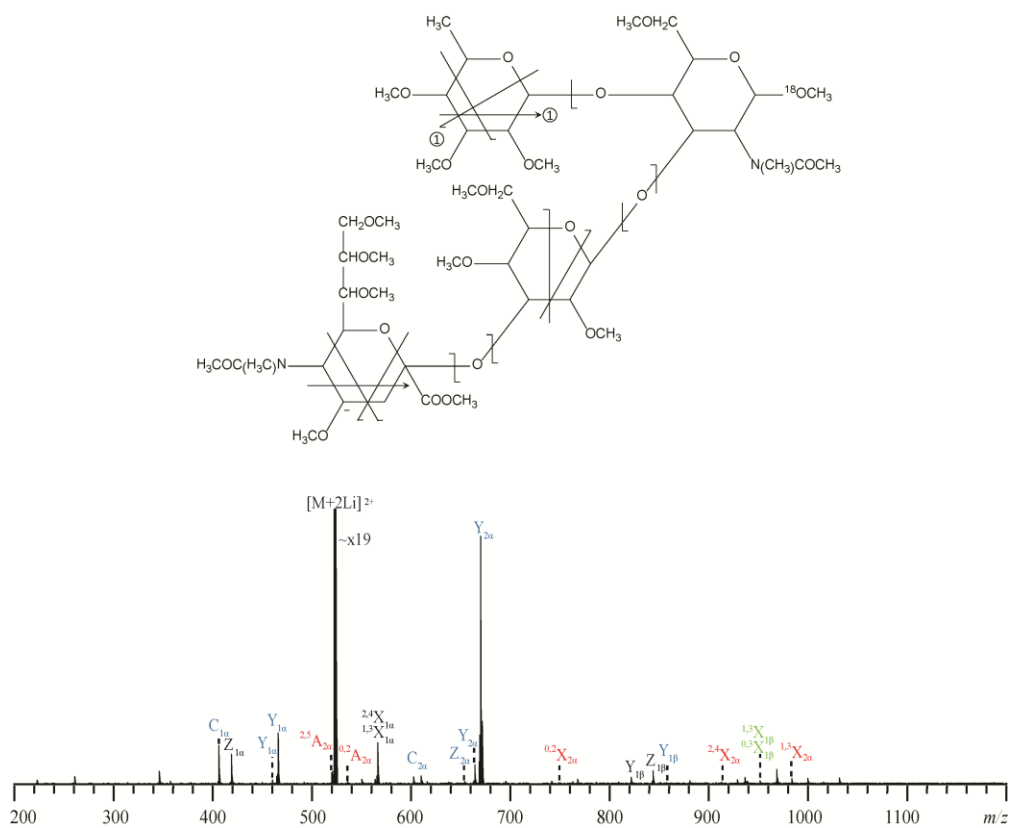


Figure 3.11 The ECD cleavage map and the ECD spectrum of the doubly lithiated, permethylated and ^{18}O labeled SLe^A precursor ion at m/z 523.2830.

ExD experiments were also carried out on milk oligosaccharide linkage isomers, lacto-*N*-tetraose (LNT) and lacto-*N*-neotetraose (LNnT). Again, EED produced the most extensive fragmentation, including cross-ring cleavages for unambiguous determination of the nonreducing end Gal–GlcNAc linkage for isomer differentiation (Figures 3.13 and 3.14).

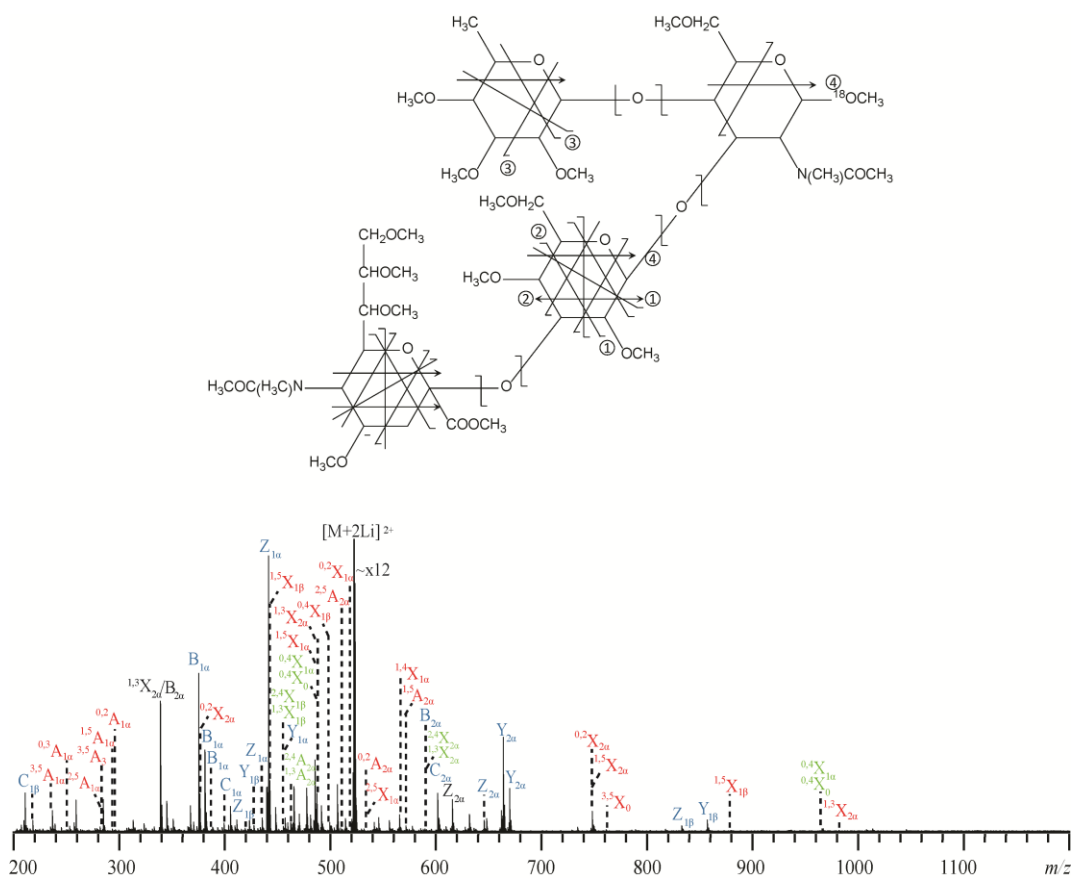


Figure 3.12 The EED cleavage map and the EED spectrum of the doubly lithiated, permethylated and ^{18}O labeled SLe^{A} precursor ion at m/z 523.2830.

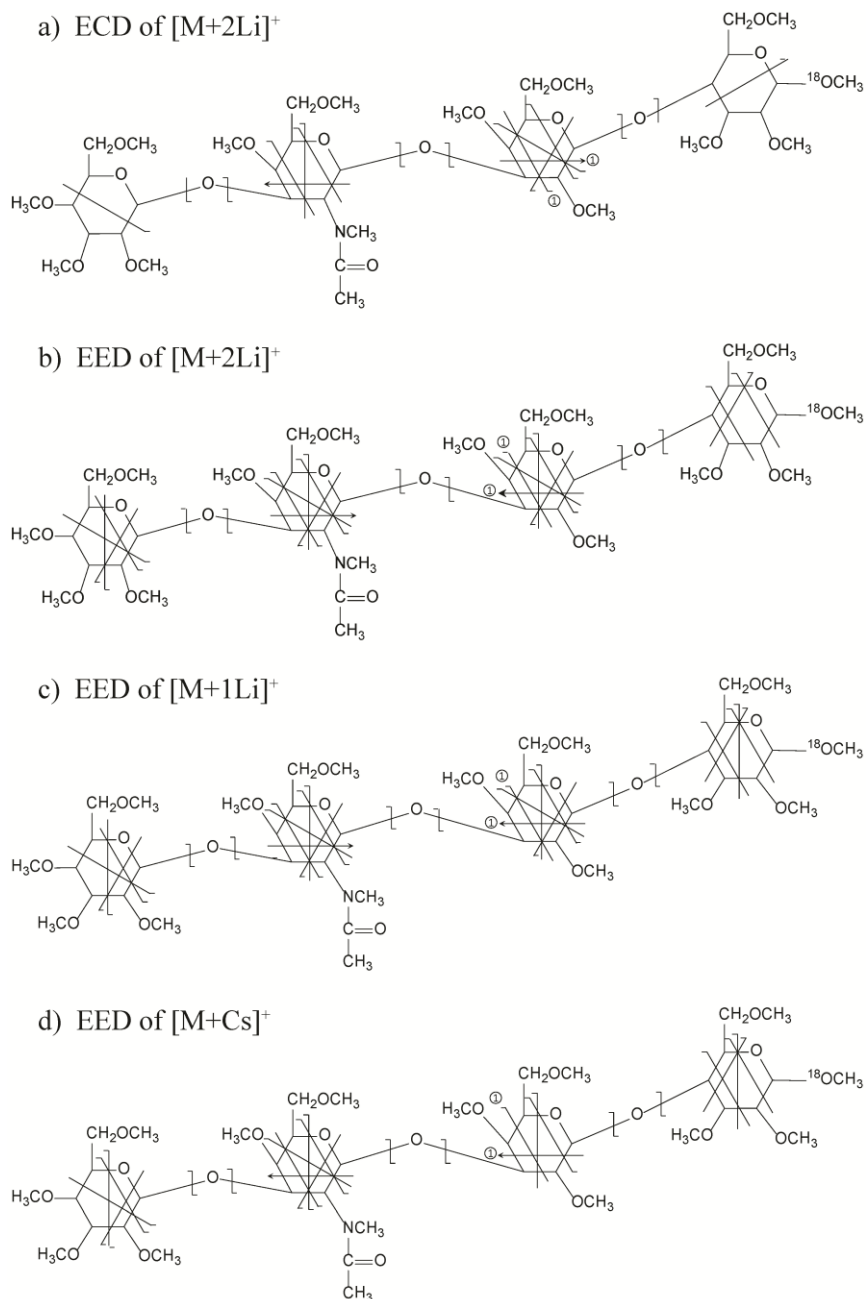


Figure 3.13 a) The ECD and b) EED cleavage maps of the doubly lithiated, permethylated, ^{18}O -labeled LNT at m/z 459.7513; c) the EED cleavage map of the singly lithiated, permethylated, ^{18}O -labeled LNT at m/z 912.4872; d) the EED cleavage map of the singly cesiated, permethylated, ^{18}O -labeled LNT at m/z 1038.3767.

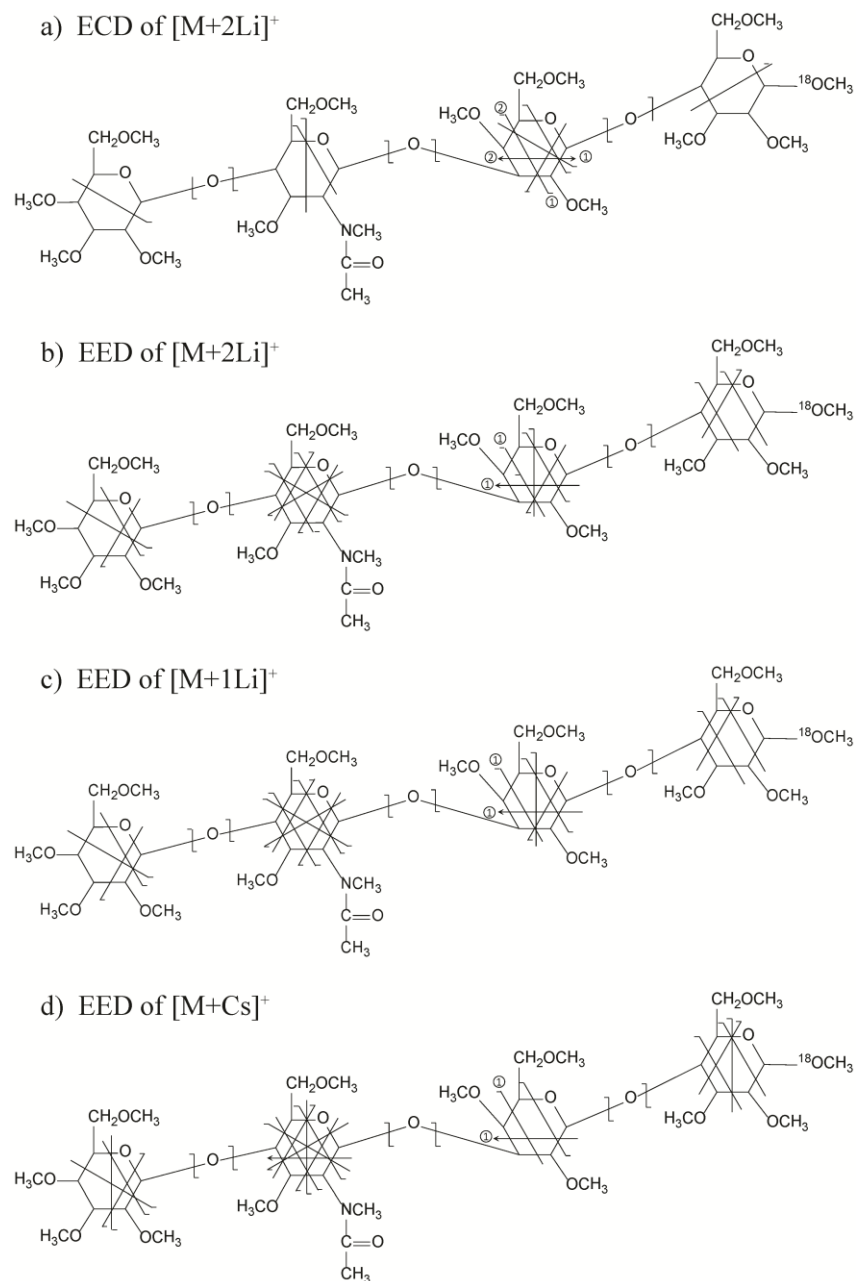


Figure 3.14 a) The ECD and b) EED cleavage maps of the doubly lithiated, permethylated, ^{18}O -labeled LNT at m/z 459.7513; c) EED cleavage map of singly lithiated, permethylated, ^{18}O -labeled LNT at m/z 912.4872; d) EED cleavage map of singly cesiated, permethylated, ^{18}O -labeled LNT at m/z 1038.3767.

In addition to providing more structural information in general, EED offers another advantage over ECD and ETD in that it does not involve charge reduction. Thus, EED is applicable to singly charged ions, making it an ideal choice for analysis of MALDI-generated ions as well as small glycans that cannot be efficiently multiply charged.

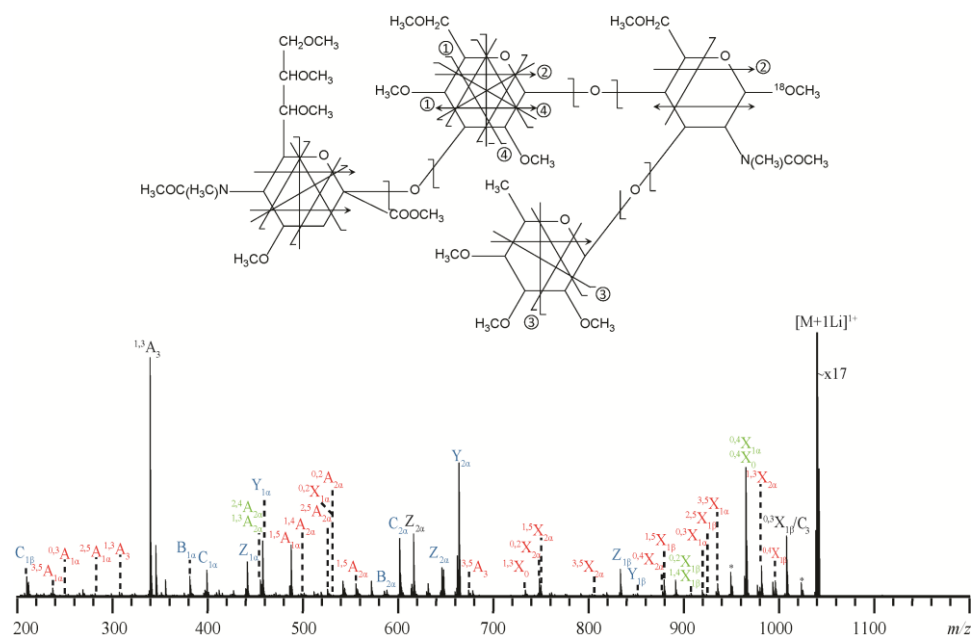


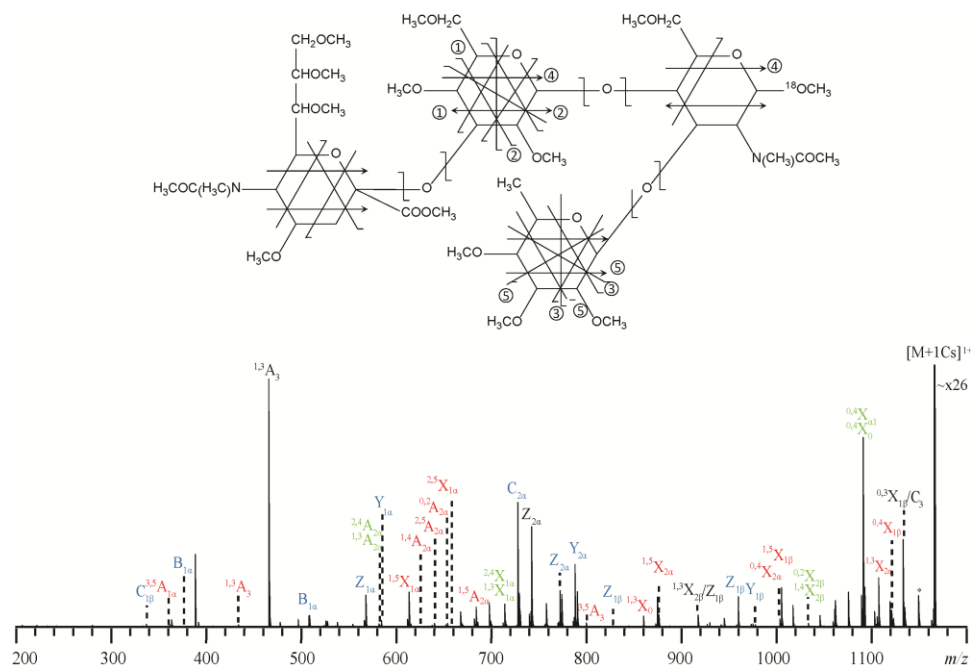
Figure 3.15 The EED cleavage map and spectrum of the singly lithiated, permethylated and ^{18}O labeled SLe^{X} precursor ion at m/z 1039.5505.

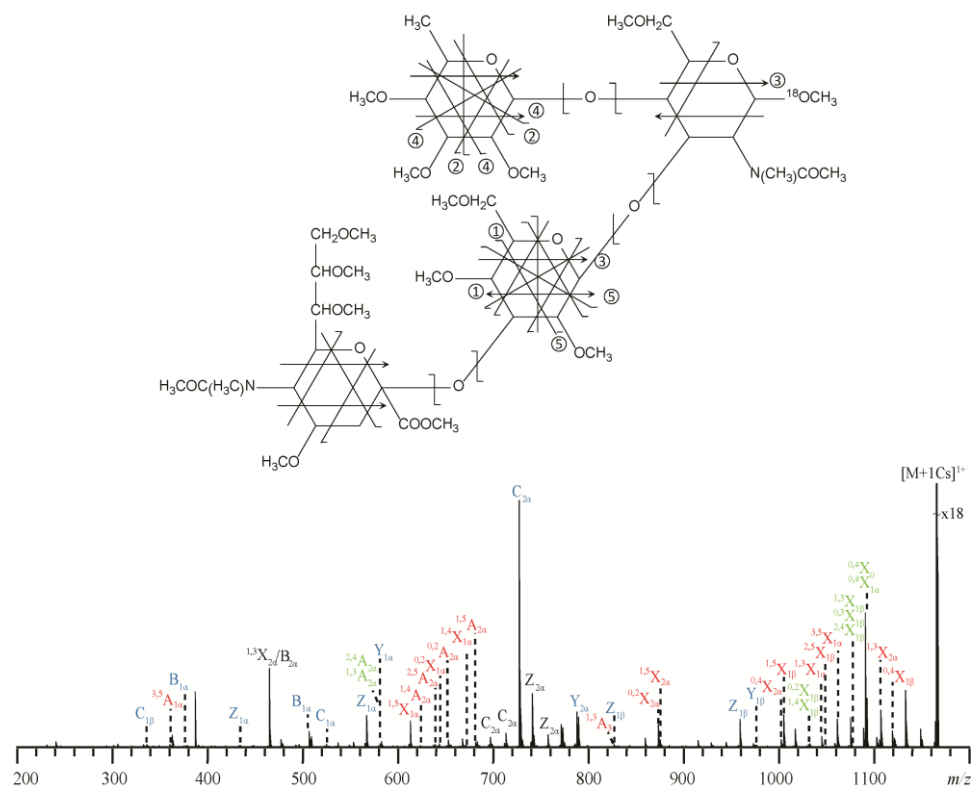
As shown in Figures 3.15 and 3.16, EED of the singly lithiated $\text{SLe}^{\text{X}}/\text{SLe}^{\text{A}}$ produced fragmentation coverage similar to their doubly lithiated counterparts (Figures 3.10 and 3.12). Charge retention benefits the analysis of multiply charged precursor ions as well. First, fragment ions in a higher charge state can be more efficiently detected because the image current generated by an ion scales linearly with its charge. Second, because the

mass resolving power of the ICR analyzer is inversely proportional to the ion mass-to-charge ratio, it is easier to resolve isobaric fragment ions when they are present in higher charge states and thus their signals appear at lower m/z values. Finally, charge retention increases the chance of observing both members of each set of complementary fragment ions, leading to more confident spectral interpretation. Figures 3.17 and 3.18 show the EED spectra of the singly and doubly lithiated, permethylated $\text{Man}_5\text{GlcNAc}_2$ (Man = mannose). Whereas the $^{0,4}\text{X}_{3\alpha}$ ion that defines the terminal, $\text{Man}1\rightarrow6\text{Man}$ linkage was present in both spectra, its complementary $^{0,4}\text{A}_{2\alpha}$ ion was only observed in the EED spectrum of the doubly lithiated species. A general lack of non-reducing end fragments in EED of the singly lithiated species likely resulted from the preference of Li^+ -binding near the reducing end chitobiose core.

cations, such as Na^+ and Cs^+ , are monoisotopic, but they do not induce efficient ECD fragmentation, producing mostly metal loss, as a result of their weaker interaction with glycans and lower recombination energy upon electron capture. EED does not suffer from such restriction, as it is a charge remote process with a much higher energy input. EED of the $[\text{M} + \text{Cs}]^+$ ions from SLe^{X} and SLe^{A} (Figures 3.19 and 3.20) provided comparable structural information as that of their $[\text{M} + \text{Li}]^+$ species. Cesium adduction offers an additional benefit owing to its large negative mass defect ($m_{\text{Cs}} = 132.9055$ Da). For permethylated polyhexose with a repeating unit of $\text{C}_9\text{H}_{16}\text{O}_5$ (204.0998 Da), substitution of each proton with a Cs^+ introduces an effective mass defect shift of around -0.16 Da at a given nominal mass. This mass difference is significantly higher than the variation in mass defects due to the difference in the fragment elemental composition. As illustrated in Figure 3.21, EED fragment ions of the $[\text{M} + 2\text{Cs}]^{2+}$ of SLe^{X} were clustered around three trend lines in the mass defect vs. mass plot, corresponding to 0, 1, or 2 Cs^+ -adduction, respectively. This can be utilized for automatic metal counting and accurate determination of the fragment ion neutral mass.

glycans released from a glycoprotein, the actual sample consumption was lower and the acquisition time could be reduced further with off-line or on-line LC isolation. Nonetheless, it appears that EED has the sensitivity and throughput compatible with on-line LC separation. Further, in LC analysis of glycans, reducing-end chromophore labeling is frequently used, because it improves separation and facilitates UV detection and quantification. However, the chromophore-labeled reducing end is often the preferred metal binding site, as well as an electron scavenger. Consequently, reducing-end labeled glycans fragment poorly in ECD, and produce mostly small tag loss, as illustrated in Figure 3.23a. EED, on the other hand, is not affected by the presence of the chromophore (Figure 3.23b), and is well suited for LC-MS analysis of reducing-end labeled glycans.





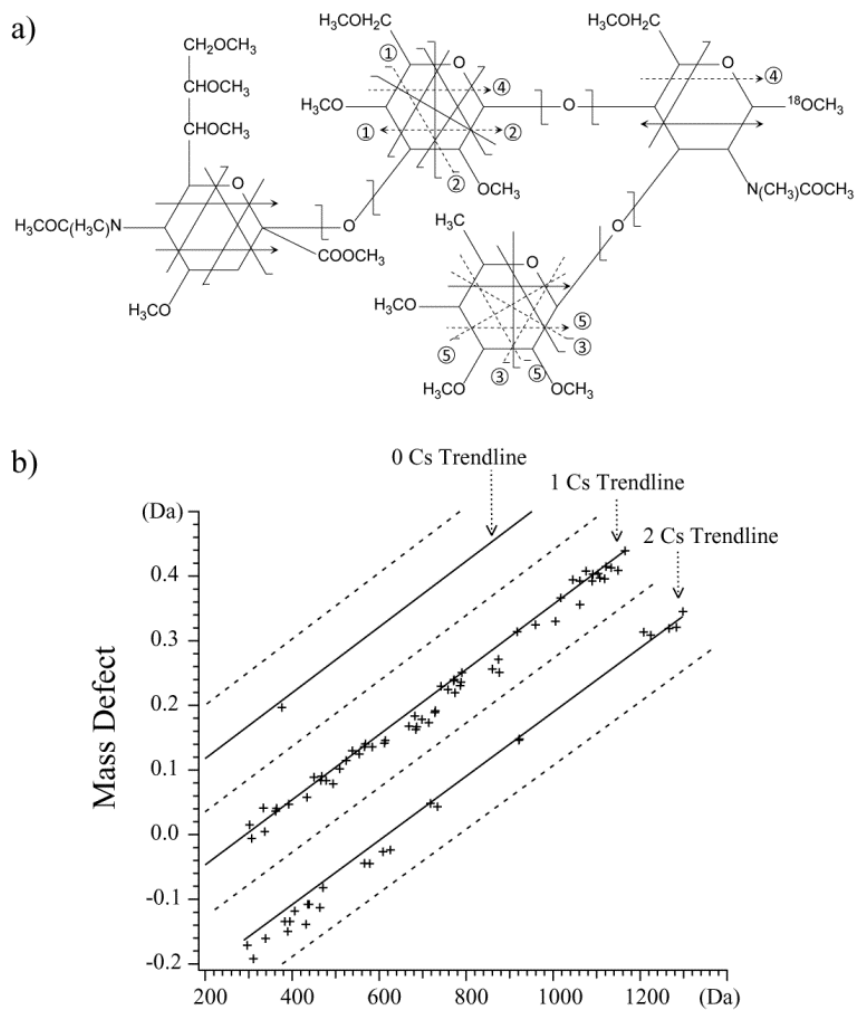


Figure 3.21 a) The EED cleavage map of the $SLe^X [M + Cs]^+ m/z 1165.4400$. b) Fragment ions from $SLe^X [M + 2Cs]^{2+} m/z 649.1724$ can be clustered into different trend lines in the mass defect vs. mass plot based on their Cs+ content..

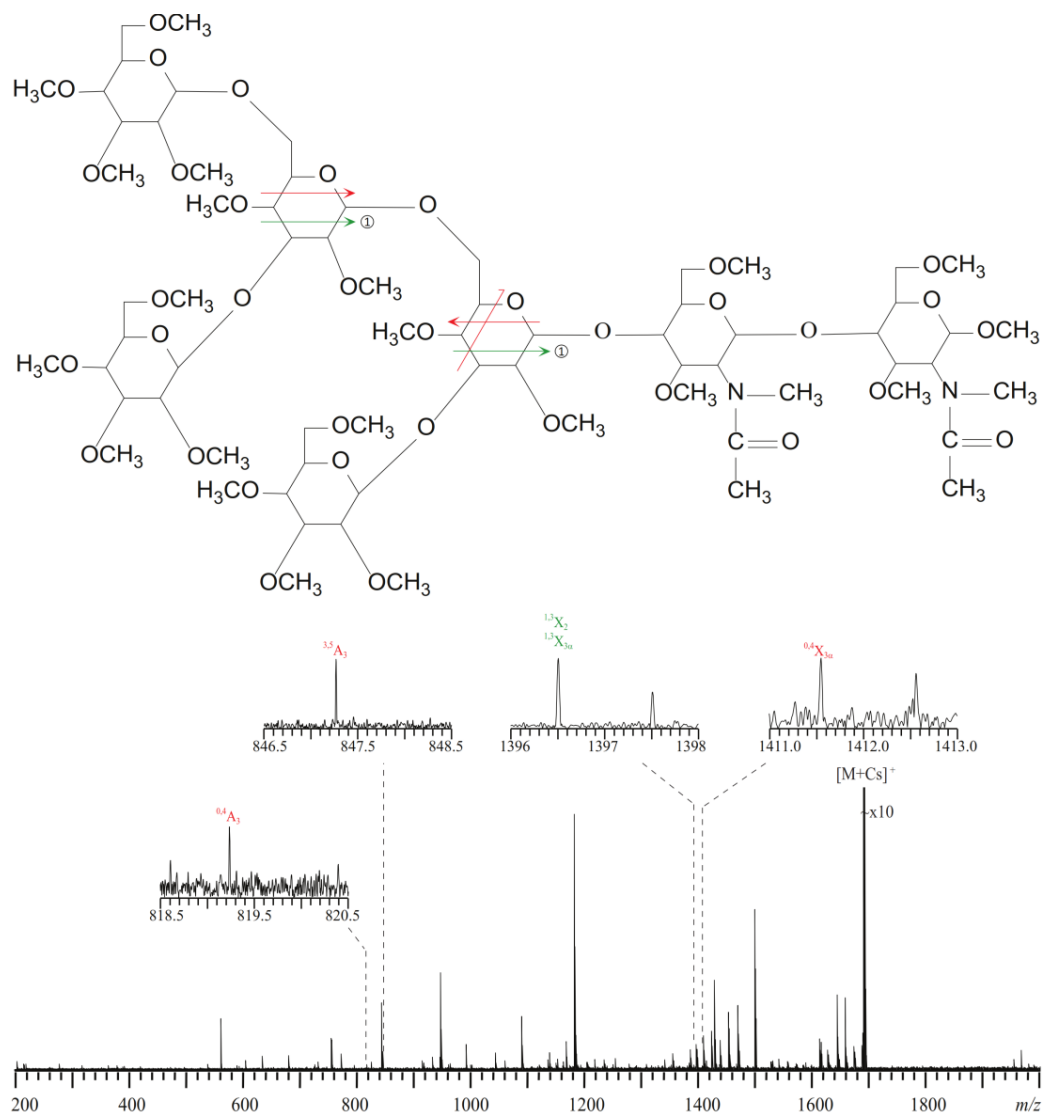


Figure 3.22 The EED cleavage map and single scan spectrum of the singly cesiated, permethylated, and ^{18}O -labeled $(\text{Man})_5(\text{GlcNAc})_2$.

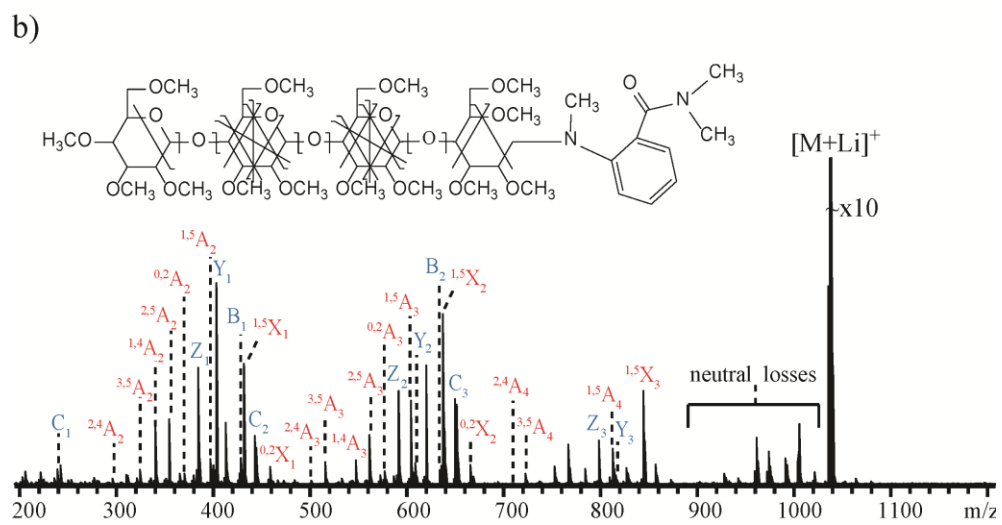
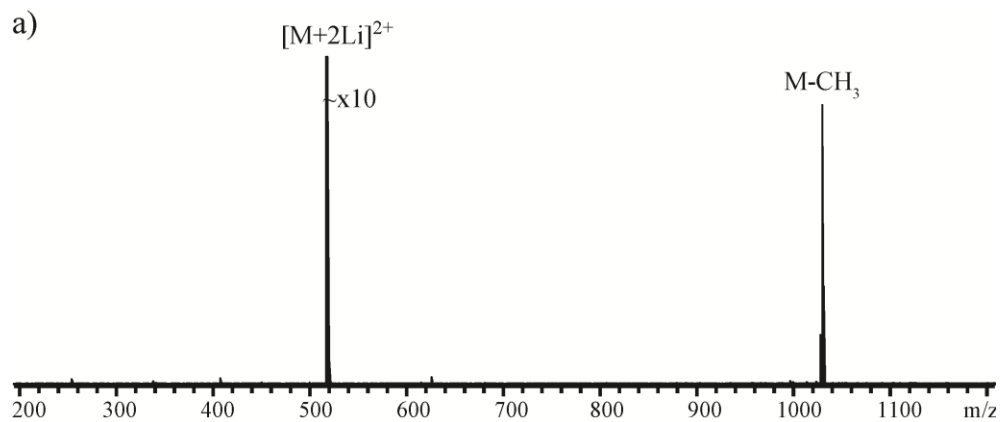


Figure 3.23 a) ECD of the $[M + 2Li]^{2+}$ m/z 519.2938 and b) EED of the $[M + Li]^+$ m/z 1031.5721 of 2-AB labeled, permethylated maltotetraose.

3.4 Conclusions

In conclusion, EED can provide rich structural information for a wide variety of glycans. Permethylation, reducing end labeling and high mass resolving power are helpful for accurate interpretation of the complex EED spectra. EED is amenable to analysis of singly charged precursor ions, although analysis of ions in higher charge states offers better detection efficiency, higher mass resolution and complementary fragment information. The charge-remote nature of the EED process allows a wider selection of metal charge carriers, among which Cs^+ is preferred, as it has a simple isotope composition and a large mass defect that enables reliable metal counting. With its high sensitivity, throughput, and compatibility with HPLC analysis of reducing-end labeled glycans, EED appears to hold great promise for large-scale glycomics studies.

Chapter 4 Top-down study of β 2-microglobulin deamidation

4.1 Introduction

Asparagine (Asn) deamidation plays an important role in aging and many protein misfolding diseases; it may also influence the stability of protein drugs^{63, 106-112}. Under neutral and basic conditions, Asn deamidation generates a mixture of isomeric acidic products, aspartic acid (Asp) and isoaspartic acid (isoAsp)¹¹³. Of the two, isoAsp formation has a more deleterious effect on the stability and function of the protein, because it inserts an extra methylene group to the polypeptide backbone, significantly altering the protein structure¹¹⁴. Thus, it is important not only to detect Asn deamidation but also to differentiate its isomeric products. Detection of deamidation is straightforward by mass spectrometry (MS) methods on the basis of the resulting mass shift of +0.984 Da per deamidation site. Several analytical methods exist for the differentiation of Asp and isoAsp residues, but each has its own limitations¹¹⁵⁻¹¹⁹. Recently, a tandem mass spectrometry (MS/MS) method was developed for the identification and quantification of isoAsp formation based on the presence and relative abundance of the isoAsp-specific diagnostic ion(s) (c+57 and z•-57) generated by either electron capture dissociation (ECD) or electron transfer dissociation (ETD)^{65-66, 120-122}. A high-throughput nanoLC-ESI-MS/MS (ECD) method was also developed for proteome-wide isoAsp mapping, which used the accurate mass of the isoAsp diagnostic fragment, as well as several other spectral and chromatographic parameters, to identify isoAsp-containing peptides¹²³⁻¹²⁴. However, such bottom-up approach requires enzymatic digestion which could potentially

introduce additional artifactual deamidation and other post-translational modifications¹²⁵. A top-down approach¹²⁶⁻¹²⁷ is thus preferred, where the intact protein is analyzed directly, providing a more accurate account of the biologically significant deamidation by eliminating additional sample preparation steps associated with enzymatic digestion. To date, however, isoAsp identification by ECD has only been demonstrated at the peptide level, with the largest reported being the Amyloid beta 1-42 fragment¹²⁸.

In this study, *in vitro* Asn deamidation and isoAsp formation in the protein beta-2-microglobulin (β_2M) was investigated by top-down ECD analysis. Human β_2M has important immunological functions. It is the non-covalently bound light chain of major histocompatibility complex (MHC) class I, which is required for antigen presentation to induce immunological responses. When an MHC class I molecule undergoes degradation, the heavy chain embedded in the cell surface is absorbed by endocytosis, releasing the monomeric β_2M into the circulation. Most of these β_2M molecules are filtered through the kidney glomeruli into the kidney tubules, where they are degraded by the tubular cells by pinocytosis¹²⁹⁻¹³⁰. In serum, β_2M is normally present at a low concentration of about 1.5-3 mg/L¹³¹. However, in the renal failure patients, the concentration of β_2M can rise 60-times higher and amyloid fibrils can be formed and deposited at the joints of patients inducing amyloidosis¹²⁹. Although the native monomeric β_2M does not readily form fibrils under physiological conditions, fibril formations can be accelerated in acidic solutions, in the presence of trace amount of pre-existing fibrils as “seeds”, or in the

presence of copper ions, Cu^{2+} ^{129-130, 132-135}. In addition, it was reported that $\beta_2\text{M}$ deamidation at Asn17 can lead to fibril formation at low pH ¹³⁶.

Human $\beta_2\text{M}$ is a small (~11.7 KDa), highly soluble, monomeric extracellular protein containing 99 amino acid residues¹³⁷. The native wild type $\beta_2\text{M}$ contains seven β -sheets and a single disulfide bond connecting Cys25 and Cys80^{129, 138}. $\beta_2\text{M}$ contains five Asn residues, including two in the fast-deamidating -NG- sequence. The relatively small size of and the presence of facile deamidation sites in $\beta_2\text{M}$ make it an ideal model system for testing the potential of ECD in top-down isoAsp analysis.

4.2 Experimental

4.2.1 Materials

Sequencing grade trypsin was purchased from Roche Applied Science (Indianapolis, IN). HPLC grade water and methanol were purchased from Honeywell/Burdick & Jackson (Muskegon, MI). Human β_2 M and all other chemicals were purchased from Sigma Aldrich (St. Louis, MO).

4.2.2 Reductive Alkylation and *In Vitro* Aging

Human β_2 M was reduced and alkylated, as described previously¹²⁵. Briefly, β_2 M was reduced in 6 M urea/50 mM ammonium bicarbonate buffer at pH 8, with a ten-fold molar excess of dithiothreitol over disulfide bonds. The resulting mixture was incubated at 37 °C for one hour. Iodoacetamide was then added to the mixture in a ten-fold molar excess over disulfide bonds, followed by incubation in dark at room temperature for one hour. The reduced and alkylated β_2 M protein was dried in speed vacuum and further purified by a home-made Poros 50 R1 packed solid-phase microextraction tip (Applied Biosystems, Foster City, CA). The eluted fractions (at 40%) were tested by electrospray ionization Fourier-transform ion cyclotron resonance mass spectrometry (ESI FTICR MS). The reduced and alkylated β_2 M protein was then aged *in vitro* in 0.1 M ammonium bicarbonate buffer at pH 8.3, 37 °C for five days.

4.2.3 Mass Spectrometry Analysis

All MS experiments were performed on a solariX 12 T hybrid Qh-FTICR mass spectrometer (Bruker Daltonics, Billerica, MA) equipped with a hollow cathode dispenser and a 25 W continuous wave CO₂ laser (Synrad model J48-2, Mukilteo, WA). The intact β_2 M protein was introduced into the mass spectrometer by nano-electrospray out of a pulled fused silica capillary with a 1 μ m orifice at 5 μ M concentration in an electrospray solution containing 49.5:49.5:1 methanol:H₂O:formic acid. The reduced and alkylated β_2 M protein, either unaged or aged, was washed twice with water and analyzed similarly at the same concentration. For top-down ECD analyses, molecular ions in a specific charge state were isolated by the front-end mass filtering quadrupole and fragmented in the ICR cell by irradiation of low-energy electrons for ~20 ms with the cathode bias set at -1 V and the heating current at 1.6 A. For MS³ experiments, molecular ions of all charge states were first dissociated by collisionally activated dissociation (CAD) in the funnel-skimmer region, and a fragment ion was further isolated by the quadrupole and fragmented by ECD. The collision energy was tuned to maximize the abundance of the specific fragment ion of interest. For activated ion (AI)-ECD experiments, ion activation was achieved by IR irradiation from the CO₂ laser prior to the ECD event. Because of the ion magnetron motion, the delay between the ion trapping event and the IR laser trigger needs to be adjusted to achieve optimum ion-electron overlap at the onset of the electron irradiation¹³⁹. All tandem mass spectra were internally calibrated with the precursor ion and a few fragment ions assigned with high confidence using the DataAnalysis software (Bruker Daltonics, Billerica, MA). Peak lists

were generated by the SNAP algorithm and interpreted manually with a typical mass accuracy of less than 1 ppm. All ESI-MS spectra were externally calibrated to avoid possible bias in internal calibration when assigning the isotope index to selected internal reference peaks, and the resulting mass accuracy was better than 3 ppm.

4.3 Results and Discussion

4.3.1 ESI-MS Analysis of the β_2 M Protein

The ESI mass spectra of the native and the reduced/alkylated β_2 M (Figures 4.1a and 4.1b) show charge state distributions from 7+ to 12+ and from 10+ to 16+, respectively. The shift towards higher charge states for the reduced/alkylated β_2 M is consistent with its more unfolded structure as expected after the disulfide bond breakage. Each charge state contains two isotopic clusters (Figures 4.1a and 4.1b, insets) corresponding to the molecular ion and its singly oxidized form, respectively. The ~16 Da mass increase resulted from the oxidization of the C-terminal methionine residue, as confirmed by the tandem mass spectra (not shown). The 116.24 Da mass difference between the two molecular ions corresponds to the addition of two carbamidomethyl groups, confirming the success of the reductive alkylation.

Figure 4.1c shows the ESI mass spectrum of the reduced/alkylated and aged β_2 M (hereafter referred to as the aged β_2 M, for short). The inset shows the enlarged region of its 14+ charge state. Once again, two isotopic clusters are present corresponding to the molecular ion and its oxidized form, respectively. The relative abundance of the oxidized form is higher in the aged sample, as a result of the extended exposure to oxygen during the aging process. The superior mass resolving power of the FTICR instrument allows accurate determination of the monoisotopic peak position (using the SNAP algorithm). The monoisotopic neutral mass of the aged β_2 M was determined to be 11840.80 Da,

which represents a +3 Da mass shift after the *in vitro* aging, suggesting that deamidation may have occurred at three Asn sites.

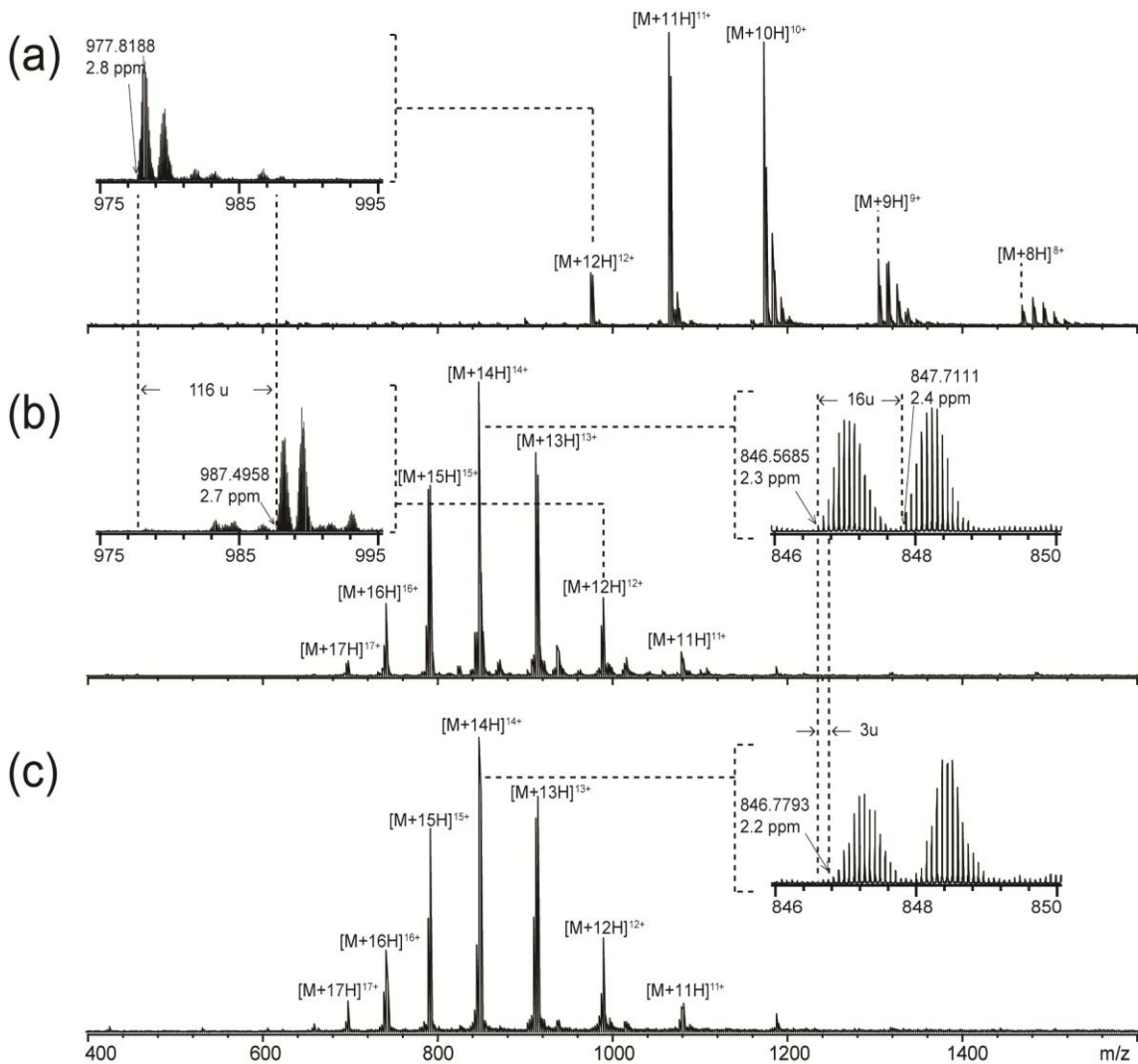


Figure 4.1 ESI mass spectra of the (a) native, (b) reduced/alkylated, and (c) reduced/alkylated and aged β_2 M. For each spectrum, a selected charge state is enlarged to illustrate the presence of two isotopic clusters (with or without Met oxidation) as well

as the mass shifts caused by reductive alkylation and Asn deamidations (insets). All m/z values listed are those of the monoisotopic peak as determined by the SNAP algorithm.

4.3.2 Top-Down ECD Analysis of the Aged β_2 M Protein

The ECD spectrum of the isolated unoxidized form of the aged β_2 M in its 14+ charge state is shown in Figure 4.2 (lower panels). For clarity, the spectrum is divided into four segments, and only sequence ions of the c- and z-types are labeled in the spectrum. The cleavage map is shown in the top panel, representing 88 out of the potential 93 inter-residue $N-C_\alpha$ bond cleavages, excluding cleavages N -terminal to a proline residue. Based on the mass difference of fragment ions in the ECD spectra of the unaged and the aged proteins (Figure 4.3), the three deamidation sites were localized to the Asn17, Asn42, and Asn83 residues. Further, a peak corresponding to the isoAsp diagnostic ion, $(c_{16}+57)^{3+}$, was observed with a mass accuracy of 0.3 ppm (Figure 4.2, inset), confirming the formation of isoAsp at the Asn17 deamidation site in the aged protein, which demonstrated the utility of ECD in isoAsp analysis using the top-down approach.

However, no isoAsp diagnostic ions were observed at either the Asn42 or the Asn83 deamidation site. This difficulty in isoAsp identification in intact proteins likely arises from the significantly increased number of available fragmentation channels that compete with diagnostic ion formation as the size of the protein increases. Moreover, fragment ion pair, formed after the $N-C_\alpha$ bond cleavage, could still be held together by extensive noncovalent interactions present in large proteins, preventing fragment ion separation and detection, further hindering the observation of diagnostic ions. These problems can be

alleviated by performing the ECD analysis on a smaller piece of the protein. Here, an MS³ (CAD/ECD) method was developed where the protein first underwent CAD and a fragment ion containing deamidation site(s) of interest was further selected and analyzed by ECD. Such gas-phase "digestion" can avoid the problem of artifactual deamidation encountered in traditional bottom-up approach that utilizes solution-phase enzymatic digestion to break down the proteins.

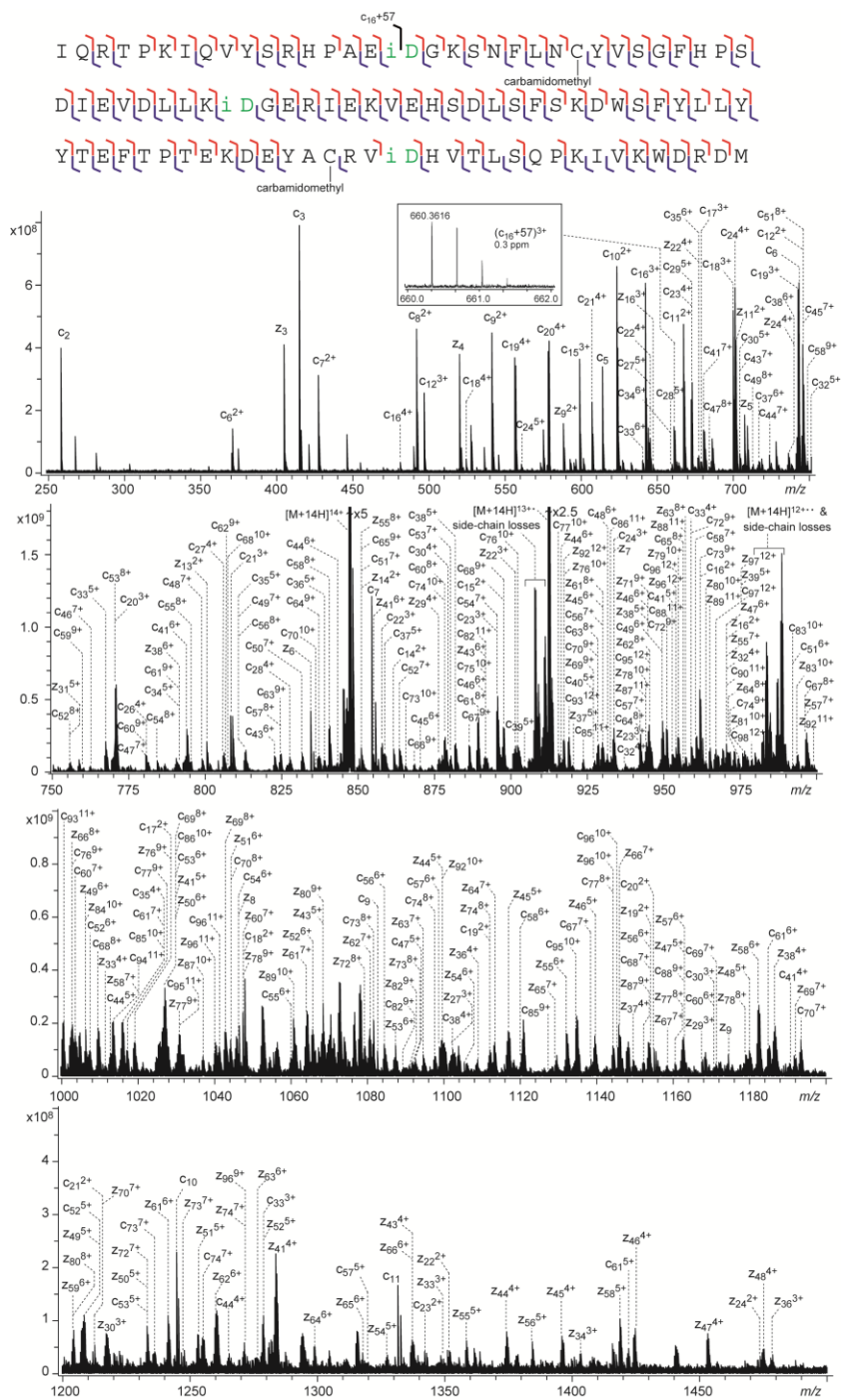


Figure 4.2 Top-down ECD spectrum of the reduced/alkylated and aged β_2 M in 14+ charge state, shown in four segments for clarity. The cleavage map is shown on top of the spectrum. The inset shows the *N*-terminal diagnostic ion for isoAsp17.

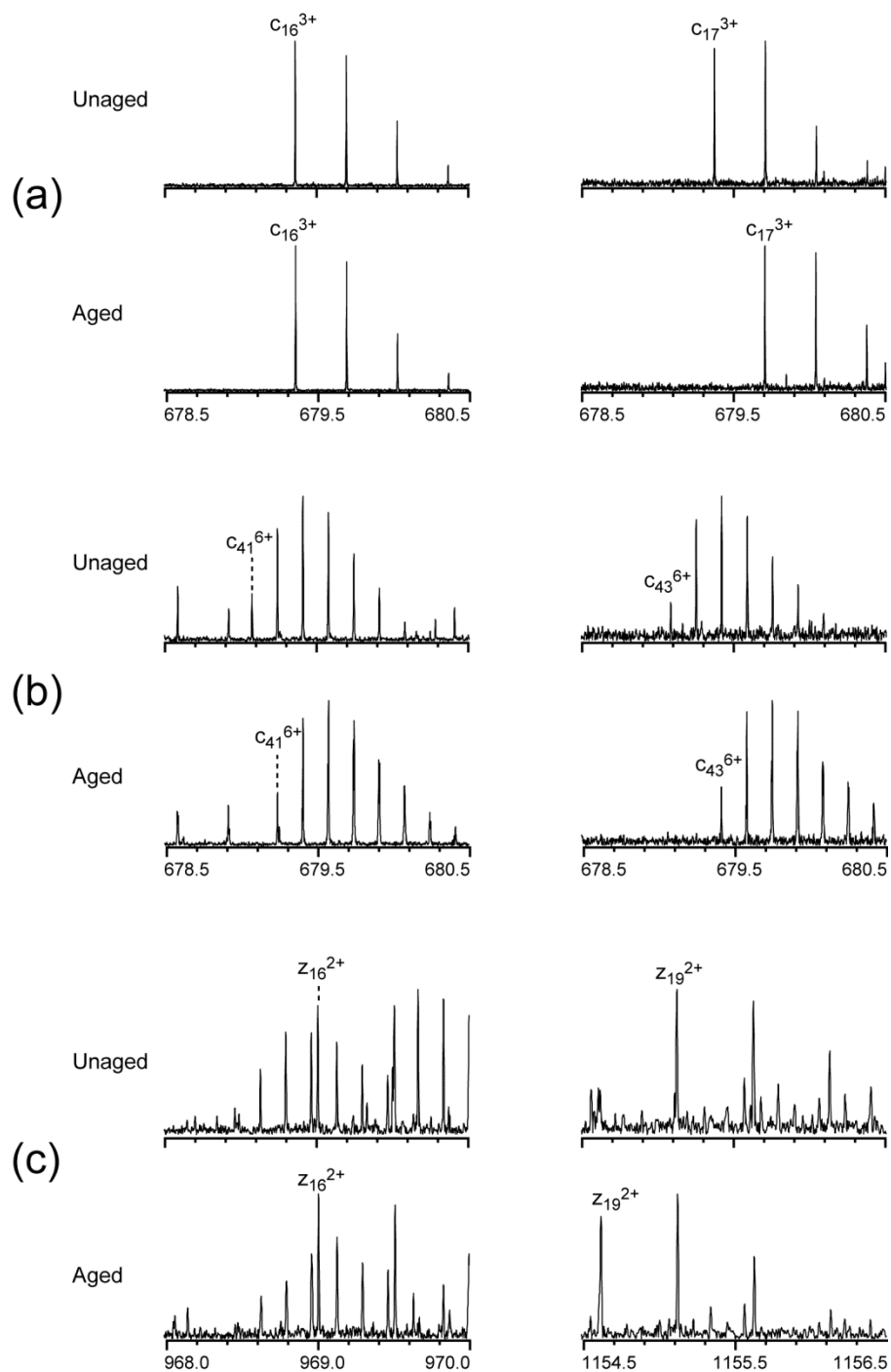


Figure 4.3 Enlarged regions of the ECD spectra of the unaged and the aged $\beta 2M$ for (a) c_{16}^{3+} and c_{17}^{3+} ions, (b) c_{41}^{6+} and c_{43}^{6+} ions, and (c) z_{16}^{2+} and z_{19}^{2+} ions.

4.3.3 Identification of isoAsp17 by NSD-ECD MS³ Analysis and Potential Interference from Sequence Scrambling

Figure 4.4 shows the CAD spectrum of the aged β_2 M generated by fragmentation in the funnel/skimmer region at a collision energy of 30 eV. No precursor ion selection was applied as the fragmentation occurred in a region before the mass filtering quadrupole. As a result, this nozzle-skimmer dissociation (NSD) spectrum contains many more peaks than that typically obtained by low-energy CAD of isolated precursor ions in a single charge state. Three fragment ions (Figure 4.4, insets) were chosen for further ECD analysis: the Asn17-containing b_{22}^{4+} , the Asn17- and Asn42-containing b_{63}^{9+} , and the Asn83-containing y_{28}^{5+} .

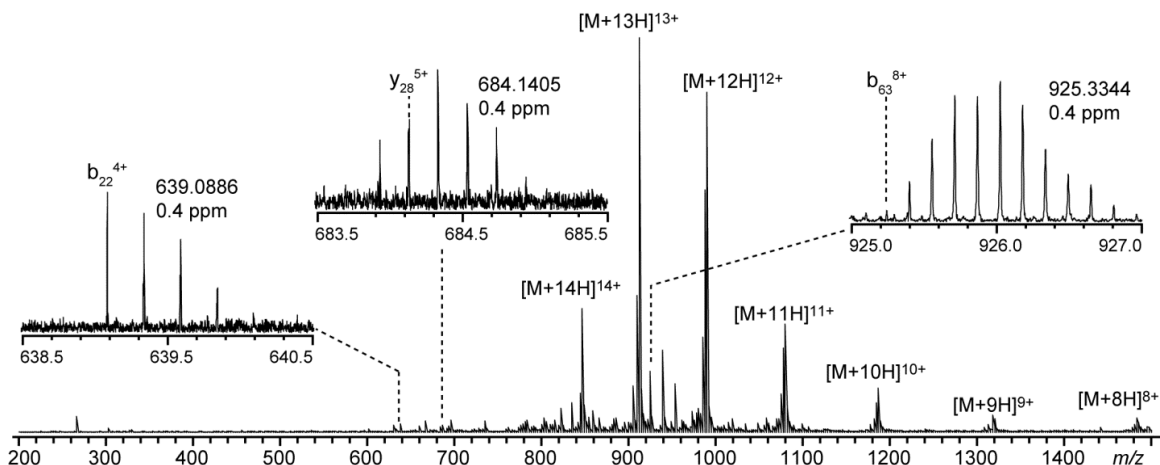


Figure 4.4 30 eV NSD spectrum of the aged β_2 M. Insets show the three isoAsp-containing fragments selected for further ECD analysis.

ECD of the b_{22}^{4+} ion generated from the aged β_2M provided a near complete series of inter-residue $N-C_\alpha$ bond cleavages in the N -terminal region of the aged β_2M protein (Figure 4.5, lower panel), as summarized in the cleavage map (Figure 4.5, top panel). The isoAsp diagnostic $(c_{16}+57)^{2+}$ and $(z_6-57)^+$ ions were also observed (Figure 4.5, insets), with a mass accuracy of 0.3 and 0.1 ppm, respectively, once again confirming the formation of isoAsp17. Thus, ECD can be successfully applied towards isoAsp identification not only in intact proteins, but also in fragments of a protein generated by gas-phase dissociation methods, as demonstrated here using the NSD-ECD MS³ approach.

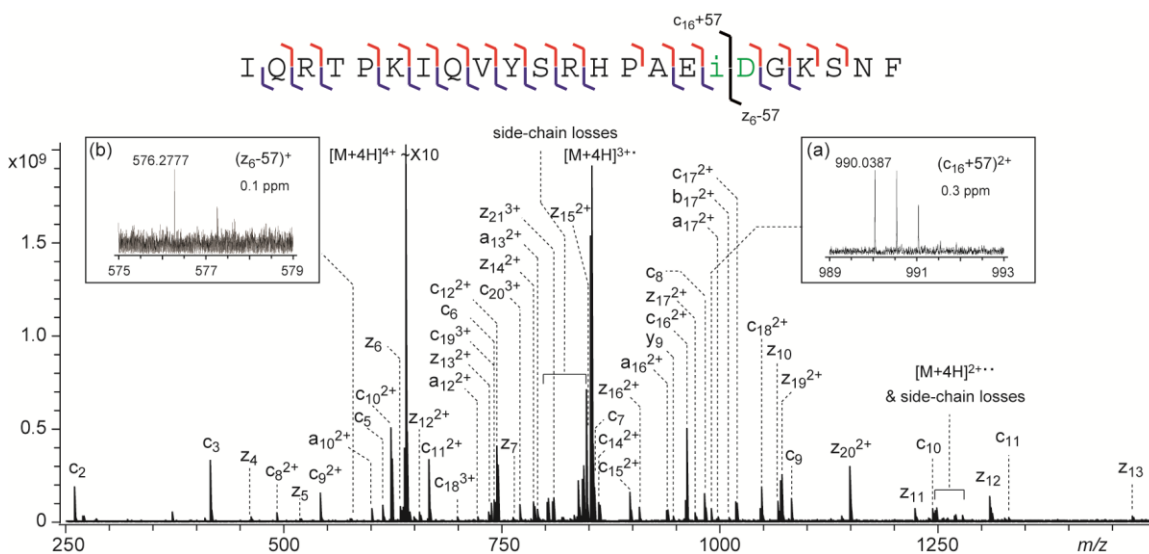


Figure 4.5 NSD-ECD spectrum of the b_{22}^{4+} ion generated from the aged β_2M , with the cleavage map shown on top of the spectrum. The inset shows the N -terminal diagnostic ion for isoAsp17.

A potential problem for such MS³ approach could arise if the selected b ion undergoes sequence scrambling before ECD. It is well known that some b ions can form a macrocyclic structure via head-to-tail cyclization. These macrocycles can reopen at different positions, generating a series of sequence-permuted linear b-ions, which could give rise to non-direct sequence ions when further fragmented by CAD¹⁴⁰⁻¹⁴¹. Sequence-scrambled fragment ions have also been observed in ECD of small b_n ions ($n = 5$ to 10)¹⁴². Despite its frequent occurrence in small and intermediate-sized b_n ions ($n \leq 10$), sequence scrambling was found to be statistically insignificant in a recent shotgun proteomics study by Zubarev and coworkers¹⁴³. Based on the analysis of 26,775 CAD spectra of doubly protonated tryptic peptides acquired with high mass resolution, they concluded that sequence scrambling via b-ion cyclization "can be safely ignored as a possible source of error in sequence assignment." Siu and coworkers also investigated sequence scrambling in CAD of a series of tryptic peptides from standard proteins. Although non-direct sequence ions were observed in 35% of the peptides studied, inclusion of these scrambled masses in database searches had little effect on protein matching scores, which led the authors to conclude that "sequence scrambling is unlikely to impact negatively on the accuracy of automated peptide and protein identifications in proteomics"¹⁴⁴. It is important to note that, although the presence of one or a few sequence scrambled fragment ions may not significantly impact the protein ID in proteomics, isoAsp analysis does not have the same statistical benefit, as it relies on the presence of a single (or a pair of complementary) diagnostic ion(s), often in low abundance, for isoAsp identification. Whereas chance of diagnostic ion's having the same

m/z value as that of a direct sequence ion is very low, chance of a spurious match could significantly increase when the b-ion sequence is permuted before ECD.

On the other hand, MS^3 is rarely needed for sequence analysis in the terminal region, because they are usually adequately covered by MS^2 experiments. Likewise, it is also relatively easy to identify isoAsp residues in the terminal region by MS^2 , as demonstrated by the successful detection of isoAsp17 in the aged β_2M protein shown above. Therefore, one should only concern sequence scrambling among large b-ions that contain isoAsp residues in the middle of the protein sequence, where the MS^3 approach is likely needed. Conceivably, sequence scrambling should become less a problem as the size of the b-ions increases, because of the unfavorable entropical factor for head-to-tail cyclization of larger b-ions. Surprisingly, Polfer and coworkers have recently reported that the relative intensity of non-direct sequence ions in low-energy CAD spectra of tryptic peptides increases with the peptide length¹⁴⁵. This seemingly surprising result can be partially attributed to the fact that the tandem mass spectra analyzed were obtained by performing low-energy CAD in a linear ion trap, where first-generation b-ions of various lengths could potentially cyclize and produce a large variety of sequence scrambled secondary fragment ions. In fact, most of the unambiguously identified non-direct sequence ions in the Polfer study were at lower mass, and likely formed from b-ions of smaller sizes. By contrast, in the NSD-ECD approach used here, a single b-ion was isolated for ECD analysis, which does not cause further sequence scrambling. Thus, one needs only to consider cyclization of the original b-ion, which is expected to become insignificant

when its size is sufficiently large. In the present study, nearly all peaks in the ECD spectrum of the b_{22}^{4+} ion of aged β_2M can be identified with high confidence as primary sequence ions, and the assigned isoAsp diagnostic peak is of far higher intensity than the few unassigned peaks present. Our result, as well as the lack of direct evidence for macrocycle formation in large b-ions (with 20+ residues) reported in literature, suggests that sequence scrambling is unlikely to be an issue for isoAsp analysis using the NSD-ECD approach adopted here.

4.3.4 Identification of isoAsp83 by NSD-ECD MS³ Analysis and Potential Interference from Co-isolation

Figure 4.6 shows the ECD spectrum of the y_{28}^{5+} ion from the aged β_2M , which contains the Asn83 deamidation site. A complete series of inter-residue $N-C_\alpha$ bond cleavages, excluding the one N -terminal to a proline residue, were observed. In comparison, four of the five missed cleavages in the top-down ECD analysis of the intact protein occurred in this same span of the C -terminal region of the protein (Figure 4.2). The fifth missed cleavage by top-down was recovered in the ECD spectrum of the b_{22}^{4+} ion (Figure 4.5). Thus, the MS³ approach can be a valuable tool for improving sequence coverage in protein sequence analysis. Similar improvement in sequence coverage by MS³ has been reported using an NSD-CAD approach on an LTQ-Orbitrap instrument¹⁴⁶. More importantly, and pertinent to the deamidation study, complementary isoAsp83 diagnostic $(z_{17-57})^{2+}$, $(z_{17-57})^{3+}$ and $(c_{11+57})^{2+}$ ions were identified with high mass accuracy (<0.2 ppm) in the ECD spectrum of the y_{28}^{5+} ion (Figure 4.6, insets), but were absent in the top-

down ECD spectrum, illustrating the utility and necessity of the NSD-ECD MS³ approach in isoAsp analysis of intact proteins.

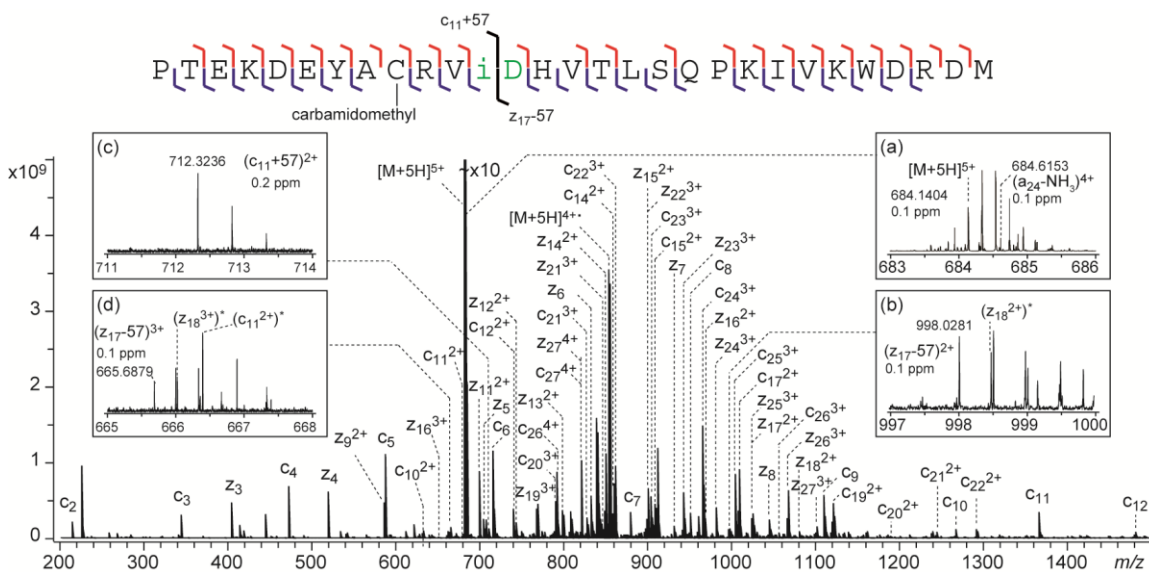


Figure 4.6 NSD-ECD spectrum of the y_{28}^{5+} ion generated from the aged β_2M , with the cleavage map shown on top of the spectrum. Inset (a) shows the enlarged region at the precursor ion m/z , insets (b-d) show the *N*- and *C*-terminal diagnostic ions for isoAsp83. * denotes peaks resulting from ECD of the co-isolated $(a_{24}-NH_3)^{4+}$ ion.

The majority of the peaks in Figure 4.6 can be assigned as primary sequence ions from the y_{28}^{5+} ion, and only those of the *c*- and *z*-types are labeled in the spectrum for clarity. However, a significant number of peaks cannot be interpreted as common ECD fragment ions (*a*-, *b*-, *c*-, *y*-, *z*-, or *w*-ions) from the y_{28}^{5+} ion. Because *y* ions are not known to undergo sequence scrambling, these unassigned ions are likely derived from different precursor ion(s). As shown in Figure 4.4, the y_{28}^{5+} ion was present in very low abundance

in the NSD spectrum of the aged β 2M. Thus, extended external accumulation of the isolated y_{28}^{5+} ion was needed to boost its population to a level appropriate for ECD analysis. As a result, other low-abundance fragment ions of similar m/z , even those absent in the NSD spectrum because of the space charge limit of the collision cell, could be co-isolated and accumulated externally to reach an abundance level high enough to generate ECD fragments. The top-right inset of Figure 4.6 shows the zoomed-in region of the y_{28}^{5+} ECD spectrum near its precursor ion m/z , where the presence of a second isotope cluster is evident in addition to the isotope cluster of the y_{28}^{5+} ion. The monoisotopic mass of this 4+ ion matches that of the $a_{24} - \text{NH}_3$ ion among all common CAD fragments that could be generated from the aged β 2M. This assignment is further confirmed by the observation of many low-abundance ECD fragments derived from the $(a_{24} - \text{NH}_3)^{4+}$ precursor. The top-left and bottom-right insets of Figure 4.6 show the enlarged region of the C-terminal isoAsp83 diagnostic ions, where interference peaks, labeled with an asterisk, from ECD of the $(a_{24} - \text{NH}_3)^{4+}$ ion are evident. In the example shown here, the A+1 isotope of the isoAsp diagnostic ions is 71 mDa heavier than the monoisotopic peak of the interfering $(z_{18}^{3+})^*$ peak, which can be easily distinguished by the FTICR mass analyzer. Although it is not common that an interfering fragment ion from a co-isolated precursor ion has an m/z value indistinguishable (by an FTICR analyzer) from that of the isoAsp diagnostic ion, it is important to examine such possibility when co-isolation is evident. In the rare case when the interfering fragment cannot be differentiated from the diagnostic ion, it is possible to perform ECD analysis

on a different NSD fragment ion (either in a different charge state or with a different length) to avoid such interference.

4.3.5 Identification of isoAsp42 by NSD-AI-ECD MS³ Analysis

As in the case of the Asn83 deamidation site, isoAsp formation at Asn42 cannot be confirmed by top-down ECD analysis of the intact aged β 2M. Even with the MS³ approach, detection of isoAsp42 is still very challenging. Unlike isoAsp17 and isoAsp83 which are located near the protein termini, isoAsp42 is located in the middle of the protein sequence, and most isoAsp42-containing NSD fragments were fairly large. None of the isoAsp42-containing NSD fragments analyzed produced isoAsp diagnostic ion(s) under ECD, which may arise from either slow product separation or restricted conformational access. Both restrictions may be lifted when the precursor ion is activated prior to ECD analysis. Figure 4.7 shows the AI-ECD spectrum of the b_{63}^{9+} ion, obtained by irradiating the precursor ion with 10.6 μ m IR light from the CO₂ laser (95% power) for 400 ms right before the ECD event. For clarity, the spectrum is divided into two segments, and only c- and z-type ions are labeled. Insets a and b show the enlarged region of the expected *N*-terminal isoAsp42 diagnostic ion in 6+ charge state in the (a) ECD and (b) AI-ECD spectrum of the b_{63}^{9+} ion. Whereas the ECD spectrum shows only noises in this region (inset a), the presence of a 6+ fragment ion is evident in the AI-ECD spectrum (inset b). The theoretical isotopic distribution of the $(c_{41+57})^{6+}$ ion is represented by circles in inset b, which matches well in m/z values with the isotope cluster observed experimentally, although the intensity match is only fair as the ion

abundance is too low to reach the statistical distribution. Because the monoisotopic peak is barely observable above the noise level, the experimental monoisotopic m/z value is derived from the A+1 and A+2 peaks, and is within 0.5 ppm of the theoretical value. IsoAsp formation at the Asn42 deamidation site is further confirmed by the presence of a C-terminal diagnostic ion, $(z_{22-57})^{2+}$, in both the AI-ECD (0.8 ppm, inset c) and ECD (0.3 ppm, inset d) spectra, although the S/N ratio is also fairly low.

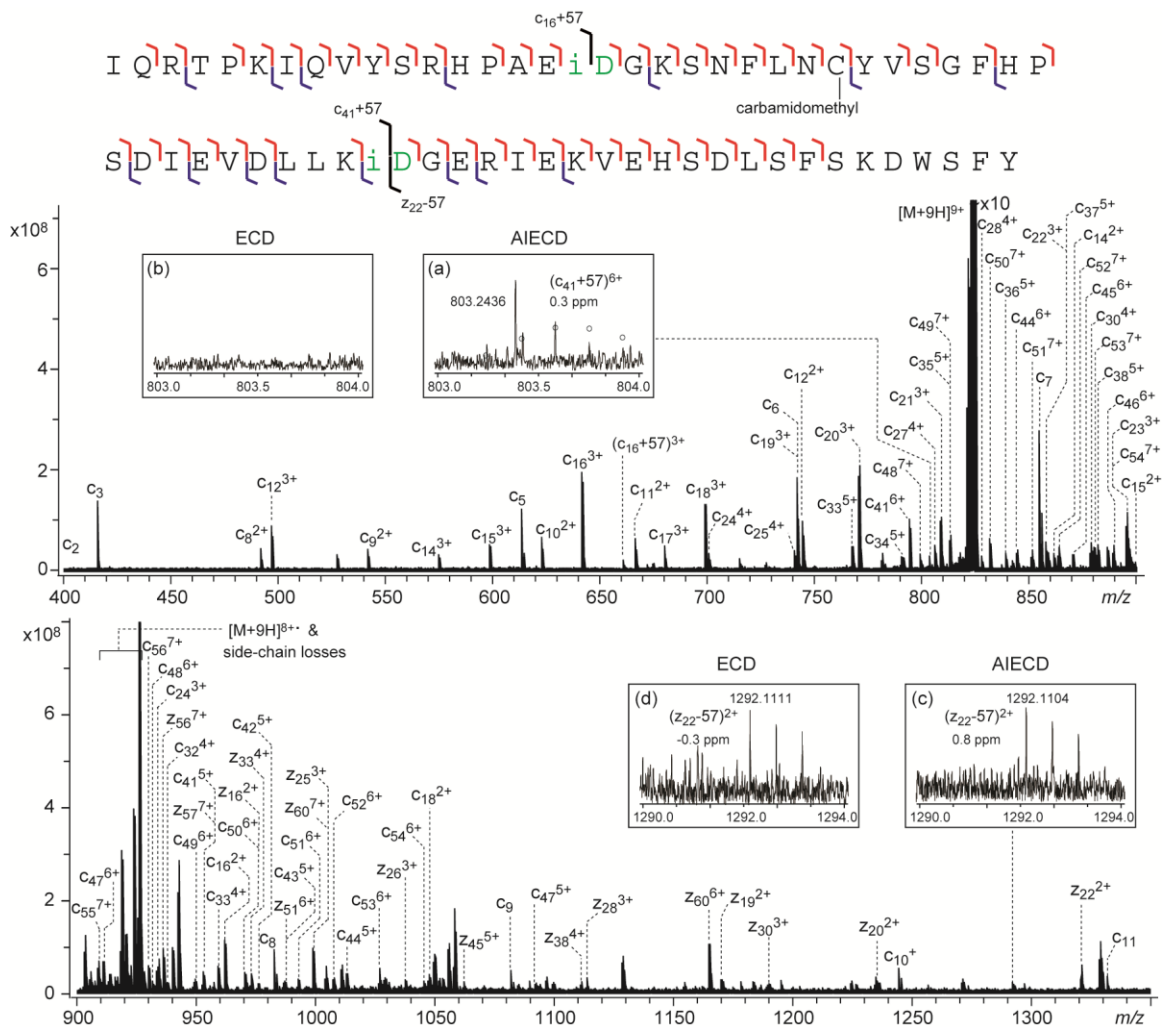


Figure 4.7 NSD-AI-ECD spectrum of the b_{63}^{9+} ion generated from the aged $\beta 2M$, shown in two segments for clarity. The cleavage map is shown on top of the spectrum. Insets (a) and (b) show the comparison between the NSD-AI-ECD and NSD-ECD spectra at the N-terminal isoAsp42 diagnostic ion region; insets (c) and (d) show the comparison at the C-terminal isoAsp42 diagnostic ion region.

Poor S/N ratio in NSD-AI-ECD spectra can be partially attributed to the difficulty in maintaining the optimum delay between ion and electron injection for best ion-electron

overlap and maximum ECD efficiency. Because the frequency of ion magnetron motion is dependent on the ion population ¹³⁹, fluctuation in ion abundance due to changes in efficiency of ionization, fragmentation or isolation can lead to significant decrease in ECD efficiency if the delay is not adjusted accordingly. This is a particularly severe problem when a prolonged period of IR irradiation is needed for efficient ion activation, during which time ions may complete multiple cycles of magnetron motion, and a small change in magnetron frequency could lead to a significant change in ion-electron overlap at the time of electron injection. This problem is further aggravated by the necessity of averaging multiple scans to achieve better S/N ratio, during which span ion abundance may change appreciably. In principle, problems associated with ion abundance variation inside the ICR cell could be mitigated by using the automatic gain control (AGC), although AGC was not implemented in this study. Nonetheless, the presence of complementary diagnostic ions assigned with high mass accuracy provides compelling evidence for isoAsp42 formation.

4.4 Conclusions

Using the protein β 2M as the model system, our study demonstrated the potential of ECD in isoAsp analysis at the intact protein level, which eliminates the need for and potential artifactual deamidation that could arise from enzymatic digestion prior to MS analysis. Top-down ECD analysis identified three Asn deamidation sites, but only detected isoAsp formation at one site. An NSD-ECD MS³ approach was developed which resulted in improved sequence coverage and positive isoAsp identification at all three deamidation sites. Sequence scrambling was not observed among the b-ions chosen for ECD analysis, and is not expected to cause false isoAsp identification using the NSD-ECD approach. False positives due to ion co-isolation are also unlikely when using a mass analyzer with a sufficiently high resolving power. However, when there are co-isolated precursor ion(s) present, it is important to examine the possibility of peak interference, and selection of a different precursor ion may be necessary for confident isoAsp diagnostic ion assignment. When the potential isoAsp formation site is in the middle of the protein sequence, ion activation may be needed to facilitate isoAsp diagnostic ion formation and detection. The top-down ECD and NSD-ECD MS³ approaches developed here appeared to be well suited for deamidation studies involving proteins of relatively small size, but may become increasingly more challenging as the size of the protein increases. Alternative methods, such as the middle-down approach, may be better suited for studying deamidation of large proteins.

Chapter 5 Middle-down Isoaspartic Acid Analysis by Glu-C Proteolysis and Electron Activated Dissociation

5.1 Introduction

Asparagine (Asn) deamidation and subsequent formation of aspartate (Asp) and isoaspartate (isoAsp) are spontaneous post-translational modifications (PTM) that occur under physiological conditions and have been associated with aging and protein misfolding diseases,⁵¹ including neurodegenerative disorders,⁵²⁻⁵³ apoptosis,⁵⁴⁻⁵⁵ autoimmunity,⁵⁶⁻⁵⁷ *etc.* The importance of isoAsp in the proteome remains underestimated due to the limitations of the currently available analytical tools.

Previous studies showed that the Asn deamidation rate depends on a number of factors such as protein primary sequences,⁵⁸⁻⁵⁹ higher order structures,⁶⁰ pH,⁶¹ temperature⁶² *etc.* To slow deamidation, control of pH is the most effective among all experimental parameters.¹⁴⁷ At pH < 3, deamination takes place via direct acid hydrolysis, producing only Asp. At pH > 4, deamidation occurs through a base-catalyzed pathway wherein the nitrogen of the protein backbone attacks the carbonyl group of the Asn side chain forming a cyclic succinimide intermediate with loss of ammonia. Carbonyl groups on this intermediate are then attacked by OH⁻ in aqueous solution and the residue undergoes rearrangement resulting in a mixture of Asp)and isoAsp (Figure 1.7). The rate limiting step is the formation of the cyclic succinimide intermediate. Base facilitates the deprotonation of the amide on the backbone making the nitrogen more nucleophilic and

therefore higher pH accelerates deamidation. Experimental data and theoretical calculations have also suggested that the deamidation rate reaches its minimum around pH 3 to 4.⁶¹⁻⁶² As a result, to inhibit deamidation and subsequent isoAsp formation, protein drugs and reagents are usually stored in mildly acidic buffer solutions at low temperatures.¹⁴⁷

Mass spectrometry (MS) methods are among the most widely applied techniques for analysis of deamidation and isoAsp formation, as they offer high sensitivity and require minimum sample preparation. Deamidation results in a mass shift of 0.984 Da from Asn to Asp/isoAsp, this difference can be readily measured with a Fourier transform ion cyclotron resonance (FT-ICR) mass spectrometer by envelope deconvolution methods.¹⁴⁸ However, isoAsp is still difficult to detect by single step MS because its mass is identical to Asp. Recently, electron capture dissociation (ECD)¹⁴⁹ and electron transfer dissociation (ETD)¹⁵⁰ based tandem mass spectrometry (MS/MS) methods have been developed to differentiate Asp from isoAsp on peptides. Unique isoAsp diagnostic ions, $c+57$ and $z-57$, resulting from C_{α} - C_{β} bond cleavage, can be produced through these two techniques.¹⁵¹

Most characterizations of post-translational modifications (PTMs) have been carried out through “bottom-up” approaches by first digesting the protein with trypsin before HPLC separation and MS interrogation. Despite its wide applications in proteomics research, for the identification of isoAsp, such “bottom-up” approaches carry the risk of introducing

artificial deamidation and isoAsp during the tryptic digestion. Therefore, instead of a normally overnight digestion, short trypsin digestion protocol, *e.g.* less than 4 hours, was recommended.¹⁵² However, a short digestion time may fail to produce sufficient target peptides for large quantities of big protein complexes. In addition, trypsin digestion sometimes produces N-terminal isoAsp, whose detection may be compromised by the presence of isobaric ion species.¹⁵³

As an alternative approach, “top-down” strategies were also developed for the Asn deamidation and isoAsp characterizations.¹⁵⁴⁻¹⁵⁵ Although no artificial isoAsp formation is involved in “top-down” MS/MS, its fragmentation efficiency is usually low because intramolecular interactions hinder the separation of fragments in the gas phase. Ion activation (AI) by infrared laser helps to overcome the intramolecular interactions but will eventually fail for larger proteins.¹⁵⁶ To reduce a large protein or protein complex to a manageable size, instead of enzymatic digestion, our group designed a comprehensive “top-down” strategy by first performing a gas phase digestion of proteins using nozzle skimmer dissociation (NSD). Fragments of interest were then selected and subjected to ECD.¹⁵⁵

Recently, “middle-down” MS is emerging, since it takes advantage of both “bottom-up” and “top-down” MS.¹⁵⁷⁻¹⁵⁸ “Middle-down” involves analysis of polypeptides larger than 3000 Da, usually resulting from protein digestion with Lys-C, Asp-N, or Glu-C. MS/MS interrogation of such long polypeptides is usually efficient and it preserves the

combinatorial PTMs. W. Ni et al. employed Asp-N to characterize Asp versus isoAsp,¹⁵⁹ but the occurrence of artifactual deamidation and isoAsp formation remained as a challenge because the optimal digestion condition for Asp-N is still around pH 8.0.

As the deamidation rate is affected mostly by pH and reaches its minimum around pH 3 to 4,⁶¹ a rational selection of the pH for enzymatic digestion is the key to avoiding false positive results in both deamidation and isoAsp analysis. Endoproteinase Glu-C is a serine proteinase that is widely used in proteomics studies. It cleaves specifically at glutamyl bonds in ammonium acetate and ammonium bicarbonate buffered solutions, whereas in phosphate buffer it cleaves both glutamyl bonds and aspartyl bonds. It should be noted that the maximum proteolytic activity of Glu-C has been reported to be at pH 4.0 and 7.8,¹⁶⁰⁻¹⁶¹ a range which includes the pH where the Asn deamidation rate reaches its minimum. Under this rationalization, Glu-C digestion at pH 4.0 could probably be a valuable enzymatic tool to reduce the protein size without generation of artifactual deamidation and subsequent formation of isoAsp.

This study investigated the formations of artifactual deamidation and isoAsp during Glu-C digestion under different conditions of pH and temperature. Our results suggest that the Glu-C “middle-down” approach we report here is free of artifacts, thus allowing reliable isoAsp characterization and quantitation.

5.2 Experimental

5.2.1 Materials

The sequencing grade trypsin was purchased from Promega (Madison, WI). Synthetic peptides $VE_{(iso)}DARDFFLK_{(iso)}DAEDVR$ (BUXY1) and $VEDAR_{(iso)}DFFLKDAE_{(iso)}DVR$ (BUXY2) were obtained from AnaSpec (Fremont, CA). All other chemicals and proteins, including endoproteinase Glu-C (Glu-C), ribonuclease A (RNase A) from bovine pancreas and β -2-microglobulin (β 2M) from human urine were obtained from Sigma Aldrich (St. Louis, MO).

5.2.2 Sample Preparation

Native RNase A and β 2M were reduced, alkylated and desalted as described previously.¹⁵¹ Aged proteins were obtained by incubating the reduced and alkylated proteins in pH 7.8 ammonium bicarbonate buffer solution for 2 weeks (RNaseA) and 1 week (β 2M). For tryptic digestion, the proteins were mixed with trypsin at 1:50 (w/w) and were incubated in ammonium bicarbonate buffer for 16 h at 37 °C. For Glu-C digestion, proteins were mixed with endoproteinase Glu-C at 1:50 (w/w) in either the pH 7.8 ammonium bicarbonate buffer solution or the pH 4.0 ammonium acetate buffer solution, at either 25 °C or 37 °C. Desalting using Poros 50 R1 (Applied Biosystems, Foster City, CA) was performed as previously reported.¹⁵¹

5.2.3 Reversed Phase High Performance Liquid Chromatography (RP-HPLC)

RP-HPLC separations were achieved with a Vydac 218TP5215 reversed phase C18 column (4.6 ×250 mm) on an Agilent 1200 Series HPLC system (Agilent Technologies, Wilmington, DE, USA). Mobile phase A was 99% water, 1% acetonitrile, and 0.1% trifluoroacetic acid (TFA). Mobile phase B was 99% acetonitrile, 1% water, and 0.1% TFA. A linear gradient of 5%-95% of mobile phase B in 30 min was running at a flow rate of 1 ml/min at 30 °C. The chromatograms were obtained using a 214 nm UV detector and fractions corresponding to the chromatographic peaks were collected at 4 °C before MS analysis.

5.2.4 Instrumentation

The overall peptide profiles resulting from enzymatic digestions were examined on the Reflex IV MALDI-TOF mass spectrometer (Bruker Daltonics, Billerica, MA) equipped with a 337 nm ultraviolet laser. All electron activated dissociation (ExD) experiments were carried out on the 12 Tesla solarix™ hybrid Qq-FT-ICR mass spectrometer equipped with an indirectly heated hollow dispenser cathode and a 10.6 μm CO₂ laser (Bruker Daltonics, Billerica, MA). Samples were directly infused into the mass spectrometer by applying a 1.1-1.2 kV spray voltage through the TriVersa NanoMate (Advion, Ithaca, NY). Target ions were isolated with the front-end quadrupole and accumulated in the collision cell for 100 to 500 ms before being transferred to the ICR cell. For ECD experiments, the precursor ions were irradiated with ~1.5 eV electrons for 100 ms; for hot-ECD experiments, the precursor ions were irradiated with ~14.0 eV

electrons, for up to 500 ms. For AI-ECD experiments, the precursor ions were first activated by the 10.6 μm laser for 200-500 ms prior to their irradiation by ~ 1.5 eV electrons. The cathode heating current was from 1.3 A to 1.5 A. A 0.5-s transient was typically acquired for each scan, except for some special cases, in which the ultra-high resolving power was necessary. Each spectrum shown represents the results of 100 to 200 transients summed to improve the signal-to-noise ratio.

5.2.5 Data Analysis

All spectra were zero-filled twice and Fourier transformed without apodization. The tandem mass spectra were calibrated internally using the precursor ion and a few fragment ions assigned with high confidence, giving a typical mass measurement accuracy better than 3 ppm. Deconvoluted mass lists were generated semi-automatically by the SNAPTM algorithm using the Data AnalysisTM software (version 4.0, Bruker Daltonics, Billerica, MA). Software used to assist data analysis included the Protein ProspectorTM (version 5.9.2) and a home-made Visual Basic program for auto-assignments.

5.3 Results and Discussion

Ribonuclease A (RNaseA) was chosen as the model system because its Asn deamination rate and the patterns of the isoAsp formation have been well studied.^{151, 154, 162} Peptides containing Asn 67 were preferentially selected as Asn 67 is the initial deamidation site and forms a mixture of Asp/isoAsp 67.¹⁵⁴ All cysteinyl residues (Cys) were reduced and alkylated by treatment with dithiothreitol (DTT) and iodoacetamide and are labeled as “C*”.

5.3.1 Challenges in Analyzing the N-terminal Isoaspartate of Tryptic Peptides

The isoAsp 67 formed after 2 weeks' aging is preceded by a lysine residue and is therefore part of a potential trypsin digestion site, but it remains unknown whether such β peptide bond is cleavable by trypsin. To determine whether tryptic cleavage could occur at such a position, we designed and synthesized complementary control peptides, BUXY1 and BUXY2, in which isoAsp follows immediately after either lysine or arginine. After overnight digestion under 37 °C, BUXY1 and BUXY2 produced isomeric tryptic peptides (Figure 5.1). The detection of DFFLK in the BUXY1 spectrum (Figure 5.1a) and _(iso)DFFLK in the BUXY2 spectrum (Figure 5.1b) supports the hypothesis that trypsin is capable of cleaving β -peptide bonds.

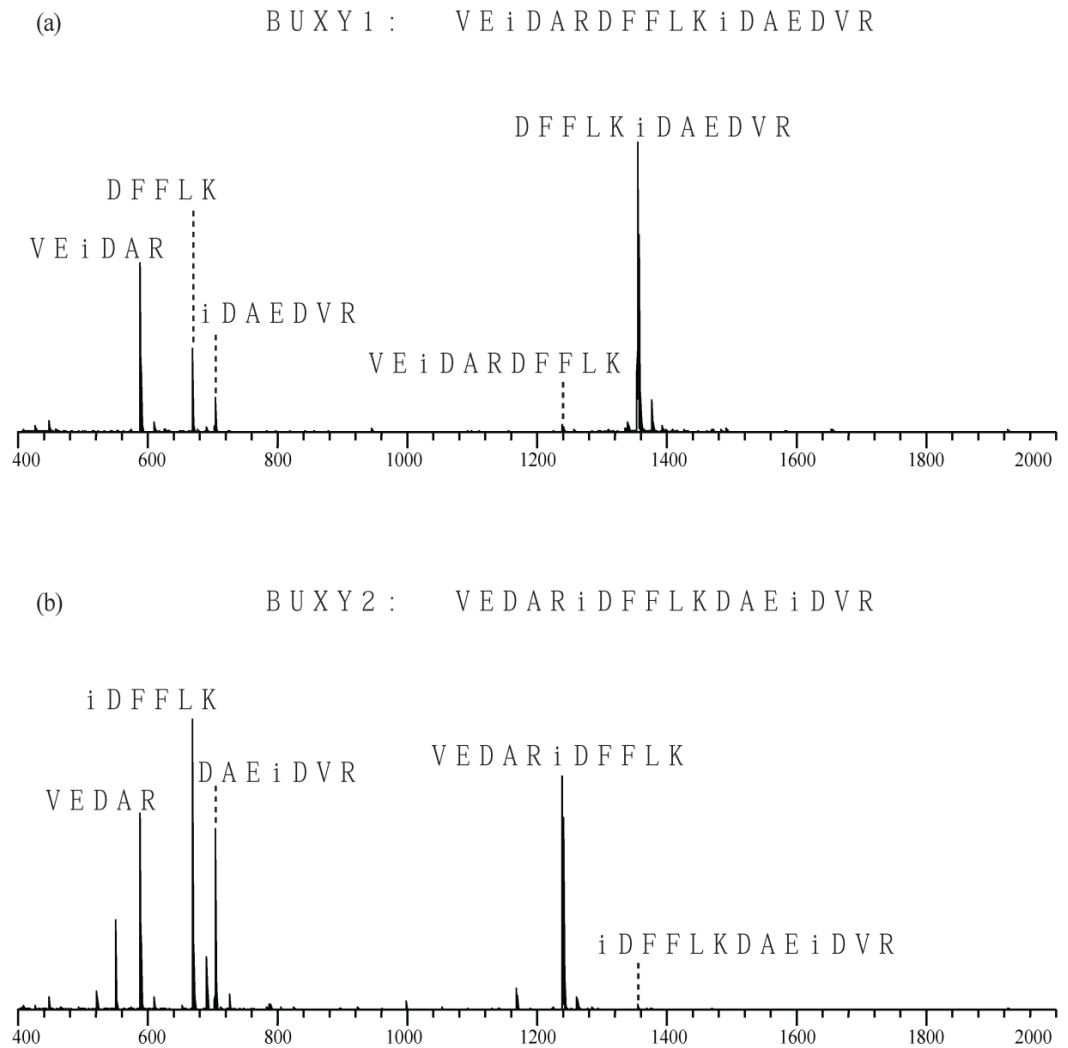


Figure 5.1 MALDI-TOF MS spectra of the synthetic peptides BUXY1 (a) and BUXY2 (b) after 18-h overnight trypsin digestion in pH 7.8 buffer solution at 37 °C.

Based on the conclusion drawn from the example above, the tryptic digestion of the aged RNase A can theoretically give rise to peptides that have an Asp/isoAsp residue on their N-terminus ($^{67}\text{D}/_{(\text{iso})}\text{DGQTNC}^*\text{YQSYSTMSITDC}^*\text{R}^{86}$). To identify N-terminal isoAsp residues, Sargaeva et al. reported MS/MS analyses based on ECD and ETD in which the

diagnostic ion, $[M+nH-74.0242]^{(n-1)+}$. was detected.¹⁵³ Unfortunately, ECD could also produce isobaric fragment ions via the methionine (Met) side chain loss ($[M+nH-74.0190]^{(n-1)+}$), which have only a 5.2-mDa difference from the N-terminal isoAsp diagnostic ion. In this example, the theoretical masses are 2213.8890 Da for the diagnostic ion and 2213.8942 Da for the isobaric ion. To reach a baseline separation, if both species should be present, at least 880,000 resolving power is required. In this situation, without additional sample modifications (e.g. N-terminal acetylation), isoAsp analysis of such tryptic peptides would require at least a 10-second transient on a 12 T FT-ICR mass spectrometer (data not shown). If only one of the isobaric ions is present, a mass accuracy better than +/- 2 ppm should be achieved. In conclusion, the trypsin-based “bottom-up” approach is risky because not only it has the problem of introducing artifactual isoAsp, but also isoAsp characterization using this approach could be difficult because of potential interfering isobaric ions if the isoAsp formed follows a Lys or Arg residue in the sequence.

5.3.2 Influencing Factors of the Asn Deamidation Rate during the Glu-C Digestion

In order to estimate the Asn deamidation rate at different pH and temperature values during the Glu-C digestion, an 18-h time course study was carried out for the Asn 67 containing peptides. Glu-C digestions were performed either at room temperature (25 °C) or at physiological temperature (37 °C). The quadruply charged peptide from the Glu-C digestion (⁵⁰SLADVQAVC*SQKNVAC*KNGQTNC*YQSYSTMSITDC*RE⁸⁷) was

monitored by the mass spectrometer. As shown in Figure 5.2, at pH 7.8, 25 °C, no obvious mass shift was found after 4-h digestion, whereas the isotope distribution of the same peptide shifted 1 Da towards higher mass after 9-h digestion and shifted even more after 18-h digestion (Figure 5.2, left column). These isotope envelope shifts indicated the occurrence of Asn deamidation which was also observed during tryptic digestion of the same protein.¹⁵² At pH 4.0, 25 °C, however, no obvious mass shift was observed even after 18-h digestion (Figure 5.2, right column), indicating no detectable deamidation occurred during an overnight Glu-C digestion at pH 4.0. Even at 37 °C, a temperature that is expected to increase the deamidation rate,¹⁶³ no deamidation was detected after 18 hours' digestion (Figure 5.3). These results confirmed that the Glu-C overnight digestion at pH 4.0 is free of artifactual deamidations.

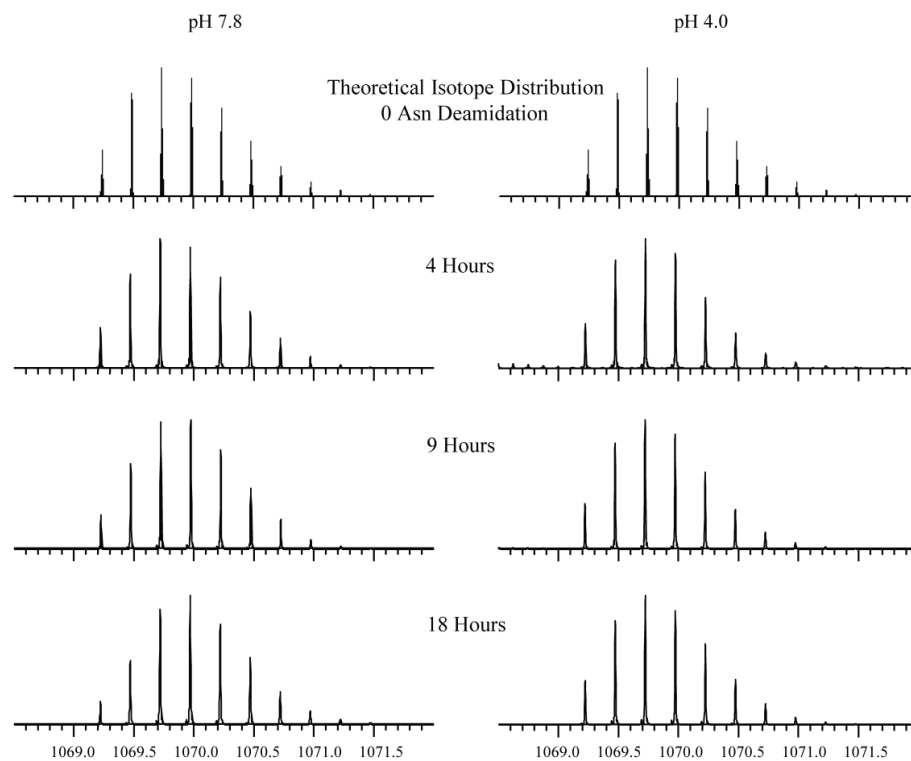


Figure 5.2 Isotope patterns of the quadruply charged, unaged RNaseA peptides derived from $(^{50}\text{SLADVQAVC}^*\text{SQKNVAC}^*\text{KNGQTNC}^*\text{YQSYSTMSITDC}^*\text{RE}^{87})$ and extracted at different times during the Glu-C digestion in a solution buffered at pH 7.8 (left column) and pH 4.0 (right column) at 25 °C. The theoretical distribution of the unaged form of the same peptide is shown at the top of each column.

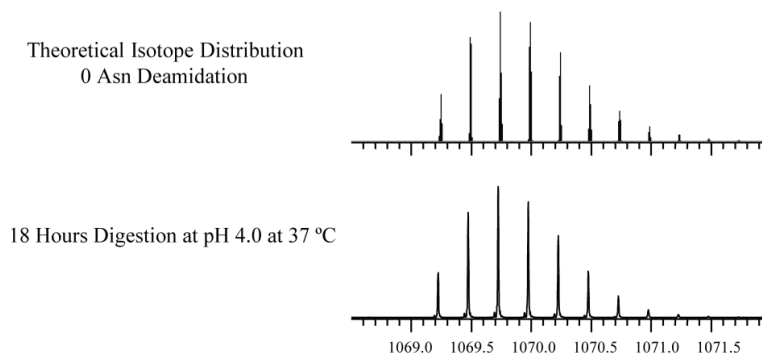


Figure 5.3 The isotope pattern of the quadruply charged unaged RNaseA peptide ($^{50}\text{SLADVQAVC}^*\text{SQKNVAC}^*\text{KNGQTNC}^*\text{YQSYSTMSITDC}^*\text{RE}^{87}$) extracted after 18-h Glu-C digestion in buffer solutions at pH 4.0 at 37 °C. The theoretical distribution of the unaged form of the same peptide is shown at the top for comparison.

5.3.3 Detection of isoAsp Formation through Electron Activated Dissociation and Charge State Pumping

Glu-C digestion usually produces peptides longer than tryptic peptides due to the lower frequency of occurrence of glutamic acid residues in mammalian proteins. For example, in humans, the codon usage frequency for glutamic acid residues (6.86%) is much lower than lysine (5.63%) and arginine residues (5.67%) combined (Data from NCBI-GenBank). Because ECD fragmentation is generally less efficient for very long peptides, the large size of the peptides produced by the Glu-C digestion could pose a potential problem for the ECD interrogation of isoAsp. To develop a reliable MS/MS method for the isoAsp identification, peptides from the Glu-C digestion of the aged RNaseA, $^{50}\text{SLADVQAVC}^*\text{SQKNVAC}^*\text{K}(\text{D}/\text{isoD})\text{GQT}(\text{N}/\text{D}/\text{isoD})\text{C}^*\text{YQSYSTMSITDC}^*\text{RE}^{87}$,

were selected and isolated as the precursor ions for MS/MS experiments (Figure 5.4). The mass spectral profile showed that the isotope distribution of this precursor ion shifted ~2 Da compared with the unaged control, suggesting 2 potential deamidation sites (Figure 5.5).

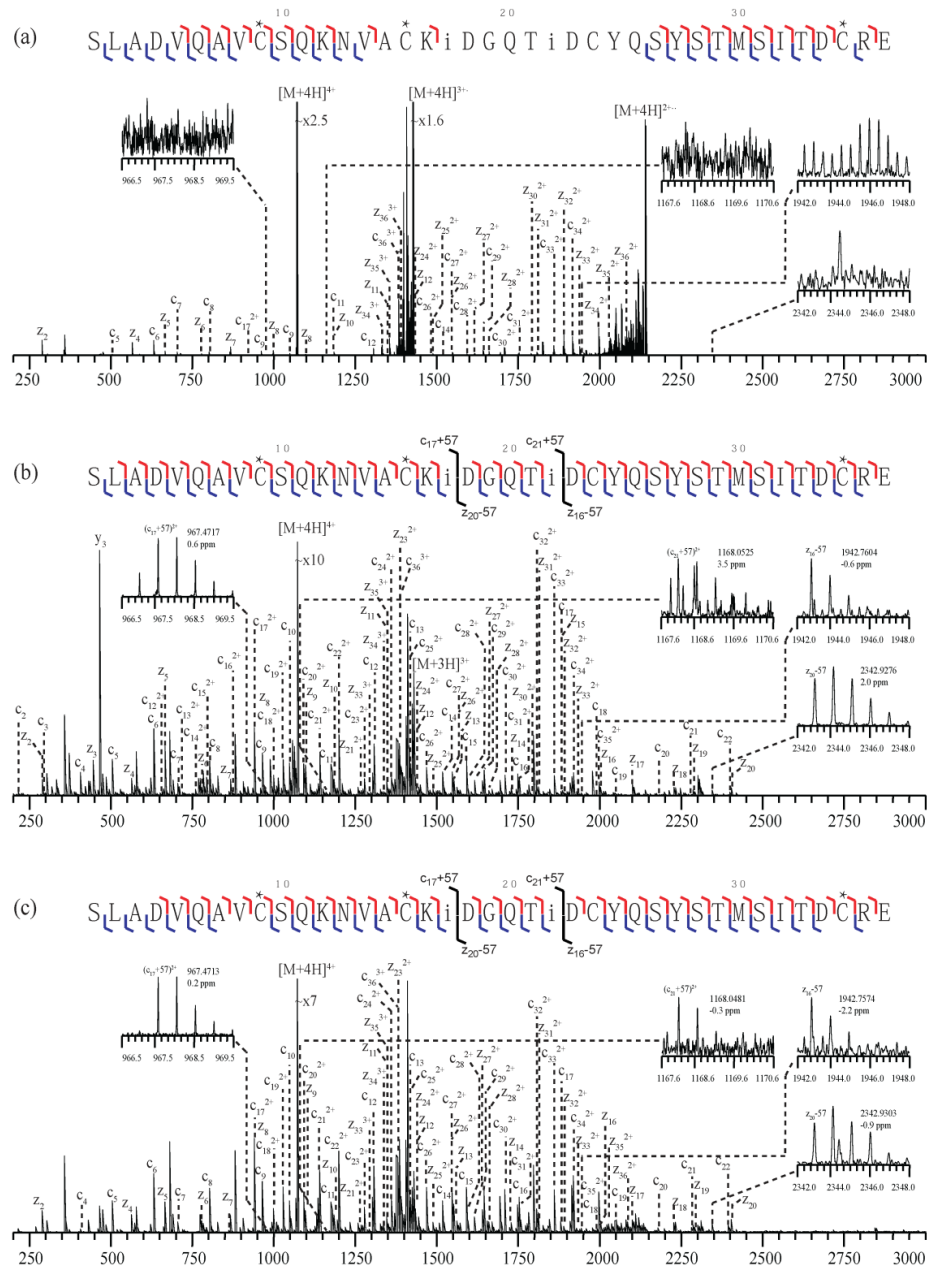


Figure 5.4 ExD spectra and c, z cleavage maps of the quadruply charged aged RNaseA peptide

(50 SLADVQAVC*SQKNVAC*K(D/isoD)GQT(N/D/isoD)C*YQSYSTMSITDC*RE 87):

(a) ECD, (b) hot-ECD, and (c) AI-ECD spectra. Insets show the absence or the presence of the diagnostic ions of isoAsp 67 and isoAsp 71.

Figure 5.4a shows the ECD spectrum of the quadruply charged precursor ion acquired with ~1.5 eV electron irradiation. ECD produced mostly charge reduced species and only limited sequence coverage. Most c, z cleavages were found at the terminal regions of the peptide and no isoAsp diagnostic ion was identified (Figure 5.4a).

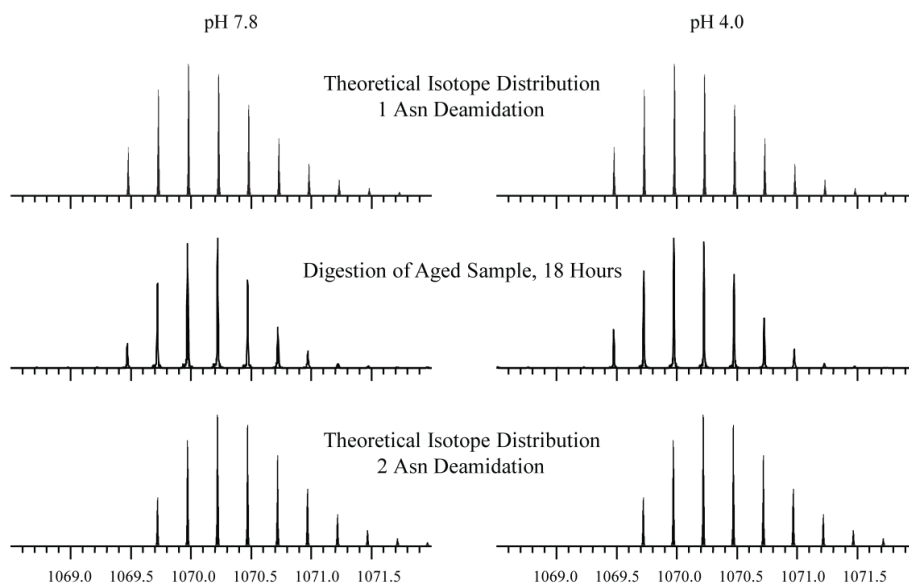


Figure 5.5 The isotope pattern shifts of the quadruply charged aged RNaseA peptides ($^{50}\text{SLADVQAVC}^*\text{SQKNVAC}^*\text{KDGQTDC}^*\text{YQSYSTMSITDC}^*\text{RE}^{87}$) extracted after 18-h Glu-C digestions in buffer solutions at pH 7.8 (left column) and pH 4.0 (right column) at 25 °C. For comparison, the theoretical distributions of the same peptides with 1 and 2 deamidation sites are shown at the top and bottom of each column.

To improve the ECD fragmentation efficiency, hot-ECD using electrons with higher kinetic energy was performed on the same precursor ion. Upon irradiation by 14.0-eV electrons, the fragmentation efficiency was significantly increased, with generation of full sequence coverage from c and z cleavages (Figure 5.4b). Diagnostic ion pairs for both isoAsp67 ((c₁₇+57)²⁺, (z₂₀-57)⁺) and isoAsp71 ((c₂₁+57)²⁺, (z₁₆-57)⁺) were identified, and these fragments verified the formation of a secondary isoAsp on the aged RNaseA. Although electrons with higher energies are capable of achieving higher fragmentation efficiency, several fragmentation processes could also occur upon the irradiation of high energy electrons, including hot-ECD, electronic excitation dissociation (EED) and electron-impact excitation of ions from organics (EIEIO).²² Consequently, for the hot-ECD spectrum presented here, extensive b, y fragments and fragments from secondary cleavages were also identified, which may interfere the identification of the isoAsp diagnostic ions (e.g. (c₂₁+57)²⁺ in Figure 5.4b), and may also complicate overall data interpretation.

An alternative approach to improve the ECD fragmentation efficiency is activated ion-ECD (AI-ECD), in which infrared laser irradiation is used prior to ECD to reduce the intramolecular interactions.¹⁵⁶ As shown in Figure 5.4c, AI-ECD produced c and z cleavages that provided full sequence coverage without introducing the extensive interfering peaks that were observed in the hot-ECD spectrum. All diagnostic ion pairs for isoAsp67 and isoAsp71 were readily detected.

The generation of higher charge states has also been reported as a way to enhance ETD fragmentation efficiency by changing the gas phase conformation of peptide molecules.¹⁶⁴ Among the supercharging reagents, sulfolane has been reported to produce the greatest charge increase.¹⁶⁵ In the example reported here, doping 10 mM sulfolane into the ESI solution increased generation of the 5+ supercharged precursor ions. As shown in Figure 5.6, the supercharged ion underwent more extensively ECD fragmentation than its 4+ counterpart. All isoAsp diagnostic ions were detected. However, because supercharging requires the use of high concentration sulfolane which is a non-volatile additive that may build up in the ion source, it was not used for the studies whose results are reported in the following sections.

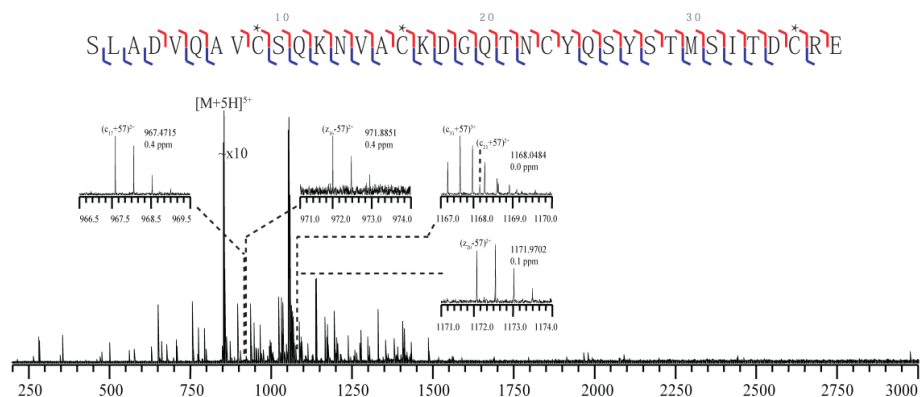


Figure 5.6 The ECD spectrum and the c, z cleavage map of the $[M+5H]^{5+}$ ion of the aged RNaseA peptide ($^{50}\text{SLADVQAVC}^*\text{SQKNVAC}^*\text{KDGQTD}^*\text{YQSYSTMSITDC}^*\text{RE}^{87}$) produced from the Glu-C digestion at pH 4.0 at 25 °C. Insets show the diagnostic ions of isoAsp67 and isoAsp71.

In summary, among the techniques that improved fragmentation efficiency, AI-ECD promoted the production of the isoAsp diagnostic ions without producing signal interferences and ion source contamination. Therefore, AI-ECD was employed as the main MS/MS tool for isoAsp detection for the subsequent studies.

5.3.4 pH Dependence of the IsoAsp Formation Rate during the Glu-C Digestion

In Figure 5.7, using AI-ECD, the isoAsp67 formation rate was monitored during an 18-h Glu-C digestion at different pH values, at 25 °C. The adjacent c₉ ion was included in the figure so that the reader would be able to compare the relative abundance of the isoAsp67 diagnostic ion. Although 4-h Glu-C digestion at pH 7.8 did not introduce an observable shift in the isotope distribution¹⁵², the presence of the low abundance isoAsp67 diagnostic ion suggested that a trace amount of this peptide had already undergone deamidation and subsequently formed isoAsp (Figure 5.7, left column). This result indicated that, in deamidation analyses, the detection of the isoAsp diagnostic ion is more sensitive than the measurement of the isotope pattern shift. The relative intensity of the signal from the isoAsp67 diagnostic ion increased with the time of the Glu-C digestion (Figure 5.7, left column). For Glu-C digestion at pH 4.0, no isoAsp diagnostic ion was detected even for 18-h digestion (Figure 5.7, right column). Because higher temperatures lead to a higher rate of isoAsp formation, the same sets of experiments were performed at 37 °C, and again no isoAsp diagnostic ion was detected at pH 4.0 after 18-h digestion (Figure 5.8). In conclusion, an 18-h overnight Glu-C digestion at pH 4.0 is free of artifactual isoAsp formation.

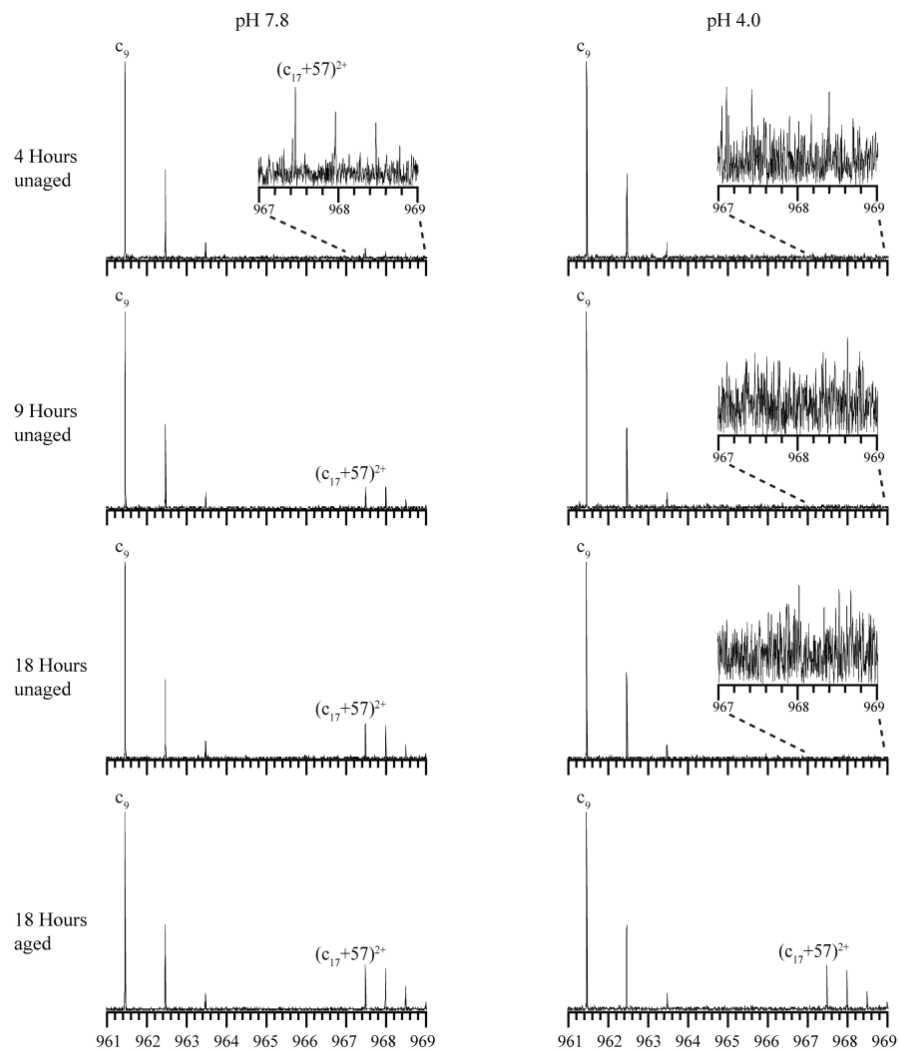


Figure 5.7 Formation of isoAsp 67 during the Glu-C digestion of unaged RNaseA as monitored by its diagnostic ions using AI-ECD. The RNaseA peptides (50-87) were extracted at different times during the Glu-C digestions in buffer solutions at pH 7.8 (left column) and pH 4.0 (right column) at 25 °C. IsoAsp diagnostic ions of the aged RNaseA peptides are also shown at the bottom as controls.

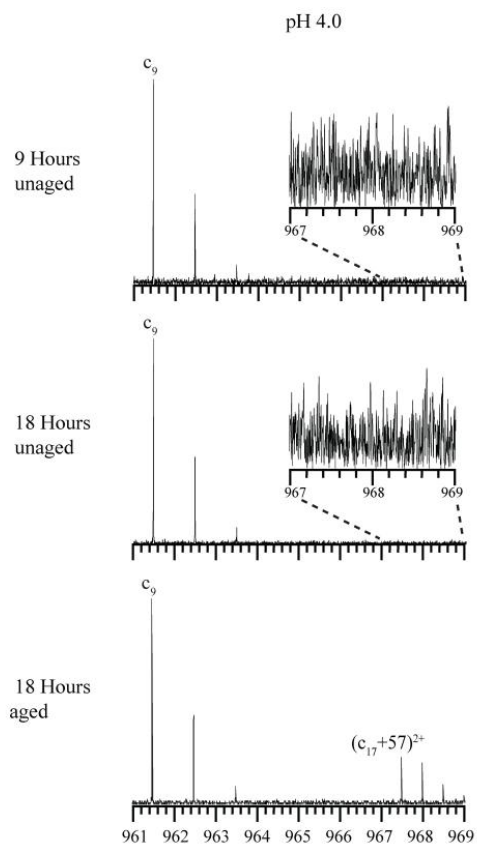


Figure 5.8 Formation of isoAsp67 during the Glu-C digestion of unaged RNaseA as monitored by its diagnostic ions using AI-ECD. Target RNaseA peptides (50 SLADVQAVC*SQKNVAC*KD/(iso)DGQTNC*YQSYSTMSITDC*RE⁸⁷) were extracted after 9-h and 18-h Glu-C digestions in the pH 4.0 buffer solution at 37 °C. Insets indicate the absence of the isoAsp diagnostic ion. IsoAsp diagnostic ions of the aged RNaseA peptides are also shown at the bottom as the positive control.

5.3.5 Identification of IsoAsp42 in Aged β -2-microglobulin

Detection of the isoAsp through the “top-down” strategy is usually challenging because many more fragmentation channels become available and these compete with diagnostic ion formation. In addition, extensive non-covalent interactions in large proteins can also prevent fragment ion separation and detection. In order to reduce the competing fragmentation and non-covalent interactions, gas phase “digestion” through NSD and infrared ion activation are usually needed for “top-down” MS. However, the fragmentation efficiency of the isoAsp42 diagnostic ion remained low even when both NSD and infrared ion activation were applied.¹⁵⁵

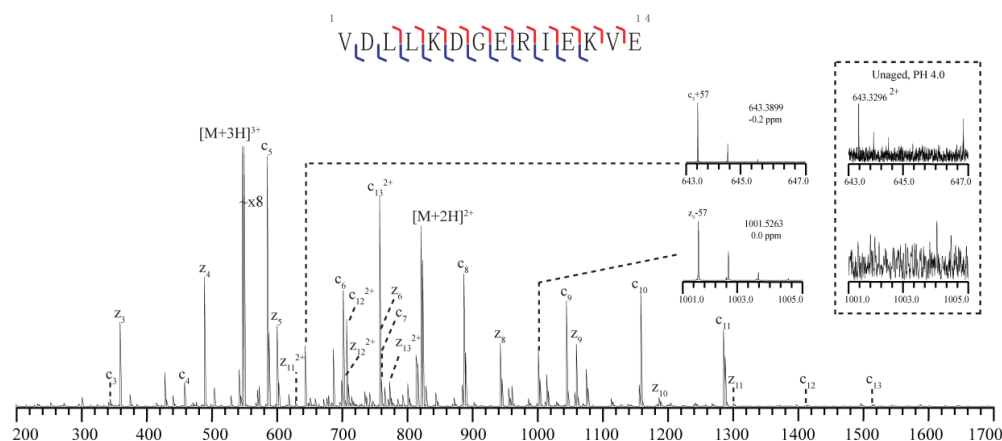


Figure 5.9 ECD spectra of the triply charged aged β 2M peptide from Glu-C overnight digestion at pH 4.0 at 25 °C. Insets show the diagnostic ions of the isoAsp42. Insets in the dotted box illustrate the absence of the isoAsp42 diagnostic ions during the analysis of unaged β 2M peptide obtained at the same conditions.

The Glu-C “middle-down” strategy may be the best means for identification of the β 2M isoAsp42 as we demonstrated that, for RNaseA, this approach was capable of breaking down proteins without introducing artifactual isoAsp. Based on this rationalization, Glu-C overnight digestion of the aged β 2M was carried out at pH 4.0, at 25 °C. Peptides containing Asp/isoAsp 42 were separated and collected by means of off-line RP-HPLC. The peptide with the sequence $^{37}\text{VDLLKD}/(\text{iso})\text{DGERIEKVE}^{50}$ was selected for the ECD experiments because it has 3 lysyl and arginyl residues which could be readily triply charged and therefore seemed likely to exhibit better ECD fragmentation efficiency than the $^{37}\text{VDLLKD}/(\text{iso})\text{DGERIE}^{47}$ (data not shown). As presented in Figure 5.9, for the aged β 2M, ECD of this precursor ion produced both c_5+57 and z_9-57 diagnostic ions, indicating the presence of isoAsp 42. As a control, the same experimental procedures were carried out for the unaged β 2M and no diagnostic ion was detected (dotted inset, Figure 5.9). These results clearly demonstrated that the Glu-C “middle-down” method we developed here is free of artifactual isoAsp and suggests that it should be applicable to the isoAsp characterizations of many more proteins.

5.4 Conclusions

Using RNaseA as the model protein, artifactual deamidation and isoAsp formation during Glu-C digestion were investigated. Our results demonstrated that Glu-C digestion at pH 4.0 completely avoids the occurrence of both artifactual deamidation and subsequent isoAsp formation and therefore could be employed as the primary proteolysis tool for isoAsp analysis. To address the problem that ECD fragmentation efficiency can sometimes exhibit inadequate efficiency for the full sequence determination of the long polypeptides produced by the Glu-C digestion, a middle-down MS/MS technique were also developed; this strategy includes hot-ECD, AI-ECD and charge state pumping. AI-ECD outperformed other techniques, as it offered high fragmentation efficiency without signal interferences or ion source contamination. Furthermore, using the Glu-C “middle-down” approach, we successfully detected the generation of isoAsp42 of β 2M, which was difficult to accomplish using the “top-down” approach. This result portends strong potential for wide application of this method to the analysis of many more proteins. In conclusion, as a straightforward yet powerful complement to the “top-down” approach, the Glu-C “middle-down” strategy reported here should be considered a valuable tool for isoAsp characterization.

Chapter 6 In-Source Decay for Isoaspartate Characterization

6.1 Introduction

Isoaspartic acid (isoAsp) is an isomer of aspartic acid (Asp) that can be formed spontaneously under physiological conditions *via* isomerization of Asp or deamidation of asparagine (Asn) residues.¹⁶⁶ IsoAsp is a β -linked amino acid, i.e., it has an extra methylene group within the peptide backbone. The backbone elongation may significantly alter the protein conformation, leading to changes in protein activity, misfolding and degradation.¹⁶⁷⁻¹⁶⁹ *In vivo*, isoAsp accumulates in long-lived proteins, and this modification is often associated with aging,¹⁶⁷ eye lens abnormalities,¹⁷⁰ and amyloid diseases such as Alzheimer disease.^{168, 171} *In vitro*, isoAsp formation is a major concern in the biopharmaceutical industry, as it can lead to protein aggregation and decrease in activity.

Many analytical tools have been developed for isoAsp characterization in peptides and proteins.¹⁷¹⁻¹⁸¹ Among them, the best results are achieved using high performance liquid chromatography (HPLC)^{177, 182-185} and tandem mass spectrometry (MS/MS) methods.^{65-66, 118-119, 121-122, 186-189} Recently, electron-activated dissociation (ExD) methods, including electron capture dissociation (ECD) and electron transfer dissociation (ETD), have been successfully applied to isoAsp analysis,^{67, 178, 190} which utilize the formation of the

diagnostic fragment ions $c+57$ and z^*-57 resulting from the C_α - C_β bond cleavage within the isoAsp residue for site-specific isoAsp detection.

In-source decay (ISD) fragmentation during the MALDI process is a pseudo tandem MS technique, which allows peptides and proteins to fragment in a single MS stage.¹⁹¹ It is a valuable tool in protein analysis as the protein post-translational modifications (PTMs) are usually preserved during the ISD process. ISD has been applied to analyze peptides and proteins with phosphorylation and O-glycosylation, to differentiate the isomeric amino acid residues leucine and isoleucine, and to obtain information on disulfide-linkages.¹⁹²⁻¹⁹⁴ Alternatively, disulfide bonds can be reduced prior to ISD allowing the analysis of cysteine-containing peptides.¹⁹⁵ Further, it has been shown that only limited hydrogen scrambling is observed during the ISD fragmentation process.¹⁹⁶ This is beneficial for the hydrogen/deuterium exchange studies of proteins that aim to obtain information on their dynamic and structural properties. In addition, ISD has been implemented in MS imaging of tissue samples to simultaneously identify and localize proteins.¹⁹⁷

In ISD, fragmentation occurs as a result of the metastable decay of precursor ions during delayed extraction within the ion source,¹⁹⁸ whereby polypeptide N - C_α bonds are cleaved to generate c and z product ions. These product ions are similar to those generated in ExD; however, the mechanisms of their formation appear to be different. It is proposed that, in ISD, intermolecular hydrogen transfer occurs between the peptide and the

In this study, using MALDI-Fourier transform ion cyclotron resonance (FTICR), we investigated the capability of ISD for the identification of isoAsp. We identified the isoAsp diagnostic ions when a hydrogen-donating matrix was used.

6.2 Experimental

The experimental procedures for reductive alkylation, protein aging, proteolysis and RP-HPLC separation are described in Chapter 5.

6.2.1 Peptides and Reagents

β -2-microglobulin from human urine (β 2M), endoproteinase Glu-C (Glu-C) and MALDI matrices, including 1,5-diaminonaphthalene(1,5-DAN), and 2-picolinic acid (2-PA) were purchased from Sigma-Aldrich (St. Louis, MO). Formic acid (FA) was purchased from Thermo Scientific (Rockford, IL). HPLC grade acetonitrile (ACN) and methanol (MeOH) were obtained from Fisher Scientific (Fairlawn, NJ, USA).

6.2.2 Sample Deposition onto the MALDI-MS Plate

Peptides were dissolved in 50:50 ACN:H₂O with 0.1 % FA at a concentration of 20 pmol/ μ l. The 1,5-DAN and 2-PA matrix was freshly prepared by dissolution in 50:50 ACN:H₂O with 0.1% FA at the concentration of 20 mg/ml. 1,5-DAN and 2-PA solutions were then mixed at the ratio of 3:1 (v:v) as recommended by published reports. Samples were deposited onto a stainless steel MALDI target in a “sandwich” manner: 0.5 μ l of matrix solution followed by 1 μ l of analyte solution and then again 0.5 μ l matrix solution on top, with the droplet being allowed to dry each time before the following layer was spotted.

6.2.3 Mass Spectrometry

The in-source decay experiments were performed on an ESI/MALDI dual source solariXTM hybrid Qh-FTICR instrument (Bruker Daltonics, Billerica, MA) equipped with a 12-T actively shielded magnet. The FTICR parameters were: 30-45 % laser power, 1000 Hz laser frequency, 300 laser shots per scan, 1-50 scans accumulated for each spectrum depending on the purpose of the experiment. Data were analyzed using the DataAnalysis 4.1 software (Bruker Daltonics, Billerica, MA).

6.3 Results and Discussion

6.3.1 C $_{\alpha}$ -C $_{\beta}$ Bond Cleavage within Isoaspartate

Because ISD using a hydrogen-donating matrix results in a fragmentation pattern similar to that obtained by ECD, it seemed possible that ISD follows the same fragmentation pathway as ECD and would thus be expected to generate ECD-like diagnostic ions for isoAsp. To test the applicability of ISD for identification of isoAsp residues, the β 2M protein was aged to induce deamidation and subsequent formation of isoAsp¹⁵⁵ (Chapter 4), and was then digested by Glu-C at pH 4.0 (Chapter 5). Because ISD is a pseudo MS/MS technique without precursor ion selection before dissociation, it was necessary to separate the peptide mixture resulting from the deamidation and Asp isomerization by RP-HPLC, prior to ISD analysis. The HPLC fraction that contained a peptide that included Asn17 (the β 2M peptide 1-36), whose molecular weight determination indicated that it had been completely deamidated after 5-day aging, was subjected to ISD analysis using 1,5-DAN/2-PA matrix on a MALDI-Qq-FTICR mass spectrometer. Figure 6.1 shows that ISD of the singly charged precursor ion produced a continuous series of c-ions from c₅ to c₃₃, as well as some z-ions (excluding cleavages N-terminal to a proline residue). The isoAsp-diagnostic ion, c₁₆+57, was detected in the aged β 2M peptide 1-36 (Figure 6.1, left inset), but not in the unaged control (Figure 6.1, right inset), demonstrating the applicability of ISD for isoAsp analysis.

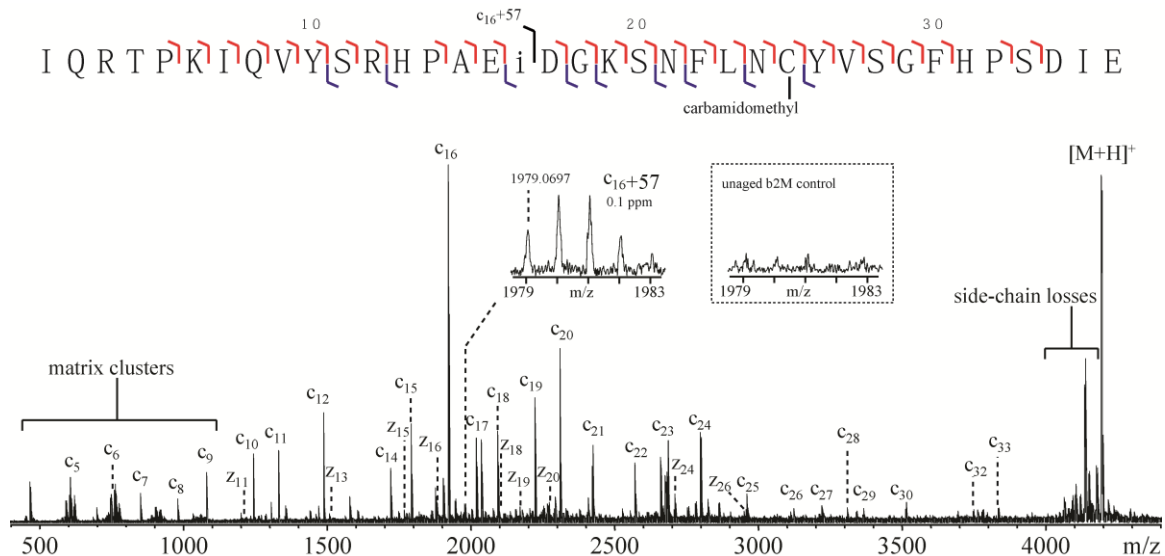


Figure 6.1 The ISD spectrum of the aged and Glu-C digested β 2M peptide (1-36) using 1,5-DAN/2-PA as the matrix, acquired on a solariX 12-T FTICR mass spectrometer. Inset shows the diagnostic fragment for the isoAsp17 residue.

The oxidized and unoxidized species of the aged β 2M peptide 78-99 resulting from the Glu-C digestion at pH 4.0 were also separated by RP-HPLC. The fraction containing the unoxidized form of the β 2M peptide 78-99 was selected for the ISD experiment. Figure 6.2 shows that ISD produced extensive c/z-type fragments for this peptide and the superior resolving power offered by FTICR mass spectrometer is capable of separating the low-mass ISD fragment ion, c_4 , from the matrix cluster (Figure 6.2, left inset). The isoAsp-diagnostic ion, z_{17-57} , was also identified, indicating the formation of isoAsp 83 in the aged β 2M (Figure 6.2, right inset).

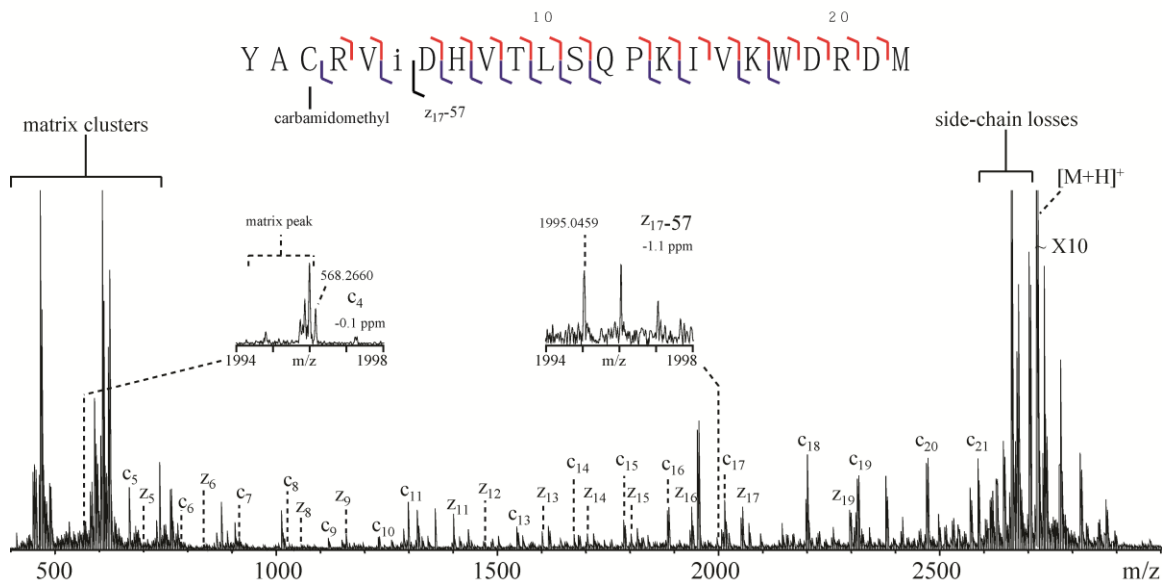


Figure 6.2 The ISD spectrum of the aged and Glu-C digested β 2M peptide (78-99) using 1,5-DAN/2-PA as the matrix, acquired on a solariX 12-T FTICR mass spectrometer.

Protein PTM characterization using ISD can also be achieved at the intact protein level.²⁰²⁻²⁰³ However, the isoAsp diagnostic ions produced by top-down MS/MS are usually below the detection limit due to strong intermolecular interactions and competition from multiple favorable fragmentation channels as discussed in Chapter 4. To increase the sensitivity of ISD in isoAsp identification, continuous accumulation of selected ions (CASI) was employed after ISD. Figure 6.3 illustrates the ISD-CASI spectrum of the reduced and alkylated aged β 2M. The quadrupole Q1 was tuned to allow ions within the m/z range from 1800 to 2000 to pass through, thus preventing overflow of the external collision cell by other, more abundant ions. The ISD product ions within this m/z range were accumulated in the collision cell for \sim 10 ms and then transferred to the ICR mass analyzer. As shown in Figure 6.3, the diagnostic ion of isoAsp 17 can be

readily detected in a single scan, suggesting that the top-down ISD-CASI has great potential in the isoAsp identification.

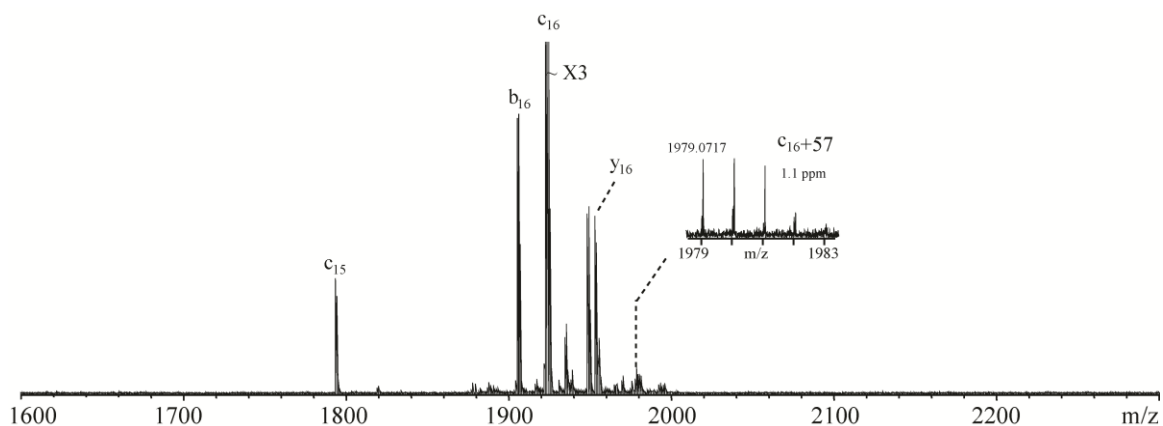
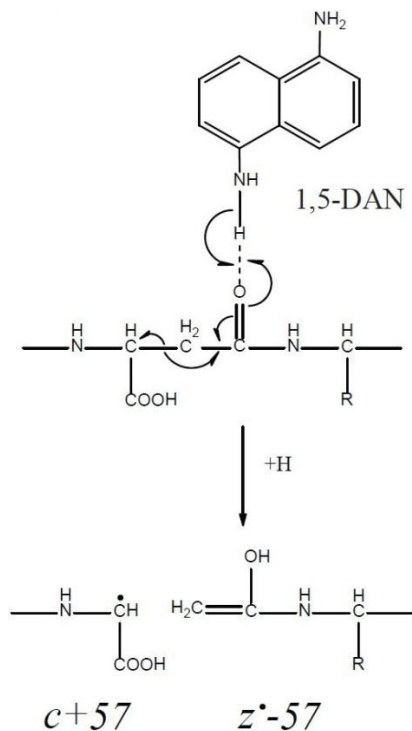


Figure 6.3 The single scan ISD-CASI spectrum of the aged β 2M using 1,5-DAN/2-PA as the matrix, acquired on a solariX 12-T FTICR mass spectrometer.

6.3.2 Mechanism of Diagnostic Ion Formation During ISD

Scheme 6.2 illustrates the proposed mechanism for the formation of the isoAsp diagnostic ion during ISD, using a hydrogen-donating matrix (*e.g.* 1,5-DAN). The process is driven by the stability of the radical in the c+57 product ion, due to the presence of the side-chain carboxylic group.



Scheme 6.2 Formation of the $c+57/z^*-57$ isoAsp diagnostic fragments via hydrogen transfer using 1,5-DAN as the matrix.

6.3.3 Comparison of ISD Performance between FTICR MS and TOF MS

Most of the reported MALDI-ISD experiments have been performed on TOF instruments. Matrix cluster ions are commonly observed in MALDI-TOF mass spectra, and often dominate the low-mass region, preventing reliable identification of low-mass ions, particularly when they are present in low abundance. The use of an FTICR instrument can provide several advantages over a TOF instrument for ISD experiments. First, FTICR mass analysis is performed on a much longer time-scale, allowing some matrix clusters to undergo metastable decomposition before detection. As a result, there

is, in general, less matrix interference. Second, even in the presence of matrix cluster peaks, the superior mass resolving power and mass accuracy afforded by an FTICR mass analyzer can often be utilized for confident identification of peaks of interest (Figure 6.2, left inset). Third, ISD typically requires the use of high laser power, producing a wider spread of ion kinetic energies. This presents a particularly severe problem for axial-TOF instruments, as it leads to poor mass resolving power and decreased mass accuracy. The MALDI-o-TOF instrument shows significantly improved ISD performance over the axial-TOF, as the ions are cooled and focused by buffer gas, and injected orthogonally into the flight tube, minimizing the deleterious effect of the axial kinetic energy spread.²⁰⁴ Similarly, because an FTICR mass analyzer determines the m/z value based on the ion cyclotron frequency, which is independent of its axial velocity, the broader kinetic energy spread will not compromise its performance. Further, FTICR platform can provide the basis for implementation of an IR laser. Gentle irradiation of the ions before detection will destroy matrix clusters and, thus, reduce their interference with ions of interest.

6.4 Conclusions

In this study, we investigated the potential of ISD for the identification of isoAsp. Our results demonstrated that, using a hydrogen-donating matrix, ISD cleaved the C_{α} - C_{β} bond and produced the c -57 and z +57 diagnostic ions, thus enabling isoAsp identification. CASI after ISD may be used to facilitate isoAsp identification at the intact protein level. In general, MALDI-FTICR MS is better suited for isoAsp characterization, as it suffers less interference from matrix clusters and is not affected by the ion kinetic energy spread.

Chapter 7 Conclusions and Future Perspective

7.1 Conclusions

MS/MS has become one of the primary tools for the biomolecule characterization as it is fast, accurate and sensitive. The ion activation methods for MS/MS fall into two categories: vibrational and electronic. Although MS/MS based on vibrational ion activation has been widely implemented in most modern mass spectrometers, they usually provide insufficient structural information for biomolecules. As an alternative, ExD offers extensive complementary structural information and has been successfully applied in the proteomics research. In this thesis, we explored the potentials of ExD in the glycan *de novo* sequencing and isoAsp identification.

The first part of this study focuses on determination of ExD fragmentation mechanisms and application of ExD to glycan *de novo* sequencing. Structural analysis of glycan is challenging as it has multiple levels of structural complexity, including composition, topology, and linkage configuration. Recent development of advanced MS and MS/MS techniques has added new dimensions to the structural analysis of glycans. The composition of a glycan can be easily deduced by measuring the accurate mass of a glycan. Other structural information, including topology, linkage configuration can be obtained through MS/MS, but traditional MS/MS often provides only partial definition of the structures. In order to achieve complete structural elucidation of glycans, it is necessary to understand the mechanisms of glycan fragmentation processes and to

develop robust MS/MS methods to meet the challenges in the modern glycobiochemistry research.

When evaluating the performance of a MS/MS method, two factors need to be considered: the efficiency of the method and the analytical information it provides. The ideal MS/MS method is expected to be highly efficient as well as rich in structural information. By varying the electron energy and metal charge carriers, ExD on model glycans was systematically studied. Depending on the electron energy, ExD can be divided into the following processes: ECD, hot-ECD, EED, and EI_oD. As a charge induced fragmentation technique, ECD, though high in efficiency, produces mostly glycosidic cleavages. Using electrons with higher kinetic energy, a new fragmentation pathway, designated as EED, was found to be the most informative. However, the efficiency of EED needs to be improved in order to practically use this technique in the glycan structural analysis.

The key experimental parameters for an EED experiment include electron density and electron energy distribution. As electrons at the low energy tail will generate ECD-type of fragments and will compete with the EED process, the efficiency of EED can be improved by blocking the low energy electrons and maintaining high electron density at meanwhile. By controlling the above experimental parameters, we further improved the EED efficiency, allowing EED to be performed at the liquid chromatography time scale. The application of EED was further extended to the differentiation of the

oligosaccharides isomers including SLe^A, SLe^X, LNT and LNnT. Results showed EED efficiently produced extensive fragmentation and provided most of the linkage information for various types of glycans, thus allowing confident differentiation of the glycan isomers.

Theoretical modeling was employed to gain insights into the charge remote fragmentation behavior inherent in the EED process. EED is initiated by electron detachment from an oxygen atom, forming a distonic ion. The subsequent electron re-capture produces a di-radical which can undergo extensive fragmentation. As a charge remote process, EED is capable of producing many more structurally informative fragments than ECD, regardless of the type of metal charge carriers.

The second part of this study focuses on the identification of Asn deamidation and Asp isomerization. The characterizations of Asn deamidation and isoAsp through the trypsin based “bottom-up” approaches have the risk of introducing false positive results. Although differentiation of the isomeric Asn deamidation products (Asp and isoAsp) at the peptide level by ECD has been well established, isoAsp identification at the intact protein level remains a challenging task. Here, we designed a comprehensive top-down method using the protein β_2 M as the model system. Of the three deamidation sites identified in the aged β_2 M, isoAsp formation was detected at only one site by the top-down ECD analysis. The absence of diagnostic ions likely resulted from an increased number of competing fragmentation channels and a decreased likelihood of product ion

separation in ECD of proteins. To overcome this difficulty, an MS3 approach was applied where a protein ion was first fragmented by CAD and a resulting product ion was isolated and further analyzed by ECD. IsoAsp formation at all three deamidation sites was successfully identified by this CAD-ECD approach.

With the consideration that the top-down strategy will eventually fail for high molecular weight proteins, a middle-down ExD method was next developed, for the analysis of peptides generated by proteolysis with Staphylococcal serine protease Protease V8 (Glu-C), carried out at slightly acidic conditions. Using Glu-C digested ribonuclease A as the model system, tandem mass spectrometry techniques for isoAsp identification were developed and compared, including ECD, hot-ECD, AIECD and charge state pumping. Our results demonstrated that, at pH 4.0 in ammonium acetate buffer, the Glu-C overnight digestion was free of artifacts. We extended this study to the characterization of isoAsp42 on aged β_2 M, whose analysis was challenging through the top-down approach. The Glu-C middle-down method we developed here readily identified the isoAsp42 without false positive interferences, thus suggesting the promise of this analytical strategy for isoAsp characterization in proteomics studies.

Because the isoAsp characterization through ECD requires expensive FT-ICR instruments and is only applicable to multiply charged precursor ions and does not compatible with MALDI source that generates 1+ precursor ions, we further investigated the potential of MALDI-ISD for the isoAsp characterization. ISD on isoAsp-containing

peptides using hydrogen-donating matrix, 1,5-DAN/2-PA mixture, generates diagnostic fragment ion series $c+57$ and $z'-57$ specific to the isoAsp residue. These results indicate that ISD can be broadly applied for isoAsp characterization regardless of charge state.

In conclusion, the author believes that the work presented in this thesis suggested that EED has the potential to be the experimental basis for the high-throughput glycan *de novo* sequencing. This work also added new dimensions for the confident characterizations of Asn deamidation and isoAsp formation, enabling the practical use of ExD technique in isoAsp characterization.

7.2 Future Perspective

The ultimate goal for the glycan structural analysis is to produce informative MS/MS spectra in a high-throughput manner. The work presented in this thesis demonstrated that EED is informative, sensitive and efficient MS/MS technique for such purpose. However, in order to achieve this goal, it is necessary to setup an online LC-EED MS/MS platform that is compatible with highly heterogeneous glycan samples. Additional studies are needed to synchronize the LC separation with EED. For example, as EED has better performance on glycans adducted with metal charge carriers, it is desirable to use a post-column make-up flow to mix the metal salt solution with the LC eluents. The practical application of EED to the high-throughput analysis of unknown glycan structures also requires the development of a glycan *de novo* sequencing software. With the consideration that glycan has multiple levels of structural complexity, the direct *de novo* linkage analysis will be a daunting task. In order to reduce the complexity, it is necessary to perform the structural analysis as the following stepwise manner: composition analysis, topology analysis, and linkage analysis. The development of such software will need extensive collaboration between scientists in both mass spectrometry and computer science.

For the characterization of Asn deamidation and isoAsp formation, the Glu-C middle-down ECD strategy has been shown to facilitate the isoAsp characterization by reducing the size of the analyte without introducing artifacts. It would be interesting to extend this middle-down method to high molecule weight proteins such as monoclonal antibodies.

Further, although the preliminary data demonstrated the capability of ISD in isoAsp analysis, the efficiency of ISD is still low compared to ECD. A systematic study on the experimental conditions of ISD is necessary in order to obtain an optimized ISD efficiency.

Bibliography

1. Barber, M., R. S. Bordoli, R. D. Sedgwick, A. N. Tyler, *Journal of the Chemical Society-Chemical Communications* **1981**, pp 325-327.
2. Karas, M., D. Bachmann, F. Hillenkamp, *Analytical Chemistry* **1985**, 57, pp 2935-2939.
3. Fenn, J. B., M. Mann, C. K. Meng, S. F. Wong, C. M. Whitehouse, *Science* **1989**, 246, pp 64-71.
4. Karas, M., R. Kruger, *Chemical Reviews* **2003**, 103, pp 427-439.
5. Kebarle, P., U. H. Verkerk, *Mass Spectrom Review* **2009**, 28, pp 898-917.
6. Wilm, M. S., M. Mann, *International Journal of Mass Spectrometry* **1994**, 136, pp 167-180.
7. Wilm, M., M. Mann, *Analytical Chemistry* **1996**, 68, pp 1-8.
8. Dawson, P. H., *Quadrupole mass spectrometry and its applications*. Elsevier Scientific Pub. Co., New York, **1976**; p 349 p.
9. Comisar.Mb, A. G. Marshall, *Chemical Physics Letters* **1974**, 25, pp 282-283.
10. Comisar.Mb, A. G. Marshall, *Chemical Physics Letters* **1974**, 26, pp 489-490.
11. Anders, L. R., Beaucham.Jl, R. C. Dunbar, Baldesch.Jd, *Journal of Chemical Physics* **1966**, 45, pp 1062-&.
12. Baldesch.Jd, *Science* **1968**, 159, pp 263-&.
13. Mciver, R. T., *Review of Scientific Instruments* **1970**, 41, pp 555-&.

14. Marshall, A. G., C. L. Hendrickson, G. S. Jackson, *Mass Spectrom Review* **1998**, *17*, pp 1-35.
15. Amster, I. J., *Journal of Mass Spectrometry* **1996**, *31*, pp 1325-1337.
16. Comisarow, M. B., *International Journal of Mass Spectrometry and Ion Processes* **1981**, *37*, pp 251-257.
17. Sleno, L., D. A. Volmer, *Journal of Mass Spectrometry* **2004**, *39*, pp 1091-1112.
18. An, H. J., C. B. Lebrilla, *Mass Spectrom Review* **2011**, *30*, pp 560-78.
19. Zaia, J., *Mass Spectrom Review* **2004**, *23*, pp 161-227.
20. Johnson, R. S., S. A. Martin, K. Biemann, J. T. Stults, J. T. Watson, *Analytical Chemistry* **1987**, *59*, pp 2621-2625.
21. Zubarev, R. A., N. L. Kelleher, F. W. McLafferty, *Journal of the American Chemical Society* **1998**, *120*, pp 3265-3266.
22. Zubarev, R. A., *Mass Spectrom Review* **2003**, *22*, pp 57-77.
23. Yoo, H. J., N. Wang, S. Zhuang, H. Song, K. Hakansson, *Journal of American Chemical Society* **2011**, *133*, pp 16790-3.
24. Syka, J. E. P., J. J. Coon, M. J. Schroeder, J. Shabanowitz, D. F. Hunt, *Proceedings of the National Academy of Sciences of the United States of America* **2004**, *101*, pp 9528-9533.
25. Kjeldsen, F., K. F. Haselmann, B. A. Budnik, F. Jensen, R. A. Zubarev, *Chemical Physics Letters* **2002**, *356*, pp 201-206.
26. Nielsen, M. L., B. A. Budnik, K. F. Haselmann, J. V. Olsen, R. A. Zubarev, *Chemical Physics Letters* **2000**, *330*, pp 558-562.

27. Haselmann, K. F., B. A. Budnik, F. Kjeldsen, M. L. Nielsen, J. V. Olsen, R. A. Zubarev, *European Journal of Mass Spectrometry (Chichester, Eng)* **2002**, 8, pp 117-121.
28. Nielsen, M. L., B. A. Budnik, K. F. Haselmann, R. A. Zubarev, *International Journal of Mass Spectrometry* **2003**, 226, pp 181-187.
29. Fung, Y. M. E., C. M. Adams, R. A. Zubarev, *Journal of the American Chemical Society* **2009**, 131, pp 9977-9985.
30. Mann, M., O. N. Jensen, *Nature Biotechnology* **2003**, 21, pp 255-261.
31. Varki, A., *Essentials of glycobiology*. 2nd ed.; Cold Spring Harbor Laboratory Press: Cold Spring Harbor, N.Y., **2009**; p xxix, 784 p.
32. Lehninger, A. L., D. L. Nelson, M. M. Cox, *Lehninger principles of biochemistry*. 4th ed.; W.H. Freeman: New York, **2005**.
33. Molinari, M., *Nature Chemical Biology* **2007**, 3, pp 313-320.
34. Slawson, C., G. W. Hart, *Nature Reviews Cancer* **2011**, 11, pp 678-684.
35. Pang, P. C., P. C. N. Chiu, C. L. Lee, L. Y. Chang, M. Panico, H. R. Morris, S. M. Haslam, K. H. Khoo, G. F. Clark, W. S. B. Yeung, A. Dell, *Science* **2011**, 333, pp 1761-1764.
36. Domon, B., C. E. Costello, *Glycoconjugate Journal* **1988**, 5, pp 397-409.
37. Reinhold, V. N., B. B. Reinhold, C. E. Costello, *Analytical Chemistry* **1995**, 67, pp 1772-1784.
38. Ashline, D. J., A. J. Lapadula, Y. H. Liu, M. Lin, M. Grace, B. Pramanik, V. N. Reinhold, *Analytical Chemistry* **2007**, 79, pp 3830-3842.
39. Budnik, B. A., K. F. Haselmann, Y. N. Elkin, V. I. Gorbach, R. A. Zubarev, *Analytical Chemistry* **2003**, 75, pp 5994-6001.

40. McFarland, M. A., A. G. Marshall, C. L. Hendrickson, C. L. Nilsson, P. Fredman, J. E. Mansson, *Journal of the American Society for Mass Spectrometry* **2005**, *16*, pp 752-762.
41. Wolff, J. J., I. J. Amster, L. L. Chi, R. J. Linhardt, *Journal of the American Society for Mass Spectrometry* **2007**, *18*, pp 234-244.
42. Wolff, J. J., T. N. Laremore, A. M. Busch, R. J. Linhardt, I. J. Amster, *Journal of the American Society for Mass Spectrometry* **2008**, *19*, pp 294-304.
43. Zaia, J., C. E. Costello, *Analytical Chemistry* **2003**, *75*, pp 2445-55.
44. Wolff, J. J., L. L. Chi, R. J. Linhardt, I. J. Amster, *Analytical Chemistry* **2007**, *79*, pp 2015-2022.
45. Adamson, J. T., K. Hakansson, *Analytical Chemistry* **2007**, *79*, pp 2901-10.
46. Zhao, C., B. Xie, S. Y. Chan, C. E. Costello, P. B. O'Connor, *Journal of the American Society for Mass Spectrometry* **2008**, *19*, pp 138-150.
47. Adamson, J. T., K. Hakansson, *Analytical Chemistry* **2007**, *79*, pp 2901-2910.
48. Wolff, J. J., F. E. Leach, T. N. Laremore, D. A. Kaplan, M. L. Easterling, R. J. Linhardt, I. J. Amster, *Analytical Chemistry* **2010**, *82*, pp 3460-3466.
49. Leach, F. E., J. J. Wolff, Z. P. Xiao, M. Ly, T. N. Laremore, S. Arungundram, K. Al-Mafraji, A. Venot, G. J. Boons, R. J. Linhardt, I. J. Amster, *European Journal of Mass Spectrometry (Chichester, Eng)* **2011**, *17*, pp 167-176.
50. Han, L., C. E. Costello, *Journal of the American Society for Mass Spectrometry* **2011**, *22*, pp 997-1013.
51. Robinson, A. B., N. E. Robinson, *Proceedings of the National Academy of Sciences of the United States of America* **2001**, *98*, pp 944-949.

52. Roher, A. E., J. D. Lowenson, S. Clarke, C. Wolkow, R. Wang, R. J. Cotter, I. M. Reardon, H. A. Zurcherneeely, R. L. Heinrikson, M. J. Ball, B. D. Greenberg, *Journal of Biological Chemistry* **1993**, 268, pp 3072-3083.
53. Shirasawa, T., T. Shimizu, Y. Matsuoka, *Biological & Pharmaceutical Bulletin* **2005**, 28, pp 1590-1596.
54. Zhao, R., G. A. Follows, P. A. Beer, L. M. Scott, B. J. P. Huntly, A. R. Green, D. R. Alexander, *New England Journal of Medicine* **2008**, 359, pp 2778-2789.
55. Cimmino, A., R. Capasso, F. Muller, I. Sambri, L. Masella, M. Raimo, M. L. De Bonis, S. D'Angelo, V. Zappia, P. Galletti, D. Ingrosso, *Plos One* **2008**, 3.
56. Mamula, M. J., H. A. Doyle, R. J. Gee, *Autoimmunity* **2007**, 40, pp 131-137.
57. Mamula, M. J., R. J. Gee, J. I. Elliott, A. Sette, S. Southwood, P. J. Jones, P. R. Blier, *Journal of Biological Chemistry* **1999**, 274, pp 22321-22327.
58. Robinson, A. B., N. E. Robinson, *Proceedings of the National Academy of Sciences of the United States of America* **2001**, 98, pp 4367-4372.
59. Patel, K., R. T. Borchardt, *Pharmaceutical Research* **1990**, 7, pp 787-793.
60. Capasso, S., S. Salvadori, *Journal of Peptide Research* **1999**, 54, pp 377-382.
61. Trout, B. L., B. Peters, *Biochemistry* **2006**, 45, pp 5384-5392.
62. Patel, K., R. T. Borchardt, *Pharmaceutical Research* **1990**, 7, pp 703-711.
63. Wakankar, A. A., R. T. Borchardt, *Journal of Pharmaceutical Sciences* **2006**, 95, pp 2321-2336.
64. Yang, H. Q., R. A. Zubarev, *Electrophoresis* **2010**, 31, pp 1764-1772.

65. Cournoyer, J. J., J. L. Pittman, V. B. Ivleva, E. Fallows, L. Waskell, C. E. Costello, P. B. O'Connor, *Protein Science* **2005**, *14*, pp 452-463.
66. Chan, W. Y. K., T. W. D. Chan, P. B. O'Connor, *Journal of the American Society for Mass Spectrometry* **2010**, *21*, pp 1012-1015.
67. Yang, H. Q., E. Y. M. Fung, A. R. Zubarev, R. A. Zubarev, *Journal of Proteome Research* **2009**, *8*, pp 4615-4621.
68. Li, X., J. J. Cournoyer, C. Lin, P. B. O'Connor, *Journal of the American Society for Mass Spectrometry* **2008**, *19*, pp 855-64.
69. Varki, A., *Glycobiology* **1993**, *3*, pp 97-130.
70. Dwek, R. A., *Chemical Reviews* **1996**, *96*, pp 683-720.
71. Ashline, D., S. Singh, A. Hanneman, V. Reinhold, *Analytical Chemistry* **2005**, *77*, pp 6250-6262.
72. Zaia, J., *Mass Spectrometry Review* **2004**, *23*, pp 161-227.
73. Harvey, D. J., *Journal of the American Society for Mass Spectrometry* **2001**, *12*, pp 926-937.
74. Lemoine, J., B. Fournet, D. Despeyroux, K. R. Jennings, R. Rosenberg, E. Dehoffmann, *Journal of the American Society for Mass Spectrometry* **1993**, *4*, pp 197-203.
75. Brull, L. P., W. Heerma, J. ThomasOates, J. Haverkamp, V. Kovacik, P. Kovac, *Journal of the American Society for Mass Spectrometry* **1997**, *8*, pp 43-49.
76. Kovacik, V., J. Hirsch, P. Kovac, W. Heerma, J. Thomasoates, J. Haverkamp, *Journal of Mass Spectrometry* **1995**, *30*, pp 949-958.

77. Ernst, B., D. R. Muller, W. J. Richter, *International Journal of Mass Spectrometry and Ion Processes* **1997**, *160*, pp 283-290.
78. Harvey, D. J., *Proteomics* **2005**, *5*, pp 1774-1786.
79. Zhang, J. H., L. T. LaMotte, E. D. Dodds, C. B. Lebrilla, *Analytical Chemistry* **2005**, *77*, pp 4429-4438.
80. Adamson, J. T., K. Hakansson, *Journal of Proteome Research* **2006**, *5*, pp 493-501.
81. Xie, Y. M., C. B. Lebrilla, *Analytical Chemistry* **2003**, *75*, pp 1590-1598.
82. Harvey, D. J., R. H. Bateman, M. R. Green, *Journal of Mass Spectrometry* **1997**, *32*, pp 167-187.
83. Thompson, M. S., W. D. Cui, J. P. Reilly, *Angewandte Chemie, International Edition* **2004**, *43*, pp 4791-4794.
84. Zaia, J., J. L. Seymour, C. E. Costello, *Glycobiology* **2005**, *15*, pp 1209-1209.
85. Cancilla, M. T., S. G. Penn, J. A. Carroll, C. B. Lebrilla, *Journal of the American Chemical Society* **1996**, *118*, pp 6736-6745.
86. Cancilla, M. T., A. W. Wang, L. R. Voss, C. B. Lebrilla, *Analytical Chemistry* **1999**, *71*, pp 3206-3218.
87. Fura, A., J. A. Leary, *Analytical Chemistry* **1993**, *65*, pp 2805-2811.
88. Harvey, D. J., *Journal of Mass Spectrometry* **2000**, *35*, pp 1178-1190.
89. Ngoka, L. C., J. F. Gal, C. B. Lebrilla, *Analytical Chemistry* **1994**, *66*, pp 692-698.
90. Hofmeister, G. E., Z. Zhou, J. A. Leary, *Journal of the American Chemical Society* **1991**, *113*, pp 5964-5970.

91. Costello, C. E., J. M. Contado-Miller, J. F. Cipollo, *Journal of the American Society for Mass Spectrometry* **2007**, *18*, pp 1799-1812.
92. Viseux, N., E. deHoffmann, B. Domon, *Analytical Chemistry* **1997**, *69*, pp 3193-3198.
93. Ciucanu, I., F. Kerek, *Carbohydrate Research* **1984**, *131*, pp 209-217.
94. Ciucanu, I., C. E. Costello, *Journal of the American Chemical Society* **2003**, *125*, pp 16213-16219.
95. Jebanathirajah, J. A., J. L. Pittman, B. A. Thomson, B. A. Budnik, P. Kaur, M. Rape, M. Kirschner, C. E. Costello, P. B. O'Connor, *Journal of the American Society for Mass Spectrometry* **2005**, *16*, pp 1985-1999.
96. O'Connor, P. B., J. L. Pittman, B. A. Thomson, B. A. Budnik, J. C. Cournoyer, J. Jebanathirajah, C. Lin, S. Moyer, C. Zhao, *Rapid Communications in Mass Spectrometry* **2006**, *20*, pp 259-266.
97. Kaur, P., P. B. O'Connor, *Journal of the American Society for Mass Spectrometry* **2006**, *17*, pp 459-468.
98. Koster, C., A. Holle, in *ASMS annual conference*. Dallas, TX, **1999**.
99. Ceroni, A., A. Dell, S. M. Haslam, *Source Code for Biology and Medicine* **2007**, *2*, p 3.
100. Ceroni, A., K. Maass, H. Geyer, R. Geyer, A. Dell, S. M. Haslam, *Journal of Proteome Research* **2008**, *7*, pp 1650-1659.
101. Cody, R. B., B. S. Freiser, *Analytical Chemistry* **1979**, *51*, pp 547-551.
102. Zheng, Y. J., R. L. Ornstein, J. A. Leary, *Journal of Molecular Structure-Theochem* **1997**, *389*, pp 233-240.

103. Yu, X., Y. Huang, C. Lin, C. E. Costello, *Analytical Chemistry* **2012**, *84*, pp 7487-7494.
104. Fung, Y. M. E., C. M. Adams, R. A. Zubarev, *Journal of the American Chemical Society* **2009**, *131*, pp 9977-9985.
105. Hitchcock, A. M., M. J. Bowman, G. O. Staples, J. Zaia, *Electrophoresis* **2008**, *29*, pp 4538-4548.
106. Nilsson, M. R., M. Driscoll, D. P. Raleigh, *Protein Science* **2002**, *11*, pp 342-349.
107. Robinson, N. E., A. B. Robinson, *Proceedings of the National Academy of Sciences of the United States of America* **2001**, *98*, pp 944-949.
108. Robinson, A. B., *Mechanisms of Ageing and Development* **1979**, *9*, pp 225-236.
109. Hains, P. G., R. J. W. Truscott, *Investigative Ophthalmology & Visual Science* **2010**, *51*, pp 3107-3114.
110. Takata, T., J. T. Oxford, B. Demeler, K. J. Lampi, *Protein Science* **2008**, *17*, pp 1565-1575.
111. Liu, D. T. Y., *Trends in Biotechnology* **1992**, *10*, pp 364-369.
112. Lindner, H., W. Helliger, *Experimental Gerontology* **2001**, *36*, pp 1551-1563.
113. Wright, H. T., *Critical Reviews in Biochemistry and Molecular Biology* **1991**, *26*, pp 1-52.
114. Aswad, D. W., M. V. Paranandi, B. T. Schurter, *Journal of Pharmaceutical and Biomedical Analysis* **2000**, *21*, pp 1129-1136.
115. Zhang, W., M. J. Czupryn, *Journal of Pharmaceutical and Biomedical Analysis* **2003**, *30*, pp 1479-1490.

116. Chazin, W. J., J. Kordel, E. Thulin, T. Hofmann, T. Drakenberg, S. Forsen, *Biochemistry* **1989**, 28, pp 8646-8653.
117. Carlson, A. D., R. M. Riggin, *Analytical Biochemistry* **2000**, 278, pp 150-155.
118. Castet, S., C. Enjalbal, P. Fulcrand, J. F. Guichou, J. Martinez, J. L. Aubagnac, *Rapid Communications in Mass Spectrometry* **1996**, 10, pp 1934-1938.
119. Gonzalez, L. J., T. Shimizu, Y. Satomi, L. Betancourt, V. Besada, G. Padron, R. Orlando, T. Shirasawa, Y. Shimonishi, T. Takao, *Rapid Communications in Mass Spectrometry* **2000**, 14, pp 2092-2102.
120. Cournoyer, J. J., C. Lin, P. B. O'Connor, *Analytical Chemistry* **2006**, 78, pp 1264-1271.
121. Cournoyer, J. J., C. Lin, M. J. Bowman, P. B. O'Connor, *Journal of the American Society for Mass Spectrometry* **2007**, 18, pp 48-56.
122. O'Connor, P. B., J. J. Cournoyer, S. J. Pitteri, P. A. Chrisman, S. A. McLuckey, *Journal of the American Society for Mass Spectrometry* **2006**, 17, pp 15-19.
123. Yang, H., E. Y. M. Fung, A. R. Zubarev, R. A. Zubarev, *Journal of Proteome Research* **2009**, 8, pp 4615-4621.
124. Yang, H., R. A. Zubarev, *Electrophoresis* **2010**, 31, pp 1764-1772.
125. Li, X. J., J. J. Cournoyer, C. Lin, P. B. O'Connor, *Journal of the American Society for Mass Spectrometry* **2008**, 19, pp 855-864.
126. Chait, B. T., *Science* **2006**, 314, pp 65-66.
127. Yates, J. R., C. I. Ruse, A. Nakorchevsky, *Annual Review of Biomedical Engineering* **2009**, 11, pp 49-79.

128. Sargaeva, N. P., C. Lin, P. B. O'Connor, *Analytical Chemistry* **2009**, *81*, pp 9778-9786.
129. Radford, S. E., W. S. Gosal, G. W. Platt, *Biochimica Et Biophysica Acta-Proteins and Proteomics* **2005**, *1753*, pp 51-63.
130. Heegaard, N. H. H., *Amyloid-Journal of Protein Folding Disorders* **2009**, *16*, pp 151-173.
131. Druke, T. B., Z. A. Massy, *Seminars in Dialysis* **2009**, *22*, pp 378-380.
132. Eakin, C. M., A. D. Miranker, *Biochimica Et Biophysica Acta-Proteins and Proteomics* **2005**, *1753*, pp 92-99.
133. Srikanth, R., V. L. Mendoza, J. D. Bridgewater, G. S. Zhang, R. W. Vachet, *Biochemistry* **2009**, *48*, pp 9871-9881.
134. Antwi, K., M. Mahar, R. Srikanth, M. R. Olbris, J. F. Tyson, R. W. Vachet, *Protein Science* **2008**, *17*, pp 748-759.
135. Naiki, H., S. Yamamoto, K. Hasegawa, I. Yamaguchi, Y. Goto, F. Gejyo, *Amyloid-Journal of Protein Folding Disorders* **2005**, *12*, pp 15-25.
136. Kad, N. M., N. H. Thomson, D. P. Smith, D. A. Smith, S. E. Radford, *Journal of Molecular Biology* **2001**, *313*, pp 559-571.
137. Iwata, K., T. Matsuura, K. Sakurai, A. Nakagawa, Y. Goto, *Journal of Biochemistry* **2007**, *142*, pp 413-419.
138. Borysik, A. J. H., S. E. Radford, A. E. Ashcroft, *Journal of Biological Chemistry* **2004**, *279*, pp 27069-27077.
139. Tsybin, Y. O., C. L. Hendrickson, S. C. Beu, A. G. Marshall, *International Journal of Mass Spectrometry* **2006**, *255-256*, pp 144-149.

140. Bleiholder, C., S. Osburn, T. D. Williams, S. Suhai, M. Van Stipdonk, A. G. Harrison, B. Paizs, *Journal of the American Chemical Society* **2008**, *130*, pp 17774-17789.
141. Harrison, A. G., A. B. Young, C. Bleiholder, S. Suhai, B. Paizs, *Journal of the American Chemical Society* **2006**, *128*, pp 10364-10365.
142. Li, X. J., Y. Q. Huang, P. B. O'Connor, C. Lin, *Journal of the American Society for Mass Spectrometry* **2011**, *22*, pp 245-254.
143. Goloborodko, A., M. Gorshkov, D. Good, R. Zubarev, *Journal of the American Society for Mass Spectrometry* **2011**, *22*, pp 1121-1124.
144. Saminathan, I. S., X. S. Wang, Y. Guo, O. Krakovska, S. Voisin, A. C. Hopkinson, K. W. M. Siu, *Journal of the American Society for Mass Spectrometry* **2010**, *21*, pp 2085-2094.
145. Yu, L., Y. Tan, Y. Tsai, D. R. Goodlett, N. C. Polfer, *Journal of Proteome Research* **2011**, *10*, pp 2409-2416.
146. Thøerge, R., G. Infusini, W. Tong, M. E. McComb, C. E. Costello, *International Journal of Mass Spectrometry* **2011**, *300*, pp 130-142.
147. Manning, M. C., D. K. Chou, B. M. Murphy, R. W. Payne, D. S. Katayama, *Pharmaceutical Research* **2010**, *27*, pp 544-575.
148. Schmid, D. G., F. von der Mulbe, B. Fleckenstein, T. Weinschenk, G. Jung, *Analytical Chemistry* **2001**, *73*, pp 6008-6013.
149. O'Connor, P. B., J. J. Cournoyer, J. L. Pittman, V. B. Ivleva, E. Fallows, L. Waskell, C. E. Costello, *Protein Science* **2005**, *14*, pp 452-463.
150. O'Connor, P. B., W. Y. K. Chan, T. W. D. Chan, *Journal of the American Society for Mass Spectrometry* **2010**, *21*, pp 1012-1015.

151. O'Connor, P. B., J. J. Cournoyer, C. Lin, *Analytical Chemistry* **2006**, 78, pp 1264-1271.
152. O'Cormora, P. B., X. J. Li, J. J. Cournoyer, C. Lin, *Journal of the American Society for Mass Spectrometry* **2008**, 19, pp 855-864.
153. O'Connor, P. B., N. P. Sargaeva, C. Lin, *Analytical Chemistry* **2011**, 83, pp 6675-6682.
154. McLafferty, F. W., V. Zabrouskov, X. M. Han, E. Welker, H. L. Zhai, C. Lin, K. J. van Wijk, H. A. Scheraga, *Biochemistry* **2006**, 45, pp 987-992.
155. Li, X. J., X. Yu, C. E. Costello, C. Lin, P. B. O'Connor, *Analytical Chemistry* **2012**, 84, pp 6150-6157.
156. Horn, D. M., Y. Ge, F. W. McLafferty, *Analytical Chemistry* **2000**, 72, pp 4778-4784.
157. Fenselau, C., J. Cannon, K. Lohnes, C. Wynne, Y. Wang, N. Edwards, *Journal of Proteome Research* **2010**, 9, pp 3886-3890.
158. Garcia, B. A., *Journal of the American Society for Mass Spectrometry* **2010**, 21, pp 193-202.
159. Ni, W. Q., S. J. Dai, B. L. Karger, Z. H. S. Zhou, *Analytical Chemistry* **2010**, 82, pp 7485-7491.
160. Drapeau, G. R., J. Houmard, Y. Boily, *Journal of Biological Chemistry* **1972**, 247, pp 6720-&.
161. Houmard, J., G. R. Drapeau, *Proceedings of the National Academy of Sciences of the United States of America* **1972**, 69, pp 3506-3509.
162. Didonato, A., M. A. Ciardiello, M. Denigris, R. Piccoli, L. Mazzarella, G. Dalessio, *Journal of Biological Chemistry* **1993**, 268, pp 4745-4751.

163. Bhatt, N. P., K. Patel, R. T. Borchardt, *Pharmaceutical Research* **1990**, 7, pp 593-599.
164. Pitteri, S. J., P. A. Chrisman, J. M. Hogan, S. A. McLuckey, *Analytical Chemistry* **2005**, 77, pp 1831-1839.
165. Lomeli, S. H., I. X. Peng, S. Yin, R. R. O. Loo, J. A. Loo, *Journal of the American Society for Mass Spectrometry* **2010**, 21, pp 127-131.
166. Robinson, N. E., A. B. Robinson, *Molecular clocks: Deamidation of asparaginyl and glutaminyl residues in peptides and proteins*. Althouse Press: Cave Junction, OR, **2004**; p 443.
167. Ritz-Timme, S., M. J. Collins, *Ageing Research Reviews* **2002**, 1, pp 43-59.
168. Roher, A. E., J. D. Lowenson, S. Clarke, C. Wolkow, R. Wang, R. J. Cotter, I. M. Reardon, H. A. Zurcherneeely, R. L. Heinrikson, M. J. Ball, B. D. Greenberg, *Journal of Biological Chemistry* **1993**, 268, pp 3072-3083.
169. Shimizu, T., A. Watanabe, M. Ogawara, H. Mori, T. Shirasawa, *Archives of Biochemistry and Biophysics* **2000**, 381, pp 225-234.
170. Fujii, N., Y. Ishibashi, K. Satoh, M. Fujino, K. Harada, *Biochim Biophys Acta* **1994**, 1204, pp 157-63.
171. Shimizu, T., Y. Matsuoka, T. Shirasawa, *Biological & Pharmaceutical Bulletin* **2005**, 28, pp 1590-1596.
172. Di Donato, A., M. A. Ciardiello, M. de Nigris, R. Piccoli, L. Mazzarella, G. D'Alessio, *Journal of Biological Chemistry* **1993**, 268, pp 4745-51.
173. Aswad, D. W., M. V. Paranandi, B. T. Schurter, in *3rd Symposium on the Analysis of Well Characterized Biotechnology Pharmaceuticals*. Pergamon-Elsevier Science Ltd: Washington, D.C., **1999**, pp 1129-1136.

174. Alfaro, J. F., L. A. Gillies, H. G. Sun, S. J. Dai, T. Z. Zang, J. J. Klaene, B. J. Kim, J. D. Lowenson, S. G. Clarke, B. L. Karger, Z. S. Zhou, *Analytical Chemistry* **2008**, *80*, pp 3882-3889.
175. Shin, Y., H. S. Cho, H. Fukumoto, T. Shimizu, T. Shirasawa, S. M. Greenberg, G. W. Rebeck, *Acta Neuropathologica* **2003**, *105*, pp 252-258.
176. Kameoka, D., T. Ueda, T. Imoto, *Journal of Biochemistry* **2003**, *134*, pp 129-135.
177. Rehder, D. S., D. Chelius, A. McAuley, T. M. Dillon, G. Xiao, J. Crouse-Zeineddini, L. Vardanyan, N. Perico, V. Mukku, D. N. Brems, M. Matsumura, P. V. Bondarenko, *Biochemistry* **2008**, *47*, pp 2518-30.
178. Ni, W., S. Dai, B. L. Karger, Z. S. Zhou, *Analytical Chemistry* **2010**, *82*, pp 7485-91.
179. Terashima, I., A. Koga, H. Nagai, *Analytical Biochemistry* **2007**, *368*, pp 49-60.
180. Xiao, G., P. V. Bondarenko, J. Jacob, G. C. Chu, D. Chelius, *Analytical Chemistry* **2007**, *79*, pp 2714-2721.
181. Li, X. J., J. J. Cournoyer, C. Lin, P. B. O'Cormora, *Journal of the American Society for Mass Spectrometry* **2008**, *19*, pp 855-864.
182. Zhang, W., M. J. Czupryn, *J Pharm Biomed Anal* **2003**, *30*, pp 1479-90.
183. Krokhin, O. V., M. Antonovici, W. Ens, J. A. Wilkins, K. G. Standing, *Analytical Chemistry* **2006**, *78*, pp 6645-50.
184. De Boni, S., C. Oberthur, M. Hamburger, G. K. E. Scriba, *Journal of Chromatography A* **2004**, *1022*, pp 95-102.
185. Winter, D., R. Pipkorn, W. D. Lehmann, *Journal of Separation Science* **2009**, *32*, pp 1111-1119.

186. Lehmann, W. D., A. Schlosser, G. Erben, R. Pipkorn, D. Bossemeyer, V. Kinzel, *Protein Science* **2000**, *9*, pp 2260-2268.
187. Yamazaki, Y., N. Fujii, Y. Sadakane, *Analytical Chemistry* **2010**, *82*, pp 6384-94.
188. Sargaeva, N. P., C. Lin, P. B. O'Connor, *Analytical Chemistry* **2009**, *81*, pp 9778-9786.
189. Liu, M., J. Cheetham, N. Cauchon, J. Ostovic, W. Ni, D. Ren, Z. S. Zhou, *Analytical Chemistry* **2011**, *84*, pp 1056-1062.
190. Mukherjee, R., L. Adhikary, A. Khedkar, H. Iyer, *Rapid Commun Mass Spectrom* **2010**, *24*, pp 879-84.
191. Brown, R. S., J. J. Lennon, *Analytical Chemistry* **1995**, *67*, pp 3990-3999.
192. Jagannadham, M. V., R. Nagaraj, *Analytical Chemistry Insights* **2008**, *3*, pp 21-9.
193. Soltwisch, J., K. Dreisewerd, *Analytical Chemistry* **2010**, *82*, pp 5628-35.
194. Demeure, K., V. Gabelica, E. A. De Pauw, *Journal of the American Society for Mass Spectrometry* **2010**, *21*, pp 1906-1917.
195. Scheffler, K., T. Arrey, K. Strupat, in *The 59th ASMS Conference on Mass Spectrometry and Allied Topics*. Denver, CO, USA, **2011**.
196. Bache, N., K. D. Rand, P. Roepstorff, T. J. Jorgensen, *Analytical Chemistry* **2008**, *80*, pp 6431-5.
197. Zimmerman, T. A., D. Debois, G. Mazzucchelli, V. Bertrand, M. C. De Pauw-Gillet, E. De Pauw, *Analytical Chemistry* **2011**, *83*, pp 6090-6097.
198. Lennon, J. J., K. A. Walsh, *Protein Science* **1997**, *6*, pp 2446-2453.

199. Takayama, M., *Journal of the American Society for Mass Spectrometry* **2001**, *12*, pp 1044-1049.
200. Kocher, T., A. Engstrom, R. A. Zubarev, *Analytical Chemistry* **2005**, *77*, pp 172-7.
201. Demeure, K., L. Quinton, V. Gabelica, E. De Pauw, *Analytical Chemistry* **2007**, *79*, pp 8678-85.
202. Lennon, J. J., K. A. Walsh, *Protein Science* **1997**, *6*, pp 2446-53.
203. Hanisch, F. G., *Analytical Chemistry* **2011**, *83*, pp 4829-37.
204. Soltwisch, J., J. Souady, S. Berkenkamp, K. Dreisewerd, *Analytical Chemistry* **2009**, *81*, pp 2921-34.

Curriculum Vitae

Xiang Yu

Education

- Ph.D., Biochemistry, January 2013
Boston University, School of Medicine, Boston, MA
Thesis title: Glycan Sequencing and Isoaspartate Characterization by Electron Activated Dissociation Tandem Mass Spectrometry
Advisor: Catherine E. Costello
- B.S., Biotechnology, June 2007
Sichuan University, Wuyuzhang Honorary College, Chengdu, China, 2007
Thesis title: Molecular Cloning and Expression of the Nkx-2.5 with Cardiac-specific Enhancer

Publications

- **Yu, X.**, Huang, Y., Lin, C. and Costello, C. E., *Energy-Dependent Electron Activated Dissociation of Metal-Adducted Permethylyated Oligosaccharides*. Anal. Chem., 2012 84(17), pp7487-7490
- Li, X., **Yu, X. (Co-first Author)**, Costello C.E., O'Connor, P.B. and Lin, C., *Top-down Study of beta-2-Microglobulin Deamidation*. Anal. Chem., 2012 84(14), pp 6150-6157
- Huang, Y., Shi, X.F., **Yu, X.**, Leymarie N., Staples, G.O., Zaia, J., and et al., *Improved LC-MS/MS of Heparan Sulfate Oligosaccharides via Chip-based Pulsed Make-up Flow*. Anal. Chem., 2011 83(21), pp 8222–8229

Awards and Honors

- Student Travel Award, Society for Glycobiology (2010, 2011)
- Distinguished Undergraduate Award, Sichuan University (2007)
- ‘Spark’ Research Award, Sichuan University (2006)